

Snow Depth Retrieval and Downscaling using Satellite Laser Altimetry, Machine Learning, and Climate Reanalysis

A Case Study in Mainland Norway

Zhihao LIU



Table of Contents

| | |
|--|-----------|
| 1. Introduction | 1 |
| 1.1. The Role of Snow Cover | 1 |
| 1.1.1. Climate indicator | 1 |
| 1.1.2. Energy balance component | 2 |
| 1.1.3. Water reservoir | 3 |
| 1.1.4. Ecological habitats | 3 |
| 1.1.5. Thermal insulator | 5 |
| 1.1.6. Geohazards | 5 |
| 1.2. The Variability of the Snow Cover | 5 |
| 1.2.1. Spatial variability | 5 |
| 1.2.2. Temporal variability | 7 |
| 1.3. The Challenges of the Snow Observation | 7 |
| 1.4. Objectives | 9 |
| 1.5. Thesis structure | 10 |
| 2. Scientific Overview | 11 |
| 2.1. Satellite Altimetry | 11 |
| 2.1.1. Altimetry: radar and laser | 11 |
| 2.1.2. ICESat-2 | 12 |
| 2.2. DEM and Co-registration | 14 |
| 2.2.1. DEM products | 14 |
| 2.2.2. DEM uncertainties | 14 |
| 2.2.3. DEM Co-registration | 17 |
| 2.3. Machine Learning and XGBoost | 18 |
| 2.4. Climate Reanalysis and Downscaling | 20 |
| 2.5. Literature highlights | 21 |
| 2.5.1. Addressing DEM errors by ICESat-2 | 21 |
| 2.5.2. Snow depth from ICESat-2 | 21 |
| 2.5.3. Subgrid variability of snow and statistical downscaling | 23 |

Table of Contents

| | |
|---|-----------|
| 3. Methodologies | 27 |
| 3.1. Research Design | 27 |
| 3.2. Data Preparation | 29 |
| 3.2.1. ICESat-2 ATL08 | 29 |
| 3.2.2. DEM products | 30 |
| 3.2.3. Terrain and vegetation parameters | 31 |
| 3.2.4. ERA5 Land: snow and wind parameters | 33 |
| 3.3. Gradient Descent Co-registration | 34 |
| 3.4. XGBoost Regression Model | 37 |
| 3.4.1. Bias correction | 37 |
| 3.4.2. Statistical downscaling | 39 |
| 3.4.3. Hyperparameters and cross-validation | 41 |
| 3.5. Evaluation of Snow Depth | 42 |
| 3.5.1. ICESat-2 derived snow depth vs lidar derived snow depth | 42 |
| 3.5.2. ICESat-2 derived snow depth vs ERA5 Land snow depth | 43 |
| 3.5.3. Downscaled snow depth vs lidar derived snow depth | 44 |
| 4. Study Case - mainland Norway | 45 |
| 4.1. The Physical Geographical Setting | 45 |
| 4.2. The Data Setting | 46 |
| 4.3. DEM Coregistration | 46 |
| 4.4. Bias Binning Analysis: DEM Comparison | 51 |
| 4.5. Features Importance and Regression Performance | 53 |
| 4.6. ICESat-2 Derived Snow Depth and Validation | 56 |
| 4.7. Downscaled Snow Depth and Validation | 60 |
| 5. Discussion | 65 |
| 5.1. GDC vs NuthKaab Co-registration: Which and Why | 65 |
| 5.1.1. Noise suppression | 65 |
| 5.2. The Uncertainties: ICESat-2, DEM and Snow Depth | 67 |
| 5.2.1. ICESat-2 ATL08: skewness and curvature | 67 |
| 5.2.2. Uncertainties in DEMs: vegetation, resolution | 70 |
| 5.2.3. Uncertainties of snow depth: assumptions and solutions | 73 |
| 5.3. ICESat-2 Derived Snow Depth VS ERA5 Land: Cutting-out and Overestimation | 77 |
| 5.4. Downscaling and subgrid distribution | 81 |
| A. Appendix | 83 |
| A.1. Additional Figures | 83 |

Table of Contents

| | | |
|-------------------|---|-----------|
| A.2. | Technical Details of ICESat-2 ATL08 | 83 |
| A.2.1. | Processing and QC Steps of ICESat-2 ATL08 Land products | 83 |
| A.2.2. | Processing and QC Steps of ICESat-2 ATL08 Canopy products | 87 |
| A.3. | Recommendation For Winter Canopy Height Correction | 87 |
| A.4. | Code Repository | 88 |
| A.4.1. | Gradient Descent Coregistration | 88 |
| A.4.2. | XSnow | 88 |
| References | | 89 |

List of Figures

| | |
|--|----|
| 1.1. Historical Snow Trend from 1981 to 2018 (Monthly) | 2 |
| 1.2. Snowmelt-Dominated Catchments: Present and Future | 4 |
| 1.3. Snow Redistribution and Wind | 6 |
| 2.1. Timeline of Satellite Altimetry since the 1990s | 11 |
| 2.2. The ICESat-2 and Photon Counting System | 13 |
| 2.3. Uncertainty Framework for DEM Assessment | 15 |
| 2.4. Mean Absolute Errors of Global DEM Products in the Tibetan Plateau | 16 |
| 2.5. How XGBoost Works | 19 |
| 2.6. A Bias Correction Scheme for DEMs Based on Slopes and Vegetation Coverage | 22 |
| 2.7. An Overview of Models for Snow Redistribution | 24 |
| 3.1. Study Design Schematic | 28 |
| 3.2. The Topography Index: Scale-dependent Effects | 33 |
| 3.3. Quantifying the Relationship between Wind and Aspect in Snow Redistribution | 35 |
| 3.4. Coregistration Techniques: NuthKaab vs. Gradient Descent | 36 |
| 3.5. Preventing Overfitting with Cross-validation in XGBoost | 42 |
| 3.6. Snow Survey via Drone Lidar in Hardangervidda, Southern Norway | 43 |
| 4.1. The Climate of Norway | 47 |
| 4.2. The ICESat-2 Segments and Snow Surveys | 48 |
| 4.3. The Misalignment of DEMs | 50 |
| 4.4. Statistic binning Analysis: Coregistration and Bias correction (ICESat-2 - DTM10) | 52 |
| 4.5. The Mean Error and NMAD of Quantiles: Coregistration and Bias correction | 53 |
| 4.6. The Overall Distribution of DEM errors: Coregistration and Bias correction | 54 |
| 4.7. Bias Correction Map for Snow-on Scenarios | 55 |
| 4.8. Features Importance of Bias Correction Regression | 57 |
| 4.9. Snow Depth from ICESat-2 and Four DEMs, 2018-2022. | 58 |
| 4.10. The Vidaliltion of ICESat-2 Derived Snow Depth | 60 |
| 4.11. The Vidaliltion of Snow Depth Downscaling: Map | 61 |
| 4.12. The Vidaliltion of Snow Depth Downscaling: Scatter Plot | 62 |
| 4.13. Features Importance of Snow Depth Downscaling | 63 |

List of Figures

| | | |
|------|--|----|
| 5.1. | Brute-Froce Test on Gradient Descent Coregistration | 66 |
| 5.2. | ICESat-2 Consistency: Year, Day/night, Strong/Weak, Beams and Pairs | 69 |
| 5.3. | Skewness Variations in Convex and Concave Terrains | 71 |
| 5.4. | Comparison of FAB, GLO30, and DTM1 in terms of Plan Curvature and Canopy Height . | 72 |
| 5.5. | Framework for Evaluating Snow Depth from Elevation Differencing: the assumption and the uncertainties. | 74 |
| 5.6. | Distribution of Vegetation Height in snow-free and Snow-on Segments. | 76 |
| 5.7. | Features Related to Snow-on and Snow-free surface | 78 |
| 5.8. | ICESat-2 Derived Snow Depth VS ERA5 Land Snow Depth. | 79 |
| 5.9. | Impact of Cutting-out Negative Values on Snow Depth Statistics. | 80 |
| A.1. | The Monthly Average of Wind Speed and Direction in Winter (2019-2022) | 84 |
| A.2. | Statistic binning Analysis of DEM Errors: Coregistration and Bias correction (ICESat-2 - DTM1) | 85 |
| A.3. | Comparision of DTM1 and DTM10 in terms of Plan Curvature and Canopy Height . . . | 86 |

List of Tables

| | | |
|------|--|----|
| 1.1. | Snow Distribution at Different Scales. | 6 |
| 2.1. | Global DEM products. | 14 |
| 3.1. | Features in the Bias Correction Regressor | 38 |
| 3.2. | Features in the Downscaling Regressor | 40 |
| 4.1. | The Improvement of DEM by Coregistration | 48 |
| 4.2. | The Improvement of DEM by Coregistration (<i>subset_te_flag</i> equals 5) | 49 |
| 4.3. | Cross Validation of Bias Correction Regression | 56 |

1. Introduction

1.1. The Role of Snow Cover

Imagining a world with more or less snow, what would happen? Snow cover is a vital component of Earth's seasonal cycle and is a most spread and variable surface condition. Around 47% of the Northern Hemisphere (NH) land surface is covered by snow in winter (Estilow et al., 2015). Moreover, 1.9 billion people rely on glaciers and seasonal snow packs for their freshwater supply (Barnett et al., 2005; Immerzeel et al., 2020). Changes in snow cover interact with various systems, such as climate, hydrology, geohazards, and ecology (Henderson et al., 2018; Immerzeel et al., 2020), through influencing the surface energy balance, water balance, thermal regimes, vegetation, and trace gas fluxes (Callaghan et al., 2011). Therefore, understanding the role of snow cover and observing its variability are crucial for addressing challenges on regional and global scales.

1.1.1. Climate indicator

Seasonal snow cover is a valuable climate indicator due to its sensitivity to changes in air temperature and humidity, as demonstrated by observations and models (Brown & Mote, 2009; Gulev et al., 2021). For instance, a remarkable linear relationship exhibits that a 1-degree Celsius increase in warming leads to a decrease in NH spring snow cover extent of about 8 % relative to the 1995 - 2014 level in the World Climate Research Programme Coupled Model Intercomparison Project Phase 6 (CMIP6) (L. Mudryk et al., 2020).

The spring snow cover has significantly decreased in mountain regions particularly at lower elevations. On average, the duration of snow cover has declined by 5 days per decade (Hock et al., 2019). In the Alps, there has been a decrease of 5.6% per decade in snow cover duration over the past 50 years (Carrer et al., 2023; Matiu et al., 2021). In the Arctic, the snow cover extent has decreased by an average of $-3.5 \pm 1.9\%$ per decade in May and $-13.4 \pm 5.4\%$ per decade in June between 1967 and 2018 (Meredith et al., 2019), along with snow cover duration decreased by two to four days per decade since 1970s (AMAP, 2017).

Not just snow cover, several satellite-based passive microwave and other products indicate but also a general negative NH snow mass trends in all months between 1981 and 2018 except summer with little

1. Introduction

snow as showed in Figure 1.1. The shift from solid to liquid precipitation are observed during shoulder seasons (L. Mudryk et al., 2020) and in mountain areas (Rhoades et al., 2022; Siirila-Woodburn et al., 2021). The worldwide reduction in glacier mass balance (Hugonnet et al., 2021) also implies a loss of snow on glaciers and ice sheets, again a partial confirmation of the declining of snow mass (Kraaijenbrink et al., 2021; Kumar et al., 2019).

In North America, maximum snow depth has generally decreased in a robust trend since the 1960s (Kunkel et al., 2016). In the Alps, maximum snow depth decreased -8.4% per decade in recent fifty years (Matiu et al., 2021). However, most of studies noted strong regional and temporal variations on snow depth (or snow water equivalent) in Eurasia (Luoju et al., 2021), in the Qinghai-Tibet Plateau (Kraaijenbrink et al., 2021; Xu et al., 2017) due to limited data coverage and lack of high-resolution observations for mountain regions (Kunkel et al., 2016), and in some cases, increasing humidity enables intense snowfall, whereas higher temperatures decrease the likelihood of snowfall (L. Mudryk et al., 2020; Musselman et al., 2021; Quante et al., 2021).

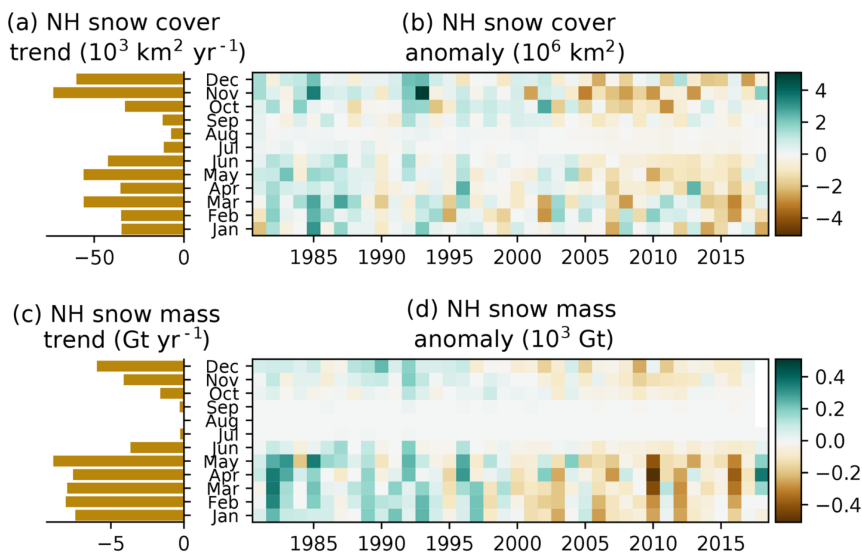


Figure 1.1.: Historical Snow Trend from 1981 to 2018 (Monthly). Trends in snow extent over 1981–2018 are negative in all months and exceed $-50 \times 10^3 \text{ km}^2 \text{ yr}^{-1}$ during November, December, March, and May (a, b). Snow mass trends are approximately -5 Gt yr^{-1} or more for all months from December to May (c, d). Source: L. Mudryk et al. (2020).

1.1.2. Energy balance component

The presence or absence of snow controls patterns of heating and cooling over Earth's surface. When snow is white and highly reflective (albedo 0.8 - 0.9 for fresh snow); a vast amount of sunlight is re-

1.1. The Role of Snow Cover

flected back into space instead of warming the surface. Without snow cover, or snow is covered by black carbon (Réveillet et al., 2022), the ground absorbs more of the sun's energy, accelerating melting and warming further, namely snow and ice albedo feedback (X. Chen et al., 2017; Perovich et al., 2007; Riihelä et al., 2021)

Under higher RCP scenarios, the trends and variability in snow cover are of paramount importance for cold regions. These regions are expected to experience substantially lower spring snow cover than the present day by the end of the twenty-first century. The degree of global warming is inextricably linked to the retreat of seasonal snow cover, and thus, understanding the variability of snow spatially and temporally is critical to identify climate-cryosphere interactions (Henderson et al., 2018).

1.1.3. Water reservoir

Snowpack plays a crucial role as a surface water storage reservoir, influencing the timing of runoff that sustains the water demands of downstream ecosystems and approximately 1.9 billion people (Barnett et al., 2005; Immerzeel et al., 2020; Kraaijenbrink et al., 2021). Furthermore, it serves as an essential indicator for flood prediction and provides early warning of hydrologic drought (Livneh & Badger, 2020).

Alterations in snowpacks can significantly impact water availability, particularly in a warmer world (Figure 1.2). This is due to reduced winter precipitation falling as snow and an earlier onset of melting in spring. Even without any changes in precipitation intensity, these effects lead to a shift in peak river runoff from summer and autumn when demand is highest towards winter and early spring (Barnett et al., 2005).

1.1.4. Ecological habitats

Changes in snow conditions can have significant impacts on the distribution of vegetation, biodiversity, and productivity in various environments (Callaghan & Johansson, 2021) such as alpine (Wipf et al., 2009), Arctic (Sturm et al., 2001), and desert regions (PENG et al., 2010). These changes can affect ecosystem through frost events, soil moisture, and winter soil temperatures, surface energy budgets (Callaghan et al., 2011; Harpold & Molotch, 2015). For instance, research has shown that forest productivity in the California Sierra Nevada region increases with more snow accumulation, particularly at mid-elevation sites where water availability is limited (Siirila-Woodburn et al., 2021). The Arctic regions are experiencing 'greening' in the past decades due to decreases of snow cover duration and extending of growing season (Callaghan et al., 2011), but it reversed to 'browning' trend in the past few years in some areas, demonstrating the complexity of the snow-vegetation interactions (Myers-Smith et al., 2020).

1. Introduction

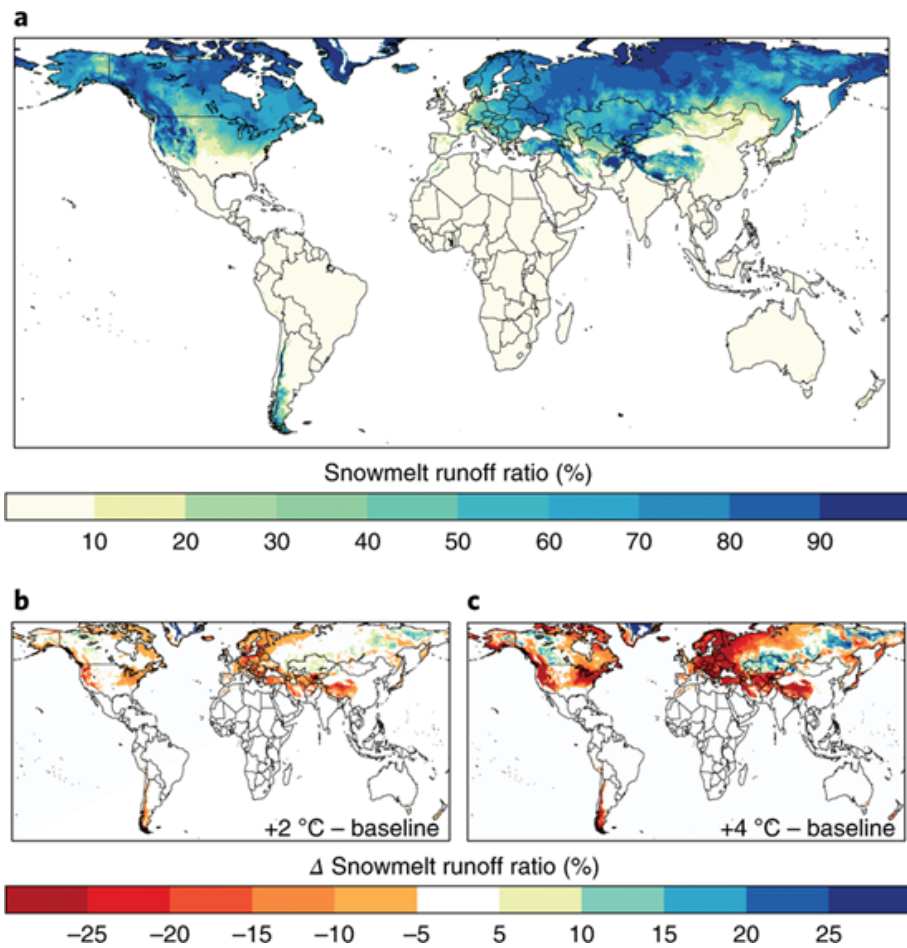


Figure 1.2.: Snowmelt-Dominated Catchments: Present and Future. The average ratio of annual runoff from snowmelt based on historical data (1985-2015). It shows that snowmelt contributes to at least half of the runoff across 26% of the global land area, particularly in western US, Tibetan Plateau (TP), Central Asia, the southern Andes, and Scandinavia (a). In addition, in a warmer climate, the proportion of runoff derived from snowmelt significantly declines with an average warming of 2 °C and 4 °C (b, c, respectively). Source: Qin et al. (2020).

1.2. The Variability of the Snow Cover

1.1.5. Thermal insulator

The structure of porous snow layers makes them good thermal insulators, which has profound implications for the permafrost thermal regime. For instance, the height of palsa formations influences their decay rate, as a higher palsa accumulates more snow on its leeward side due to snow drift, than a lower palsa. The thicker the snow depth, the less cold penetration there would be in winter and the more meltwater in spring and summer, leading to increased local permafrost thawing and block erosion (Olvmo et al., 2020; Seppälä, 1994). After accounting for statistically-derived snow depths, regional permafrost models suggest nearly twice as large a total permafrost area in Norway compared to those without factor of snow (Gisnås et al., 2016). The same insolation mechanism applies to float ice (Sturm & Massom, 2016) and winter wheat as well (Zhu et al., 2022).

1.1.6. Geohazards

Avalanches occur when a massive amount of snow slides down a slope, often triggered by external factors such as weather changes, earthquake or human activities. The impact of an avalanche can be devastating, causing serious damage to infrastructure and loss of life. Yet the a single avalanche event cannot be predicted (Schweizer et al., 2003, 2021). Another snow-related geohazard that can pose a threat to society is snow storm, heavy snow can accumulate on building roofs, eletrical grid, causing structural damage. In addition, transportation can be severely affected by heavy snowfalls that block roads or railways, leading to traffic congestion and delays (Mo et al., 2016).

1.2. The Variability of the Snow Cover

As a consequence of Earth's seasonal cycles, climate patterns, and long-term climate change, snow cover is one of the most variable land surface conditions, both spatially and temporally. Simulating these changes can be challenging due to the high degree of region-to-region and season-to-season variability in trends, as well as the range of metrics used to characterize snow cover, including snow extent, duration, and mass (L. Mudryk et al., 2020).

1.2.1. Spatial variability

The spatial variability of snow accumulation is influenced by various factors such as climate, topography, vegetation, and wind at different scales. While climate is a major contributor to large-scale variations of snow accumulation, smaller scales are affected significantly by the effects of topography, vegetation, and wind (Table 1.1). The relationship between vegetation and snow is complex; for

1. Introduction

instance, forests can reduce horizontal snow redistribution and trap more snow than open areas. Furthermore, vegetation affects snow interception by altering surface albedo and reducing wind speeds (Freudiger et al., 2017; Trujillo et al., 2007).

The topography of a region plays a critical role in shaping the distribution of snow as it influences various factors such as temperature, precipitation, solar radiation and wind speeds and direction. Wind-driven processes influence the redistribution of snow, ranging from orographic precipitation at large scales to preferential deposition of snowfall, and wind-induced transport of snow on smaller scales. Additionally, avalanches are also a significant agent (Mott et al., 2018) (Figure 1.3).

Table 1.1.: Snow Distribution at Different Scales.

| Scales | Distance | Factors |
|------------|-----------------|--|
| Macroscale | 10 km - 1000 km | Dynamic meteorologic effects |
| Mesoscale | 100 m - 10 km | Wind redistribution, terrain and vegetation. |
| Microscale | 10 m - 100 m | Air flow patterns and transportation |

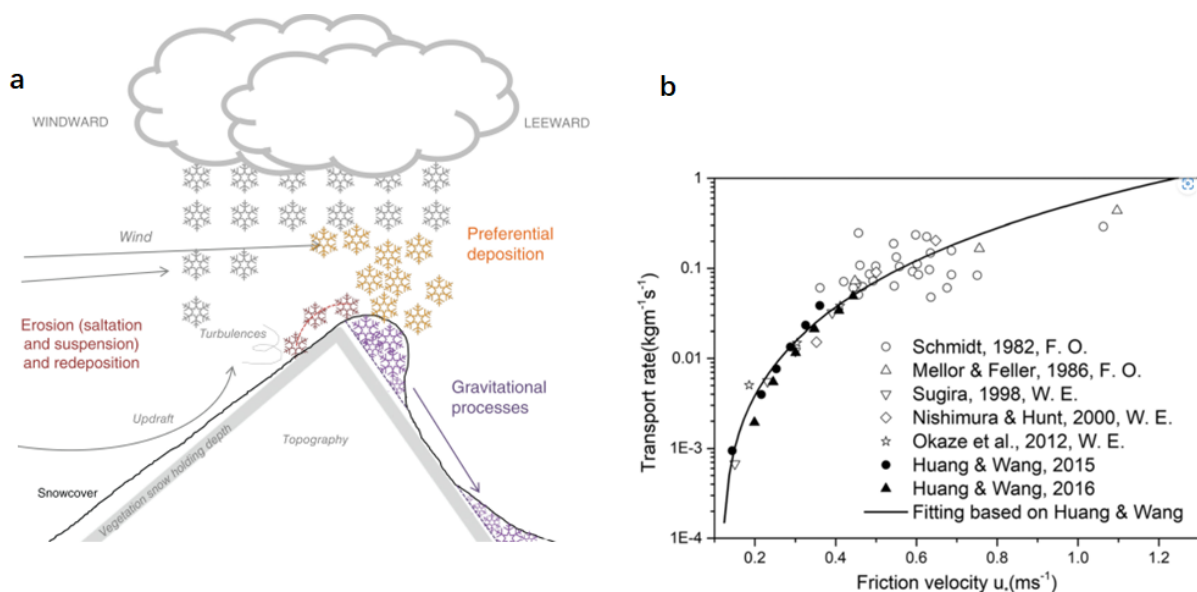


Figure 1.3.: Snow Redistribution and Wind. Wind erosion, deposition and gravity processes (avalanche) drive snow redistribution (a). The aeolian research suggests that as wind speed increases, the transport rate increases exponentially with a power of 3 (b). Adapted from Freudiger et al. (2017); G. Li et al. (2018).

1.2.2. Temporal variability

Snow cover is subject to variation across different temporal scales. On average, in January, snow covers about 47% of the land surface in the Northern Hemisphere, while in August, only 3% is covered by snow (Estilow et al., 2015). Additionally, snow accumulation changes from year to year. Decadal variability refers to fluctuations that occur over periods of ten years or more and are frequently associated with long-term climate variability and climate change (see Section 1.1.1).

Over the time, the development of the snowpack is driven by melting energy, which can be expressed in terms of the snowmelt energy balance (Anderson, 1968). This serves as the fundamental principle for numerical modeling of snowpack:

$$Q_m = Q_{ns} + Q_{nl} + Q_h + Q_e + Q_p + Q_g \quad (1.1)$$

where all Q refer to heat fluxes (W m^{-2}). Q_m is the total heat flux (positive or negative) available for snow melting, Q_{ns} is the short-wave radiation, Q_{nl} is the long-wave radiation, Q_h is the sensible heat flux, Q_e is the latent heat flux caused by water phase changes, Q_p is the heat supplied by precipitation, Q_g is the heat supplied by the ground.

1.3. The Challenges of the Snow Observation

Snowpack is characterized via three variables: snow cover extent (SCE), continuous snow cover duration (SCD), and snow accumulation, which can be expressed as either snow depth (SD) or snow water equivalent (SWE).

There are two types products for mapping snow cover: a binary classification in which each pixel in an image is designated as ‘snow’ or ‘non-snow’ cover area (SCA) or a snow-cover fraction (SCF). The snow cover information is usually derived from optical satellite systems because of their high resolution but with obvious limitations related to persistent clouds, forest cover (Nolin, 2010) and lack of solar illumination at higher latitude regions (Fox-Kemper et al., 2021).

There are two types of products for mapping snow cover: binary classification, which designates each pixel in an image as either “non-snow” or “snow” cover area (SCA), and snow-cover fraction (SCF). Optical satellite systems are typically used to derive snow cover information due to their high resolution, but with obvious limitations such as persistent clouds, forest cover (Nolin, 2010), and lack of solar illumination at higher latitudes (Fox-Kemper et al., 2021).

The MODIS (Moderate Resolution Imaging Spectroradiometer) provides one of the state-of-the-art snow cover products. It has a high spatial resolution (500 m) and daily coverage that can extend the

1. Introduction

time series from 2000 to present (Hall et al., 2006). The MODIS products keep updateing for improvements related to better long-term calibration and enhancements to the cloud mask and atmospheric profile algorithms (Crawford, 2015). High-resolution Landsat imagery has also proven useful for validating operational snow-cover products and for applications that require snow cover information at spatial scales of less than 50 m (Macander et al., 2015).

Snow mass is a challenging parameter to monitor, both globally and regionally, when compared to snow cover extent. A major persistent gap in contemporary is observing reliable SWE over mountain regions (Bormann et al., 2018). There are several reasons for this:

- (1) Measurement stations are generally located in gentle terrain at lower or mid elevation, which makes it difficult to obtain representative measurements for regions with varying topography. Moreover, the precipitation gauges often have errors due to wind effects which can lead to significant and systematic underestimates of up to 50% (Rasmussen et al., 2012), particularly for historical achieves.
- (2) Passive microwave radiometers have been used since 1978 to retrieve snow water equivalent (SWE) using an algorithm that calculates the difference at 19 and 37 GHz (Chang et al., 1987). The coarse resolution of passive microwave data (typically 25 to 50 km) limits its usefulness for finer spatial scales particular in areas of mountainous terrain (Snauffer et al., 2016).
- (3) Lidar does not measure depth directly. Instead, lidar data are acquired over an area prior to snowfall, and repeated later when snow is present to create a map of the snow surface. The height difference between the bare earth and snow surface is inferred to represent snow depth. Airborne lidar is local interest and costly; thus, it is more successful in mapping snow depth at the watershed scale (Deems et al., 2013).
- (4) Due to limitations such as sparse observation networks, satellite retrieval algorithm uncertainties, simplified model parameterizations, spatiotemporal inaccuracies in forcing data (e.g., precipitation), peak seasonal snow mass over the northern hemisphere vary as much as 50% between datasets over the 1981–2010 period with even higher uncertainties for mountain regions (L. R. Mudryk et al., 2015).

Despite the limitations in measuring peak seasonal snow mass, there are several remote sensing techniques and data assimilation models that have shown potential in accurately measuring snow depth at various scales:

- (1) If a snow-free digital elevation model (DEM) is available, satellite altimetry (Treichler & Kääb, 2017) and structure-from-motion techniques can be used to construct snow depth over mountain terrain (Deschamps-Berger et al., 2020).
- (2) Active microwave remote sensing, or radar, can be used to measure SWE with a finer spatial resolution than passive microwave radiometry. However, it is important to acknowledge the

1.4. Objectives

limitations of using low frequency radar (C-band) which cannot detect dry, thin snow and may not penetrate wet and deep snow (Dietz et al., 2012). It has been reported that microwaves can penetrate up to 20 meters in dry conditions, but this depth decreases to only 13.8 centimeters with only 1% liquid water content (Rott & Nagler, 1993). Current solutions include empirical models to retrieve dry snow depth from Sentinel-1 C-band radar at a resolution of 500 m to 1 km (Lievens et al., 2019, 2022). A new approach using a combination of Ku-band and X-band frequencies has been proposed to measure SWE by volume scattering from millimeter-scale snow grains (Tsang et al., 2022; Yueh et al., 2009). Yet, accurate retrievals are still impeded by atmospheric effects and high vegetation fraction (>25%). Moreover, geometric distortions in mountainous terrain, long repeat orbit time, and the inability to precisely model SWE when the snow is vertically inhomogeneous or melting should also be considered when utilizing radar for SWE assessment (Nolin, 2010).

- (3) The state of art snow observation dataset, the GlobSnow v3.0, is a combination of satellite-based passive microwave radiometer data (Nimbus-7 SMMR, DMSP SSM/I and DMSP SSMIS) with ground based synoptic snow depth observations using bayesian data assimilation, incorporating the HUT Snow Emission model (Luoju et al., 2021). However, the mountain areas, which still masked out due to the complex terrain (Bormann et al., 2018).
- (4) Gridded snow datasets are becoming increasingly available, but they still have limitations in redistribution processes and face challenges at hill-slope scales (as discussed further in Section 2.5.3). For regional scales, higher resolution downscaled products offer more realistic patterns of snow water equivalent (SWE) than climate reanalyses (Klehm et al., 2013). At hemispheric scale, the latest CMIP6 model have excessive snow mass and do not accurately simulate snow extent during the accumulation and snowmelt periods (L. Mudryk et al., 2020).

1.4. Objectives

The primary objective of this study is to develop a comprehensive workflow for retrieving and downscaling snow depth using satellite laser altimetry, machine learning, and climate reanalysis. The study will be conducted with a focus on mainland Norway, but the methodology can be applied globally. The specific objectives of this study are as follows:

- (1) To develop a universal co-registration algorithm for efficiently co-registering high-resolution DEMs and/or point measurements.
- (2) To benchmark available DEM products by utilizing ICESat-2 snow-off segments and develop a workflow for identifying and correcting biases in the DEM data using machine learning.

1. Introduction

- (3) To generate a novel ICESat-2 derived snow depth dataset (2018-2022) covering mainland Norway, incorporating the bias-corrected DEM from objective (2) and ICESat-2 ATL08 snow-on segments.
- (4) To develop a statistical downscaling method for snow depth using machine learning techniques and climate reanalysis ERA5 Land, which can provide a spatially complete snow depth map.
- (5) To evaluate the accuracy of the developed workflow by comparing the ICESat-2 derived snow depth dataset with in-situ snow depth measurements.

By achieving these objectives step by step, this study aims to improve our understanding of snow depth distribution and variation, particularly in remote areas. This can have significant implications for water resource management, hydrological modeling, and climate change studies. Additionally, this study will refine our comprehension of the DEM uncertainties and data quality of ICESat-2 ATL08 products. Furthermore, this study will provide a novel contribution by creating a training dataset for machine learning that addresses subgrid snow distribution, which is likely the first of its kind on a national scale.

1.5. Thesis structure

Chapter 1 provides an overview of the role of snow cover, the variability of snow cover, and the challenges associated with snow observation. It also outlines the objectives and structure of the thesis.

Chapter 2 offers a review of the key concepts involved in the laser-derived snow depth workflow. This includes satellite laser altimetry, DEM uncertainties, co-registration, machine learning, climate analysis, downscaling techniques, and highlights from previous studies.

Chapter 3 details the workflow process. This chapter covers data preparation, co-registration of DEM and ICESat-2 to generate differential datasets, accounting for DEM uncertainties using snow-off segments from ICESat-2 data, DEM bias correction using ICEsat-2 as a reference, snow depth retrieval and downscaling using XGBoost algorithm. This chapter also includes data collection methods of field validation.

Chapter 4 presents a case study conducted in mainland Norway with in-situ validation. The results are then discussed in *Chapter 5* with an emphasis on uncertainties and snow depth distribution.

Finally, *Chapter 6* offers future prospects and concluding remarks on this method's potential for improving our understanding of snow cover dynamics.

2. Scientific Overview

2.1. Satellite Altimetry

2.1.1. Altimetry: radar and laser

The satellite radar altimetry is a remote sensing techniques started at the end of the 1960s. The major goal was to measure the shape of the Earth, observing the changes on Earth surface, by the round trip travel time of a short electromagnetic pulse sent from an orbiting spacecraft toward the planetary body (Abdalla et al., 2021). There are three types of sensors, including radar altimetry, InSAR (interferometric synthetic aperture radar) altimetry and laser altimetry.

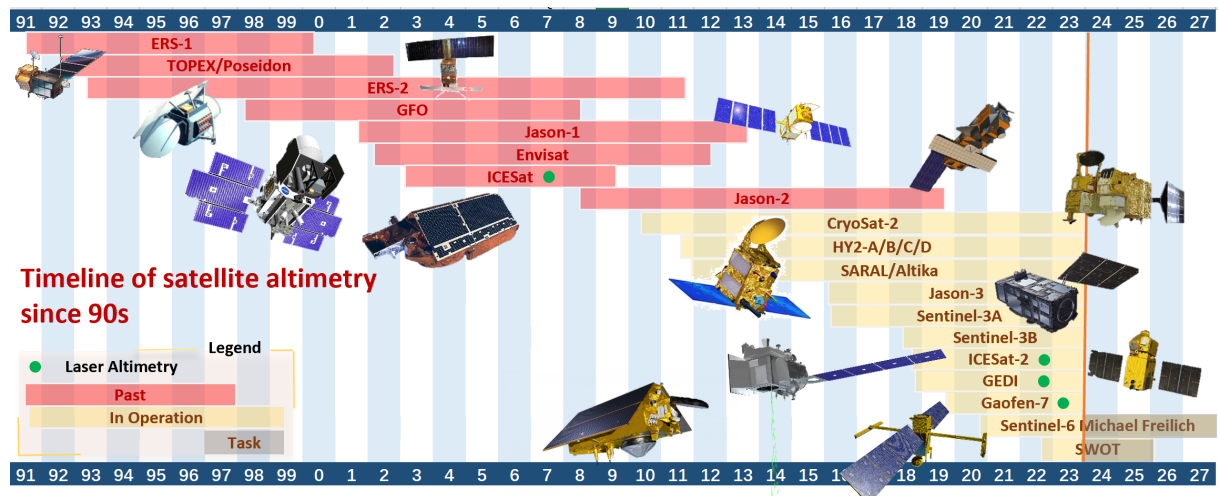


Figure 2.1.: Timeline of Satellite Altimetry since the 1990s. Modified from Abdalla et al. (2021)

The first altimetry measurements were made by radar instruments on board the Seasat-1 and Geosat satellites, which were launched in 1978 and 1985 respectively (Townsend, 1980). In 1992, The TOPEX/Poseidon mission was launched, produced the first global maps of ocean currents and sea level measurements , such as those associated with El Niño and other ocean-atmosphere interactions (Grgić et al., 2021). During 1990s-2000s, several other altimetry missions were launched, including Jason-1, ENVISAT, CryoSat-1, and Jason-2, among others (Figure 2.1). These missions greatly improved our understanding of the Earth's oceans, ice sheets, and land surfaces (Abdalla et al., 2021; Sandberg Sørensen

2. Scientific Overview

et al., 2018). However, there are major limitations of radar altimetry: - One of the most notable is its large footprint diameter on the ground, which results in an averaged elevation measurement over a broadened surface area, obscuring small-scale features such as crevasses and ridges (Grgić et al., 2021). - Additionally, radar altimetry detects topographic highs early, as soon as they enter footprint, making it difficult to relocate measurements over rough terrain due to slope-induced errors (Brenner et al., 1983). - For snow detection, radar altimeter pulse penetrates the snow surface (Connor et al., 2009), leading to volume scattering within the snow-pack. Effect increases in the dry snow zone and high accumulation areas.

In 2003, NASA launched the the Ice Cloud and Land Elevation Satellite (ICESat) (Schutz et al., 2005), which used a laser altimeter to measure the height of the Earth's surface, marked a major advancement in satellite altimetry. The unprecedented accuracy (Brenner et al., 2007) reveals unprecedented details on ice thickness, such as sea-ice freeboard and thickness (Kwok & Cunningham, 2008), Antarctic ice-sheet loss (Pritchard et al., 2012), subglacial lake drainage (Palmer et al., 2015).

In comparison, laser altimetry has several advantages over radar altimetry, including smaller footprints, higher spatial resolution, and ability of detecting both ground surfaces and canopies, light penetration on snow surface (Deems et al., 2013). However, laser altimetry is more susceptible to atmospheric conditions and has a narrower field of view that limits its coverage capabilities (Wang et al., 2011).

2.1.2. ICESat-2

As the successor to ICESat, ICESat-2 was launched in September 2018 by the National Aeronautics and Space Administration (NASA) and provides worldwide photon counting lidar data over land surfaces, vegetation canopies, water bodies, sea ice, and ice sheets (Neuenschwander & Pitts, 2019). ICESat-2 operates at an orbit height of approximately 486 km with a near-polar orbit (92° inclination) and a 91-day cycle. During this cycle, the ground track shifts laterally to increase coverage. The instrument has three beam pairs separated at 3.3 km, with each beam having a strong and weak beam in 90 m. There is a power differential of approximately 4:1 between the strong and weak beams that allows for high- and low-reflectance surfaces to be measured (Markus et al., 2017).

When ICESat-2 flies over an area, it emits 532 nm laser pulses at a repetition rate of 10 kHz from the Advanced Topographic Laser Altimeter System (ATLAS). Approximately 10^{14} photons travel horizontally to hit upon the surface with a spread of approximately 13-17 m. The instrument measures surface elevations every 70 cm by detecting photons returning back to ATLAS telescope's focal plane as many photon events (Figure 2.2) (Markus et al., 2017; Neuenschwander et al., 2022; Neuenschwander & Pitts, 2019). The individual photon events are geolocated into an XYZ point by measuring traveling time and precise location of satellite. To produce actual surface measurements, individual photon events must be accumulated and statistically analyzed (Figure 2.2). Hence, the elevation precision

2.1. Satellite Altimetry

depends on the number and distribution of returned photons, which varies according to surface geometry, reflectance, atmospheric effects, and solar background noise (Neumann et al., 2021; Smith et al., 2019).

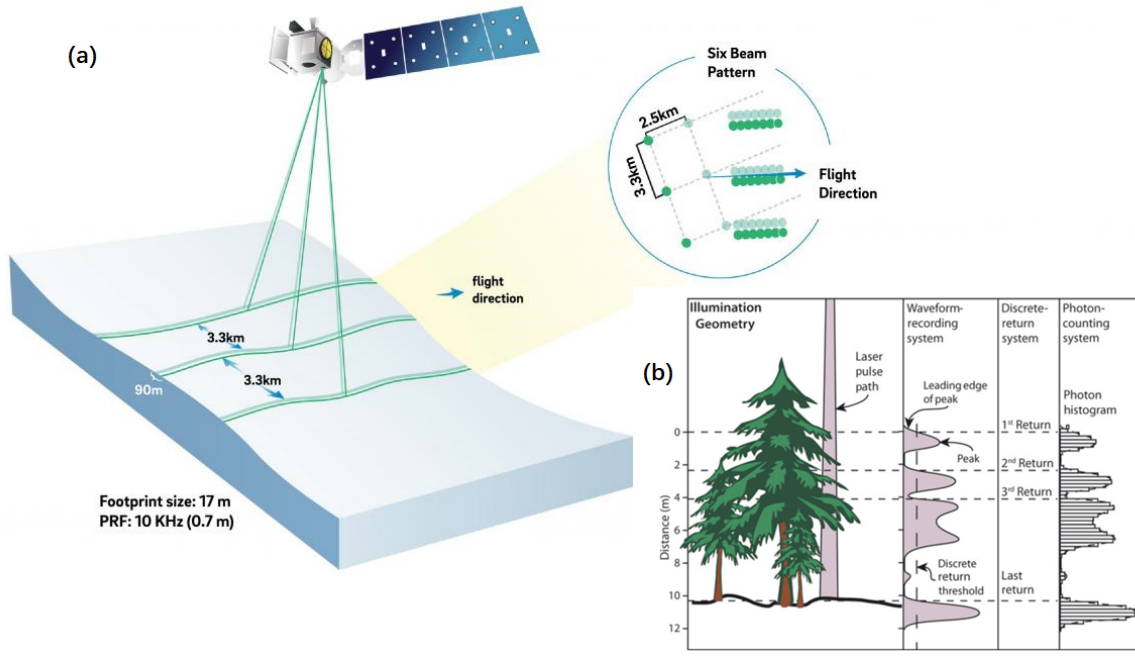


Figure 2.2.: The ICESat-2 and Photon Counting System. The ICESat-2 is equipped with six laser beams that are arranged into three pairs, allowing for improved coverage (a). Unlike its predecessor, the ICESat-2 employs a low-power system known as photons counting lidar to manage the signals generated by the laser beams. This system uses probability distribution function (PDF) analysis to process the signals (b). Adapted from Deems et al. (2013); Smith et al. (2019)

The photons then are classified into terrain photons or canopy photons in order to catch the ground surface and canopy heights. The process get through two basic steps (more technical destails in Appendix A.2):

- *Signal finding.* The first step of process is indentifying signal photons from background noise. ATL03 use histogramming approach, and ATL08 use DRAGANN (Differential, Regressive, and Gaussian Adaptive Nearest Neighbor) algorithm, which has better performance over vegetated areas but also includes small noise clusters (Neuenschwander & Pitts, 2019).
- *Photons classification.* The topography elevation from DEM are used to de-trend the signal photons, producing the flat surface. Then, with the help of landsat Vegetation Continuous Field (VCF) product, the photons located in 5-meter-height-vegetation of pixels but also above the flat surface are label as canopy (Neuenschwander & Pitts, 2019). Finally, higher availability of photons translates to higher signal-to-noise ratio and typically greater elevation precision.

2. Scientific Overview

2.2. DEM and Co-registration

2.2.1. DEM products

The digital elevation model (DEM) is a widely used representation of the Earth's surface in a fixed grid, triangulated irregular network (TIN), and point cloud. Two primary types of DEM are the digital terrain model (DTM) and the digital surface model (DSM), which incorporate man-made structures and vegetation. These models can be generated using various spaceborne remote sensing techniques such as stereoscopic satellite imagery or Synthetic Aperture Radar (SAR) (Rosen et al., 2000). Alternatively, they can also be generated using airborne remote sensing methods like LiDAR, photogrammetry or ground-based survey methods like laser scanning (X. Liu, 2008; Westoby et al., 2012) at the local and regional scales.

It is noteworthy that radar-based DEMs can penetrate dry snow surfaces, thereby resulting in nearly snow-free DEMs (more discussion in Section 1.3). On the other hand, while photogrammetry and LiDAR DEMs often offer higher resolution compared to other methods, but they are not entirely free of snow.

Table 2.1.: Global DEM products.

| DEM | Acquired | Primary Source | Spacing (m) | Coverage |
|------------------------|--------------|-------------------------|-------------|-----------------------------|
| SRTM (v3) | 2000 | C band Radar | 30, 90 | Global except high latitude |
| ASTER GDEM | 2000-2013 | Stereo imagery | 30 | Global except high latitude |
| TanDEM-X | 2010-2011 | X band Radar | 90 | Global |
| Copernicus DEM | 2010-2015 | TanDEM-X, WorldDEM | 30, 90 | Global |
| NASA DEM | 2000 | Reprocessed SRTM | 30 | Global |
| MERIT | 2000-2013 | Reprocessed SRTM, ASTER | 90 | Global |
| ArcticDEM, EarthDEM | 2007-Present | Stereo imagery | 2 | Global |

2.2.2. DEM uncertainties

DEM suffers from various types of errors and biases throughout the acquisition and processing stages. These include above-ground objective biases, interpolation errors, stripe noise and so on, which can significantly affect the accuracy and reliability of DEMs.

Despite the wide range of applications of DEMs and the technological advances used for their creation, quality assessment of DEM remains an open question as there are no specific guidelines available for it (Mesa-Mingorance & Ariza-López, 2020). For instance, describing the error distribution of DEMs using a single estimator of dispersion is challenging (Oksanen & Sarjakoski, 2006). Moreover, the sampling points utilized cannot be considered a reliable representation of the overall accuracy of the DEM.

One of the practical approach to evaluate the quality of DEM is to compare it with a reference DEM over stable terrain, excluding snow cover, glaciers, landslides, volcanic uplifts and dense forest, having a further analysis on residual differences. When referring to differences as errors, outliers, noises or biases; we are either referring to “systematic errors” (accuracy or bias) or “random error” (precision or variance). Figure 2.3 provides a framework of the uncertainties associated with DEMs (Hugonet et al., 2022).

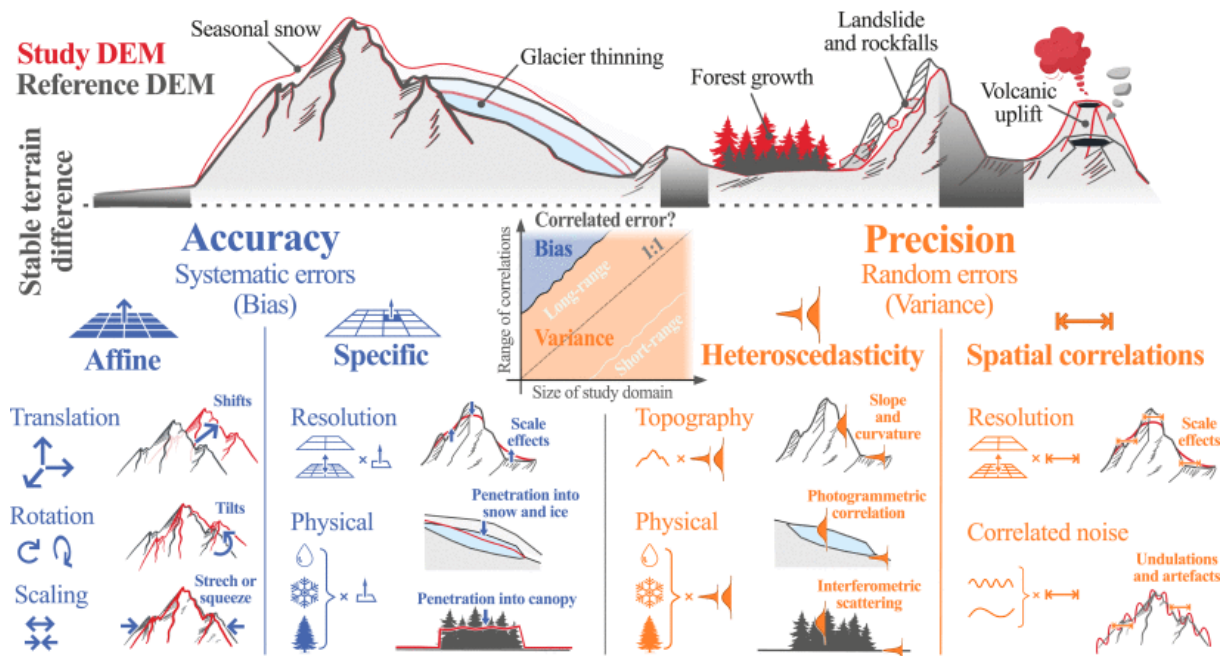


Figure 2.3.: Uncertainty Framework for DEM Assessment. Source: Hugonet et al. (2022)

An error distribution is typically described by its mean and variance. However, this description cannot fully account for non-stationary errors that are more commonly observed in real-world scenarios. These non-stationary errors include situations where a single mean and variance value cannot provide an adequate explanation. As a result, estimation becomes increasingly challenging under such conditions.

The systematic bias can result from 3D affine, such as shifts, rotations or scaling. This type of bias is common across all types of elevation data, but it can be minimized through co-registration techniques (Nuth & Kääb, 2011) (see Section 2.2.3 for further discussion). Additionally, specific systematic errors

2. Scientific Overview

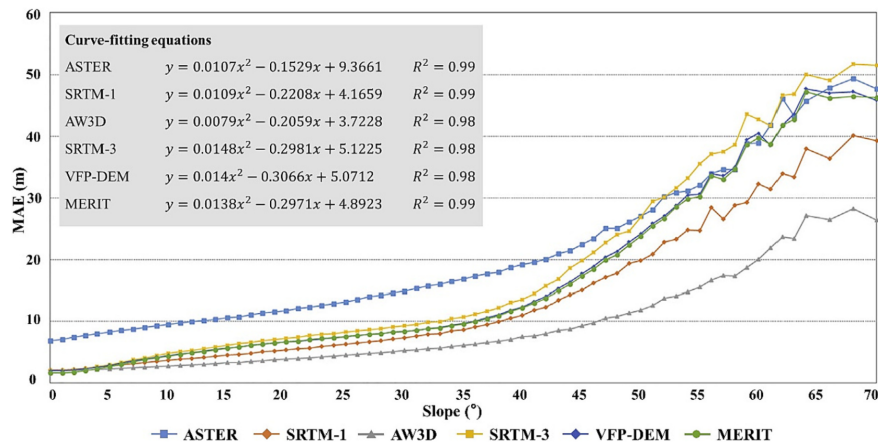


Figure 2.4.: Mean Absolute Errors of Global DEM Products in the Tibetan Plateau. Source: Xiong et al. (2022).

may arise due to resolution or physical conditions, such as instrumental inherent errors (Girod et al., 2017), or surface conditions like snow coverage and vegetation. If we can identify and describe these specific systematic errors accurately, we may be able to apply bias correction techniques to mitigate their effects.

There are various metrics that can be utilized to describe bias, such as the mean error (μ) and median error. Additionally, skewness, which is determined by considering the relationship between mean and median, is a measure of the asymmetry of a probability distribution. This metric indicates whether data is skewed to the left or right of the mean, but it does not provide information about the magnitude of errors.

Heteroscedasticity refers to a situation where the variance changes over space. This can be observed over the slope (Figure 2.4) (Xiong et al., 2022), curvature and other terrain domain. Unlike the mean, which can indicate the direction of error, variance does not exhibit any direction of error; instead, it reveals the magnitude of the spread of errors. While improving heteroscedasticity is often challenging, it is possible to assess and eliminate measurements that do not conform to ideal standards. For instance, in practice, outliers are often identified using $3 \cdot \text{RMSE}$ (Root Mean Squared Error) or $3 \cdot \sigma$ (Standard Deviation).

However, it is important to note that certain measures, such as mean, root mean square error (RMSE), and standard deviation, are significantly susceptible to the presence of outliers. As a result, to ensure more accurate and reliable results, robust estimators such as the median and normalized median absolute deviation (NMAD) are recommended (Höhle & Höhle, 2009). The NMAD is proportional to the median of the absolute differences between errors and the median error. To perform uncertainty analysis effectively, researchers can consider utilizing these metrics:

$$\mu = \frac{1}{n} \sum \delta h \quad (2.1)$$

$$\text{Pearson's second skewness} = \frac{3 \cdot (\mu - m_{\delta h})}{\sigma} \quad (2.2)$$

$$\text{RMSE} = \sqrt{\frac{1}{n} \sum \delta h^2} \quad (2.3)$$

$$\sigma = \sqrt{\frac{1}{n-1} \sum (\delta h - \mu)^2} \quad (2.4)$$

$$\text{NMAD} = 1.4826 \cdot \text{median}(|\delta h - m_{\delta h}|) \quad (2.5)$$

where δh is the sample of elevation difference and n is the number of samples. $m_{\delta h}$ is the median of the samples.

2.2.3. DEM Co-registration

Registration of three-dimensional objects is a common problem in computer vision, for which various solutions exist. Similar issues also arise in satellite image registration and DEM co-registration. For instance, the Iterative Closest Point (ICP) algorithm (Besl & McKay, 1992) is commonly used for registering two sets of rigid point clouds into a single coordinate system, which can also be applied to DEM co-registration. The algorithm iteratively matches corresponding points, computes the transformation that aligns the points, and then applies the transformation to the points until convergence.

There are numerous co-registration methods available, differing mainly in how they minimize differences due to mismatching. The Least Squares 3D Surface Matching (LS3D) algorithm treats it as a least square process of the Euclidean distances of overlapping surfaces (Gruen & Akca, 2005). Feature point-based methods reduce computation by solving the problem on selected points such as centroids of sub-watersheds (H. Li et al., 2017). All these methods require costs to establish correspondences.

The NuthKaab co-registration method (Nuth & Käab, 2011) elegantly solves this issue by identifying that statistic patterns of elevation differences that are related to slope and aspect. This method has become a standard procedure in high-accuracy cryosphere applications (W. Chen et al., 2022; Hugonnet et al., 2021; Vacaflo et al., 2022) due to its efficiency and effectiveness. However, this method is not efficient for high-resolution DEMs and initially does not support rotations.

2. Scientific Overview

Grid search methods shift the slave DEM stepwise in a predefined window but are considered rarely used due to their brute-force search process being computationally expensive (T. Li et al., 2022). This study recognizes these shortcomings and addresses them with a new algorithm (see Section 3.3).

2.3. Machine Learning and XGBoost

Machine learning (ML) is a subset of artificial intelligence that involves the development of systems capable of learning from training dataset to identify patterns and relationships, and subsequently make predictions or decisions on new data.

Two main types of machine learning exist: supervised and unsupervised. In supervised learning, a mapping function (F) is established based on labeled input variables (X) and output variables (y):

$$y \sim F(X) \quad (2.6)$$

Where the mapping function can be as simple as linear regression or as complex as tree structures:

- Linear regression. The function describes the linear relationship between X and y .
- Logistic regression. The function based on linear relationship but output binary results.
- Decision trees. The function consists of multiple leaf nodes of the tree, each internal node represents a decision or test on input variable. The goal is to find a set of decision rules that minimize the error and make a correct decision (Kingsford & Salzberg, 2008).
- Random forests (Breiman, 2001). The function combines multiple decision trees (ensemble learning algorithms) in parallel to improve performance and reduce overfitting via “bagging”.
- GBDT (Gradient-Boosting Decision Tree). An ensemble learning algorithm that uses sequential weak trees and updates input data point weights based on residuals for improved performance via “boosting”.
- XGBoost (Extreme Gradient Boosting). A specific implementation of GBDT that uses optimization techniques (Rashmi & Gilad-Bachrach, 2015) to accelerate training processes while improving accuracy (T. Chen & Guestrin, 2016).

XGBoost builds an ensemble of decision trees. Each tree consists of nodes that represent decision rules, which split the data into smaller subsets based on the input features. The objective function measures the difference between the predicted values and labeled actual values, and is optimized through gradient boosting. The final prediction is the sum of predictions from all the individual trees in the model (Figure 2.5).

Additionally, XGBoost provides additional regularization techniques, including L1 and L2 regularization terms, and a built-in mechanism for handling missing values in the input data. These regularization techniques help prevent overfitting and improve the generalization performance of the model.

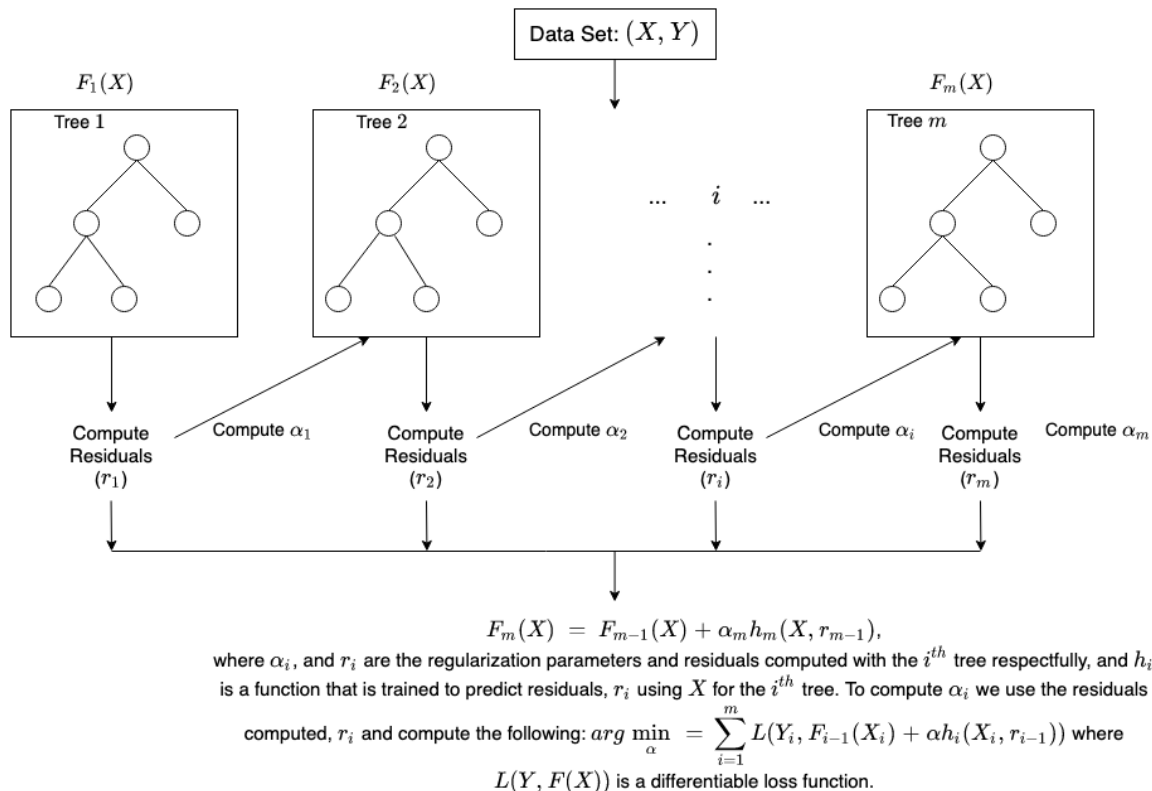


Figure 2.5.: How XGBoost Works. Source: Developer guide by Amazon (2023)

2. Scientific Overview

2.4. Climate Reanalysis and Downscaling

Normal climate archives or regional observations may have gaps, inconsistencies, biases, or uncertainties induced from different sources, methods. In order to use as much information as possible and derive a comprehensive description of climate in the past and present, the climate reanalysis are produced (Dee et al., 2014). By assimilating observations from different sources with numerical models that simulate the Earth's atmosphere, land, and oceans, it offers a long-term description of past weather condition and climate variability under a physically consistent model framework (Laloyaux et al., 2016).

ERA-Interim, ERA5 and ERA5 Land are widely used reanalysis datasets produced by the European Centre for Medium-Range Weather Forecasts (ECMWF). ERA-Interim is the previous generation of ECMWF reanalysis that covers the period from 1979 to 2019 with a spatial resolution of about 80 km. ERA5 is the latest generation of ECMWF reanalysis that covers the period from 1950 to present with a higher spatial resolution of about 30 km and more atmospheric levels (Dee et al., 2011; Hersbach et al., 2020). ERA5 Land is a subset of ERA5 that produces a total of 50 variables describing the water and energy cycles over land, globally, hourly, and at a spatial resolution of 9 km (Muñoz-Sabater et al., 2021).

However, reanalysis datasets still have quality issues due to sparse and unreliable observations, and bias from inconsistency of models. And the coarse resolution also limited its applicability for regional applications, which has motivated the downscaling global reanalysis into finer-scale regional reanalysis (Wilby & Wigley, 1997). There are two main methods of climate reanalysis downscaling: dynamical and statistical.

- (a) Dynamical downscaling involves using physically based models that simulate atmospheric dynamics and physics at finer resolutions, with global reanalysis or global climate model data serving as boundary conditions. While this approach can provide a full suite of climate variables with good spatial coherence and physical consistency, it is computationally expensive. (Fowler et al., 2007). The accuracy of this method is affected by uncertainties from forcing data and model parameterizations.
- (b) Statistical downscaling is a method that utilizes empirically based formulas, such as regression models, to establish statistical relationships between large-scale reanalysis and local observations of climate variables (Maraun & Widmann, 2018). This approach may be sensitive to the quality and representativeness of the input data and may not capture the complex physical processes and feedback at the local scale, especially for extreme events (Fowler et al., 2007).

The statistical downscaling approach assumes that there exists a stationary empirical relationship between large-scale and local observations, which is commonly referred to as “perfect prognosis” (PP) by climatologists. The downscaling can be applied not only to climate reanalysis but also to model-based atmospheric variables, referred to model output statistics (MOS). MOS focuses on downsizing

2.5. Literature highlights

model-based predictors that are often biased from observations. Hence, this approach is known as bias correction (BC) downscaling (Maraun & Widmann, 2018).

In summary, both dynamical and statistical downscaling have advantages and limitations in providing high-resolution climate data. The choice of method should depend on specific research goals, available computational resources, quality of input data, and other relevant factors such as trends and extremes.

2.5. Literature highlights

2.5.1. Addressing DEM errors by ICESat-2

The laser altimetry technique is highly precise in providing ground elevation control points for DEMs, as demonstrated by previous studies involving ICESat (Atwood et al., 2007; Gruber et al., 2012; Tang et al., 2020; Yamazaki et al., 2017). However, due to its limited spatial coverage in comparison to radar altimetry, it cannot be used independently to create moderate resolution DEMs with resolutions ranging from 30-100 meters. Nevertheless, the latest ICESat-2 mission presents new opportunities for assessing DEM uncertainties (W. Chen et al., 2022; H. Li et al., 2022). Recent research proposes a two-dimensional bias correction method (Magruder et al., 2021) for SRTM using data obtained from ICESat-2 ATL08 product and vegetation product from Landsat, leading to enhanced accuracy as shown in Figure 2.6.

However, the study (Tian & Shan, 2021) discovered that the ATL08 product tends to underestimate terrain height in areas with significant terrain slopes (0.5 m for mean bias and 2 m for variance) while overestimating it in regions covered by dense vegetation. This was observed through a comparison with a 1m lidar reference DEM. Another case study, utilizing the same year of lidar reference DEM, has revealed that the ATL08 elevations exhibit a correlation with slope. Specifically, the bias increases from 0 m to 1 m, and the root-mean-square error (RMSE) increases from 0.6 m to 7.5 m for slopes ranging from less than 5° to greater than 30° (A. Liu, 2021). It is important to note that these findings emphasize the need for comprehensive evaluation before utilizing the ICESat2 products in snow depth retrieval, particularly when dealing with complex terrain (see Section 3.4.1 for further discussion).

2.5.2. Snow depth from ICESat-2

Since the first attempt on ICESat (Treichler & Käab, 2017) by differencing satellite laser snow-on measurements with snow-off DEM to derive snow depth, there are several different attempts on snow depth retrieval by ICESat-2:

2. Scientific Overview

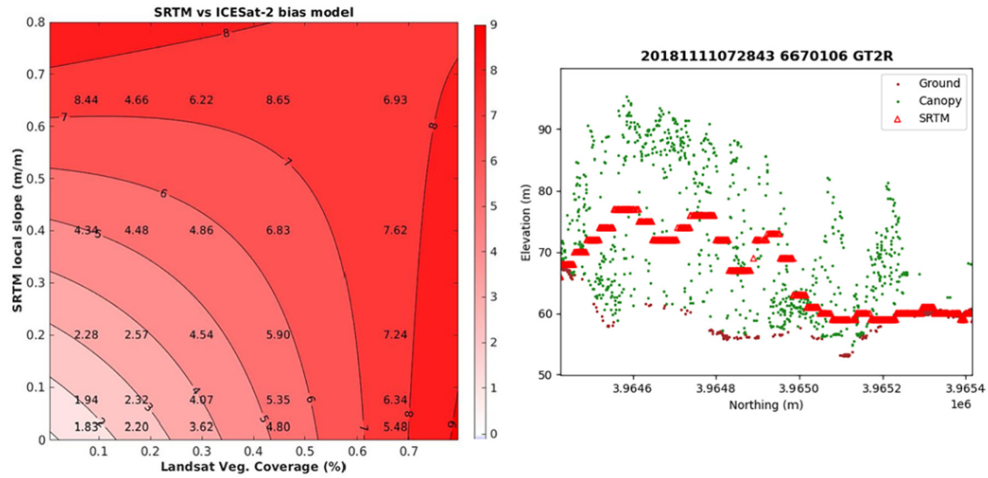


Figure 2.6.: A Bias Correction Scheme for DEMs Based on Slopes and Vegetation Coverage. The flat terrain and sparse vegetation has lower bias (a). An example transect of the comparison demonstrate that (b). Source: Magruder et al. (2021)

- Snow depth derived from ATL06 yielded an accuracy of 0.2 m (bias), a precision (NMAD) of 0.5 m for low slopes and 1.2 m for steeper areas, compared to airborne lidar snow depth (Deschamps-Berger et al., 2022).
- The study case found over flat area ($\text{slope} < 1.5^\circ$) and thin snowpack (< 40 cm) the ‘crossover differences’ (snow-on-snow-off-differencing) shows considerable accurate snow depth with RMSE of 4.20 cm (Hu et al., 2022).
- A case study in Alaska’s Kenai Mountains reveals the snow depth has MAD varying from 0.2 m for slopes $< 5^\circ$ to over 1 m for slopes $> 20^\circ$. The ATL08 are only suggested in unglacierized mountain regions with relatively low-slopes and sparse vegetation cover. (Enderlin et al., 2022)

However, these studies (Deschamps-Berger et al., 2022; Enderlin et al., 2022) do not correct bias or inconsistency between the reference DEM and ICESat-2 elevation measurements, which introduces uncertainties into the final results (see Section 2.5.1). Additionally, the use of global DEM such as Copernicus GLO30 for snow depth retrieval is considered too imprecise. While slope-dependent adjustments partially remove the negative skewness of ICESat-2 ATL08 in some cases, large uncertainties remain (Enderlin et al., 2022), indicating that a more comprehensive approach is needed to address unstationary biases.

Most remote sensing techniques are constrained by temporal and spatial limitations, including ICESat-2. The poor temporal and spatial coverage of ICESat-2 derived snow depth limits its utility. One potential solution to this issue is to assimilate snow observations into a snow model (Girotto et al., 2020) or perform dynamical downscaling with climate models (Wang, 2022) to produce spatially complete products. Alternatively, statistical downscaling can be used to develop an empirical relationship be-

tween the subgrid distribution of snow depth and the data from climate models or climate reanalysis.

2.5.3. Subgrid variability of snow and statistical downscaling

Downscaling topography-based variables such as temperature, humidity, wind speed, and radiation has been achieved in previous studies (Fiddes et al., 2022; Fiddes & Gruber, 2014). However, accurately capturing snow depth variability within a given grid cell remains a challenging task. This is largely due to the complexity of physically-based models that need to account for vegetation-snow interactions and wind redistribution. Additionally, the availability of forcing data at hillslope scales, such as precipitation and wind in remote mountains, further complicates the modeling process. As a result, physically-based models face many challenges and limitations. They either have limited coverage area or too coarse resolution to address subgrid distribution (Freudiger et al., 2017) (see Figure 2.7).

Meanwhile, the distribution patterns of snow display a notable resemblance year after year because they rely on factors such as topography, vegetation, and consistent synoptic weather patterns (Sturm & Wagner, 2010; Trujillo et al., 2007). This similarity lends support to an empirical resolution from statistical downscaling.

- Grünwald et al. (2013) used high-resolution lidar snow depth in seven different mountain regions and applied statistical modeling to assess the spatial variability of the snow depth. The results showed that by aggregating snow accumulation on a larger scale, up to 91% of the snow depth variability can be explained by local models calibrated to specific study areas. Elevation, slope, northing, and wind sheltering parameters were found to be good predictors of snow distribution. However, coefficients differed among the catchments. A general model combining all data from different regions could only explain 23% of the variability. Models developed in one peak snow season were found to be good predictors for other peak snow seasons.
- Another study (Melvold & Skaugen, 2013) presents results from a snow survey on the mountain plateau Hardangervidda, Norway, in 2008 and 2009 at maximum snow accumulation season. The study found large variability in snow depth at a local scale, ranging from 0 to 10 m, but similar spatial patterns in accumulation between 2008 and 2009. The regional-scale spatial pattern of snow depth is captured by the seNorge but relatively large differences at 1 km scale because the degree days model is not able to capture the physical processes associated with the subgrid-scale temporal and spatial variability of snow.
- Gisnås et al. (2016) statistically derived snow distributions within 1 km² grid cells were used as input to a regional permafrost model to represent sub-grid variability of ground temperatures. The snow distributions within areas of 1 km² in Norwegian mountain environments are closer to a gamma than to a lognormal theoretical distribution.

2. Scientific Overview

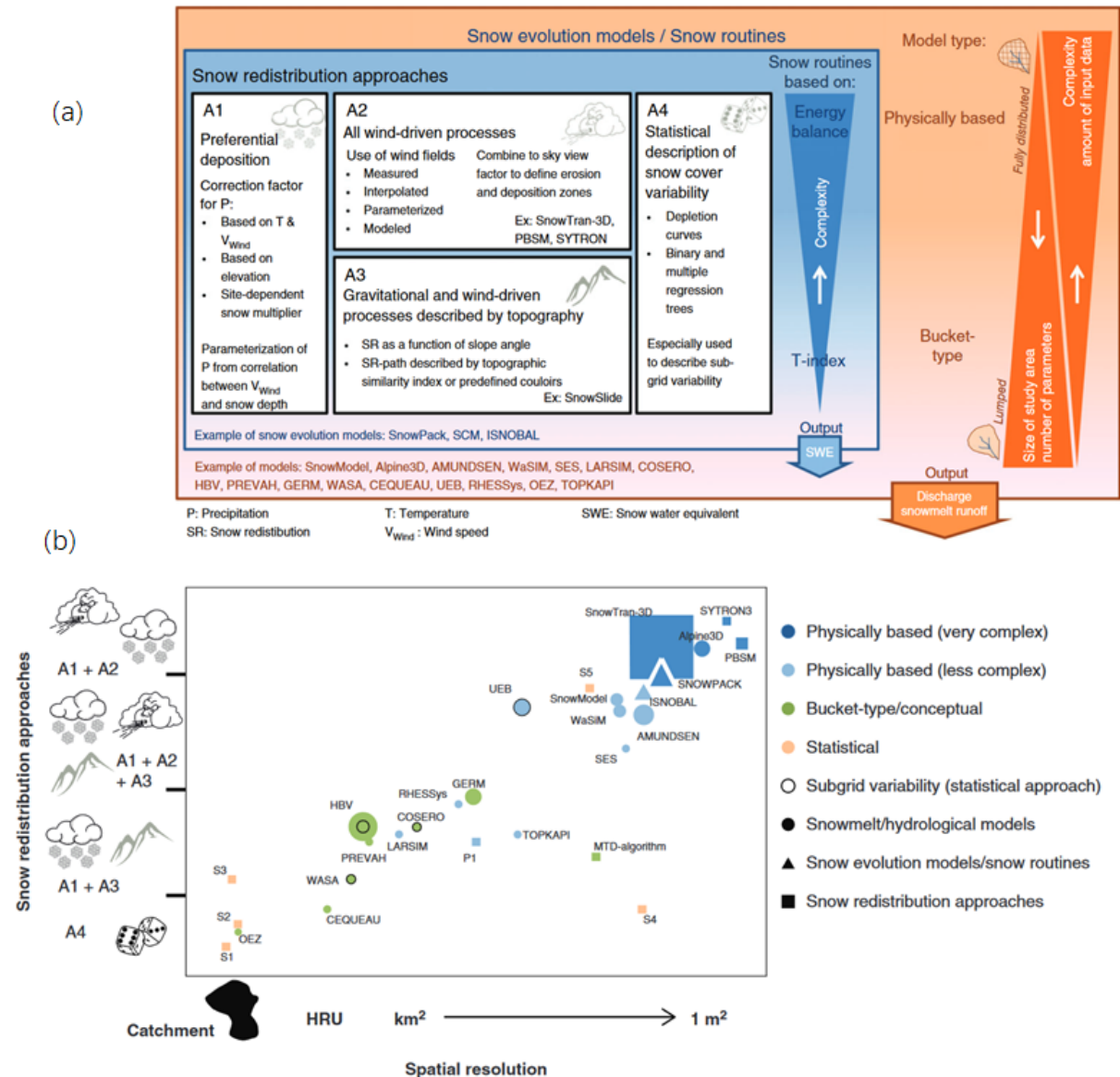


Figure 2.7.: An Overview of Models for Snow Redistribution. These approaches can be broadly classified into four categories: (A1) the correction of precipitation data; (A2) wind-driven processes; (A3) gravitational transportation and/or wind-driven processes; (A4) statistical description (a). The more complexity of model (the size of objects), the coarser spatial resolution (b). Adapted from Freudiger et al. (2017)

2.5. Literature highlights

There is a growing interest in exploring the subgrid distribution of snow and characterizing snow accumulation patterns. Most studies have used airborne laser to investigate these patterns and have found that they tend to repeat. Some studies have attempted to use covariance to describe subgrid distribution and make regression models more applicable. However, these models only survey the maximum snow depth at the end of snow season, which limits their applicability to different time periods. Moreover, they may not be applicable to other catchments due to climate differences.

In conclusion, machine learning has emerged as a promising approach for downscaling climate variables (Hobeichi et al., 2023; Sachindra et al., 2018). It can handle large datasets with numerous predictors, account for complex relationships between predictors and responses, and capture nonlinearities in the data. The solution combined the huge dataset from satellite observations and machine learning could a possible way to address subgrid distribution problem of snow.

In conclusion, there is currently a growing interest in exploring the wind redistribution of snow and understanding its accumulation patterns at a subgrid level. Most studies have relied on airborne laser to investigate these patterns, revealing that they tend to repeat over time. Some researchers have attempted to use covariance to describe subgrid distribution and make regression models more applicable. Nevertheless, these study cases have limitations as they only survey maximum snow depth at the end of the snow season and cover limited study areas that may not be generalizable to other catchments due to climate differences.

To overcome these limitations, machine learning has emerged as a promising approach for downscaling climate variables (Hobeichi et al., 2023; Sachindra et al., 2018). This approach has demonstrated effectiveness in managing large datasets with numerous predictors and can capture complex relationships between predictors and responses while accounting for nonlinearities in the data. It offers a potential solution for subgrid snow distribution problem.

3. Methodologies

3.1. Research Design

Calculation of snow depth from lidar data requires two co-registered data collections, one for snow-free bare-ground and one for snow-covered, followed by elevation differencing (Deems et al., 2013), which works in the same way as snow depth estimation from satellite laser altimetry. To implement this approach, several technical challenges need to be addressed.

- Firstly, the magnitude of seasonal snow surface elevation change is relatively small compared to the uncertainties associated with digital elevation models (DEMs). Hence, it is crucial to use the latest, fine resolution and most advanced DEM products to achieve accurate measurements. However, obtaining such data may not always be feasible due to factors such as cost and accessibility. Furthermore, this methodology requires a snow-off DEM; thus high-resolution Arctic DEMs are not applicable.
- Secondly, while the commonly used NuthKaab coregistration (Nuth & Kääb, 2011) is effective in most cases, it struggles with different resolutions and computationally-intensive tasks. Particularly for fine resolution and large scale DEMs required by this workflow. And this process can be time-consuming.
- Thirdly, biases are widely present in DEMs. It calls the need of quality control and correction.
- Lastly, the satellite's acquisition pattern is sparse both in time and space resulting in a need for additional data to produce a spatially complete snow-depth map.

To address these challenges effectively, three key steps are necessary: co-registration of datasets; bias correction; and statistical downscaling as shown in Figure 3.1. The ICESat-2 data is first split into two categories: snow-free and snow-on segments. Subsequently, the snow-free segments are used in co-registration and fed into bias correction of snow-free DEMs. The same bias corrections are then applied to derive snow depth. Finally, the derived snow depth is used in downscaling.

3. Methodologies

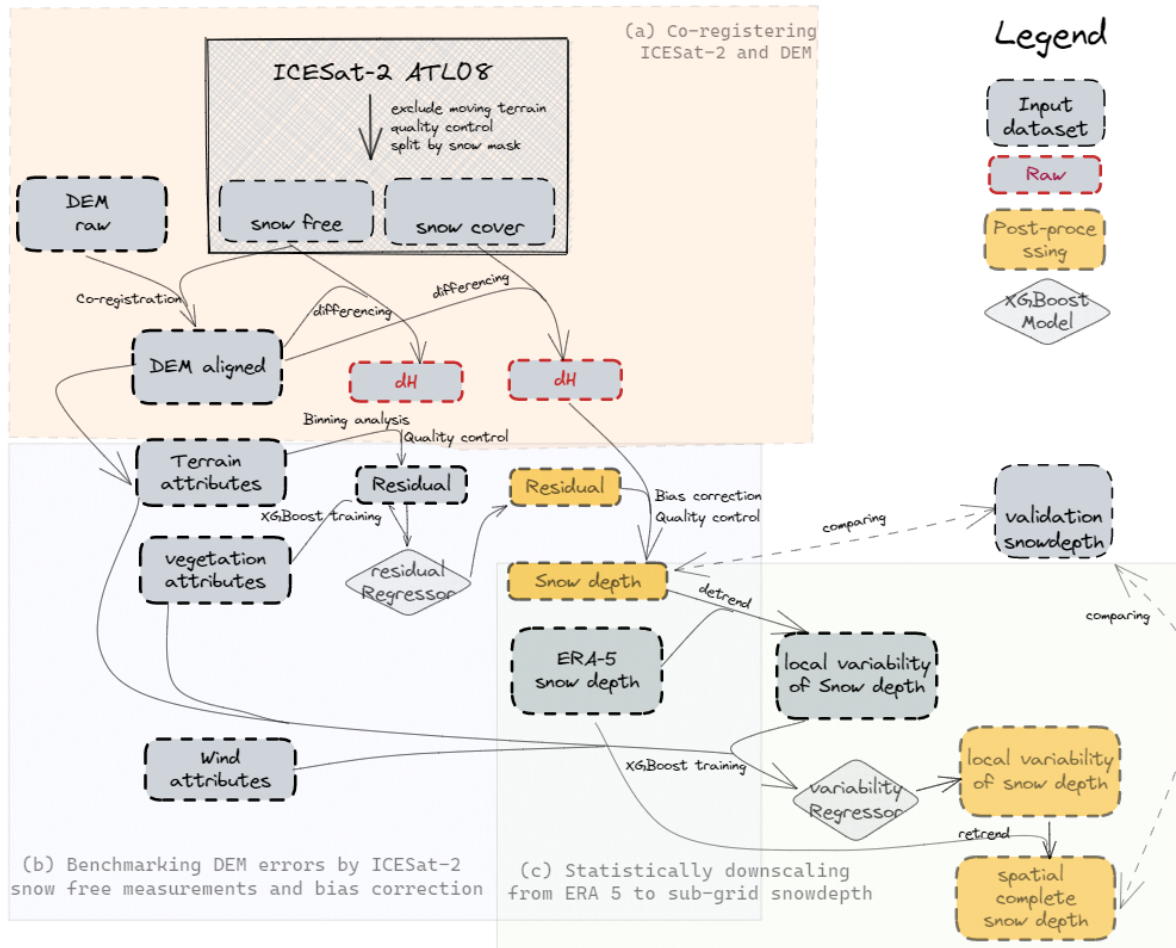


Figure 3.1.: Study Design Schematic. Firstly, DEMs are aligned to generate raw elevation differences (a). The snow-off segments, terrain and vegetation features are utilized as training data for a regressor that can eliminate biases for snow-on segments (b). By subtracting the snow depth with ERA-5 snow depth, enabling us to depict local variability of snow depth. Finally, another regressor for downscaling is trained and implemented to predict local variability of snow depth in any location and at any time (c).

3.2. Data Preparation

3.2.1. ICESat-2 ATL08

The ATL08 product from ICESat-2 provides global geodetic measurements of terrain surface and relative canopy heights. The measurements consist of fixed segment sizes of 100 meters along the ground track. The following features of the ATL08 segments have been utilized:

- *latitude and longitude*: representing the location of the midpoint of the segment.
- *date*: representing the acquisition date.
- *h_te_best_fit*: representing the best-fit terrain elevation at the 100-meter segment midpoint location, which is determined by polynomial fitting to terrain photons with slope correction and weighting applied. Some studies showed that *t_te_best_fit* has slightly higher accuracy and smaller variation than the *h_te_interp* (Neuenschwander & Pitts, 2019; Tian & Shan, 2021). As such, this study uses it thereafter.
- *n_te_photons*: representing the number of terrain photons within the segment. Likewise, *h_te_skew* (skew of terrain height for segment), *h_te_std* (standard deviation of terrain height), *h_te_uncertainty* (the sum of uncertainties such as geolocation, pointing angle, timing, etc) are used to describe the quality, status of elevation of segment.
- *snowcover mask*: dividing the dataset into snow-free land surface and snow surface by using daily snow-cover masks from NOAA daily snow cover products (Neuenschwander et al., 2022).
- *segment_watermask*: water mask from Global Raster Water Mask at 250-meter spatial resolution (Carroll et al., 2009).
- *segment_landcover*: land-cover labels from Copernicus Global Land Cover 100 m (Buchhorn et al., 2020).
- *h_mean_canopy*: For the segments where the proportion of classified photons classified as canopy photons exceeds a certain threshold (5%), this value represents the mean canopy height of the segments.(Neuenschwander et al., 2022).
- *h_te_uncertainty*: Uncertainty of mean terrain height incorporates all systematics uncertainties, such as timing, orbits, geolocation, slope...(Neuenschwander et al., 2022).
- *canopy_openness*: signifying the standard deviation of relative heights for all canopy photons within a segment. This parameter potentially indicates canopy openness, as greater standard deviation indicates greater penetration of laser energy into the canopy.
- *segment_cover*: woody vegetation fractional cover derived from Copernicus Global Land Cover 100 m (Buchhorn et al., 2020).
- *subset_te_flag*: Each segment comprises five geosegments, and *subset_te_flag* denotes the number of geosegments included in each subset. With a value of 5, all available geosegments are continuous.

3. Methodologies

- *brightness_flag*: indicating the snow cover and other hight reflectivitive surface object. this is a good alterlative when snowcover mask is not accurate enough (Neuenschwander et al., 2022).

Prior to differencing the DEMs, this study excludes moving terrain based on the *segment_watermask* and *segment_landcover* mask. Moving terrain is defined as the type of topography that lacks stable elevation during the period of DEM production and ICESat-2 visit, including inland water bodies, permanent snow and ice, and open sea. However, it is crucial to acknowledge the existence of potential biases that may arise from surface mass movement, such as landslides, significant erosion or deposition. These biases are more likely to occur in outdated DEMs and can have a considerable impact on regional accuracy.

The measurements are categorized into two groups: snow-free or snow-on categories using the *snowcover mask*. The *brightness flag* further excludes any suspicious snow-on measurements from the snow-free category. To eliminate ICESat-2's outliers, this study excludes segments with few n_te_photons ($N < 10$) or h_te_best_fit labeled by NaN (no data), and only keeps subset_te_flag equals 5 as part of quality control procedures.

3.2.2. DEM products

The Copernicus GLO-30 is a 1-arcsec Digital Surface Model (DSM) using Synthetic Aperture Radar (SAR) interferometry acquired from December 2010 to January 2015 during the TanDEM-X mission. It covered the entire Earth's land mass and filling all voids by multiple sources. The products are provided in Geographic Coordinates, with the horizontal reference datum of the World Geodetic System 1984 (WGS84, EPSG:4326), and the vertical reference datum of the Earth Gravitational Model 2008 (EGM2008, EPSG:3855).

The FABDEM (Forest And Buildings removed Copernicus DEM) is the DTM version of Copernicus GLO 30. It removes buildings and trees based on random forest algorithem and imporved the overal performance of DEM (Hawker et al., 2022).

For study case of mainland Norway (*Chapter 4*), the follong regional DEM are also used: - The *DTM1* was developed by the Kartverket's National Detailed Height Model (NDH) project (©Kartverket), launching in 2016 and is being acquired continuously with country-widet by the end of 2022. The grid resolution of the model is 1x1 meter, using the ETRS89 - UTM33N (EPSG:25833) coordinate system and NN2000 as the vertical reference datum. - The *DTM10* is derived from the *DTM1*, with a spatial resolution of 10 meters.

3.2.3. Terrain and vegetation parameters

The parameters of terrain are derived from 10-m DEM pixels by Python package xDEM (Xdem contributors, 2021) :

- (1) *The elevation difference (dh)* of DEM to reference elevation is defined as:

$$dh = H_{\text{ref}} - H_{\text{DEM}} \quad (3.1)$$

When the ICESat-2 segments (H_{Ref}) is snow-free, the elvataion difference is elevation residuals, when it is snow-on, the elevation difference is snow depth. Due to the difference in sturcture between the gridded DEM and the ICESat-2 points, the elevation difference is interpolated linearly to the point.

- (2) *The slope* of the DEM describes the gradient of each pixel in relation to its neighbours. (3) *The aspect* describes the orientation of strongest slope. And (4) *the curvature* refers to the change in slope, which is divided into planform curvature, perpendicular to the direction of the slope, and profile curvature, parallel to the direction of the slope. A negative profile curvature indicates that the surface is upwardly convex, while a positive value indicates that the surface is upwardly concave where water flow accelerates flowing down. Negative plan curvature means that the surface is sidewardly concave, accompanying convergence of water flow, while positive plan curvature is sidewaard convex.

Specifically, this study calculate terrain attributes, and assign it to the central point by neighboring cells on 3x3 pixel window, namely Zevenbergen & Thorne algorithm (Zevenbergen & Thorne, 1987) :

$$\begin{aligned} Z &= Ax^2y^2 + Bx^2y + Cxy^2 + Dx^2 + Ey^2 + Fxy + Gx + Hy + I \\ A &= [(z1 + z3 + z7 + z9)/4 - (z2 + z4 + z6 + z8)/2 + z5]/L^4 \\ B &= [(z1 + z3 - z7 - z9)/4 - (z2 - z8)/2]/L^3 \\ C &= [(-z1 + z3 - z7 + z9)/4 + (z4 - z6)/2]/L^3 \\ D &= [(z4 + z6)/2 - z5]/L^2 \\ E &= [(z2 + z8)/2 - z5]/L^2 \\ F &= (-z1 + z3 + z7 - z9)/4L^2 \\ G &= (-z4 + z6)/2L \\ H &= (z2 - z8)/2L \end{aligned}$$

3. Methodologies

$$I = z5$$

Z is the surface elevation fit equation on 3x3 pixel window, where $z1$ to $z9$ are the submatrix elevations numbered systematically and $z5$ is the central cell. L is the spacing of cells.

$$\text{Slope} = \frac{\delta Z}{\delta S} = \sqrt{G^2 + H^2} \quad (3.2)$$

$$\text{Aspect} = \arctan\left(\frac{-H}{-G}\right) \quad (3.3)$$

$$\text{Curvature} = 2(D \cos^2 \phi + E \sin^2 \phi + F \cos \phi \sin \phi) \quad (3.4)$$

$$\text{Prof}_c = -\frac{2(DG^2 + EH^2 + FGH)}{G^2 + H^2} \quad (3.5)$$

$$\text{Plan}_c = \frac{2(DH^2 + EG^2 - FGH)}{G^2 + H^2} \quad (3.6)$$

Where the slope is the first derivative of Z , and the curvature for any direction, ϕ , is the second derivative of Z . If a surface is convex (like a mountain peak), it will have positive curvature. If a surface is concave (like a through or a valley bottom), it will have negative curvature.

(5) *The Topographic Position Index (TPI)* is a metric of slope position, based on Weiss's algorithem (Weiss, 2001) that corresponds to the difference of the elevation of a central pixel with the average of that of neighbouring pixels (3 x 3 pixels), where TPI equals zero/near-zero means flat or a near continuous slope and positive TPI means the central pixel is much higher than the surrounding areas, ridge or hill, and negative TPI represent the central pixel is much lower than the surrounding areas, bottom of a valley or gully. The capability of the topographic position index (TPI) to predict snow distribution has been observed in alpine environmen (Revuelto et al., 2014)

Topographic position is a scale-dependent phenomenon (Weiss, 2001). In order to accurately represent landforms at a coarse scale, such as stream channels ranging from tens to hundreds of meters, this study introduces two additional indices: *TPI_9* and *TPI_27*. *TPI_9* is calculated in 9 x 9 pixel windows, while *TPI_27* uses a window size of 27 x 27 pixels. The differences in scale can be seen in Figure 3.2, which illustrates typical mountainous terrain of Norway.

The *vegetation parameters* are from by ICESat-2 ATL08 product as describe in Section 3.2.1, including (6) *h_mean_canopy* and (7) *canopy_openness* that are computed by photons distribution of the canopy within a the segmet (100 m). And (8) *segment_cover* is the woody vegetation fractional from third source (Buchhorn et al., 2020). The ICESat-2 is unable to provide precise canopy parameters when operating under snowy conditions, thereby necessitating the use of supplementary corrections or third-party vegetation databases. A more detailed analysis of this matter can be found in Section

3.2. Data Preparation

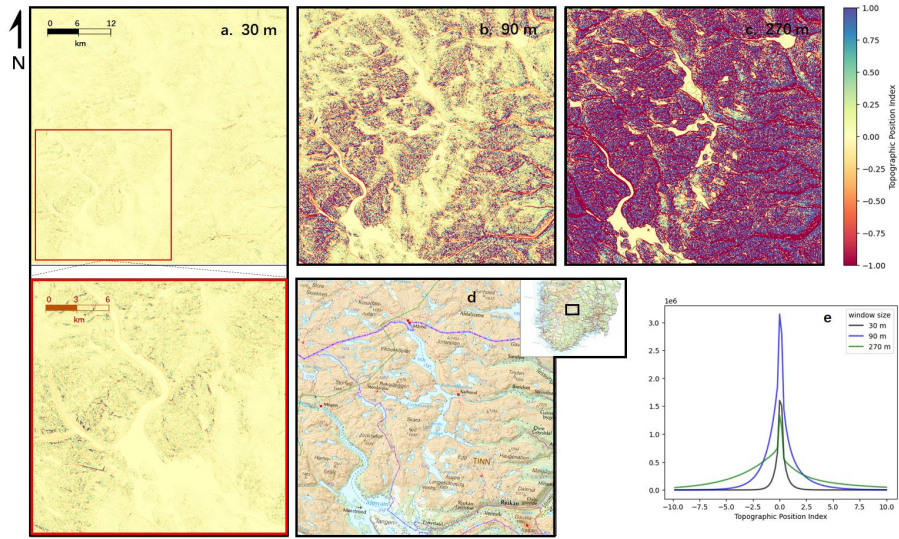


Figure 3.2.: The Topography Index: Scale-dependent Effects. Window size in 30 m (a); window size in 90 m (b) ; window size in 270 m (c), the map of east Hardangervidda, southern Norway (d); the distribution of TPI in different scales (e).

5.2.3.

3.2.4. EAR5 Land: snow and wind parameters

ERA5 Land (version 5) is a climate reanalysis that has been gridded to a regular lat-lon grid of $0.1^\circ \times 0.1^\circ$ (native resolution 9 km). The snow depth data provided by ERA5 Land represents an instantaneous grid-box average of the snow thickness on the ground, excluding snow on the canopy (Muñoz Sabater, 2021a).

The snow depth from EAR5-Land are coupled with snow depth derived from ICESat-2 ATL08 at daily resolution. To further enhance the characterization of the grid during downscaling, ERA5 Land monthly dataset contributes additional features such as snow melt, snowfall, and wind, which are calculated accumulatively for the water year period (September to September):

- (9) *snow fall accumulation* is a proxy of snow precipitation at montly resolution.
- (10) *Snow melt accumulation* is a proxy of melting energy at montly resolution.

These calculations aid in characterizing the grid from both a snow accumulation domain and a snow melting domain, which in turn helps with statistical downscaling.

- (11) *Wind-aspect factor (W_f)* (Bennett et al., 2022; DVORNIKOV, 2015) is a proxy for snow accumulation on the lee side of topographic obstacles. It is with positive value to the leeward but negative

3. Methodologies

value to windward of the topographical features. Bennett et al. (2022) classified the prevailing wind direction into eight cardinal directions by $\pm 22.5^\circ$ increments, i.e., N, NE, E, SE, S, SW, W, and NW, and applied eight different equations to get the factor ranging from -1 to 1 or -1.414 to 1.414. In essence, the wind-aspect relationship can be described by a cosin function ranges from -1 to 1 for any prevailing direction {Figure 3.3}:

$$W_f = -\cos(aspect - dir_{wind}) \quad (3.7)$$

Where dir_{wind} is defined by the direction of the wind origin, i.e, northerly wind blows from the north to the south and referred to as 0° .

As the scouring and loading effect may not cancel each other, so the W_f are further split to the leeside factor ($W_{uf_{positive}}$) and the windward factor ($W_{uf_{negative}}$), and times the wind speed in power of 3 (Figure 3.3) to get accumulative effect of wind over the winter period.

$$W_{uf_{positive}} = \sum W_{f_{positive}} u_{wind}^3 \quad (3.8)$$

$$W_{uf_{negative}} = \sum W_{f_{negative}} u_{wind}^3 \quad (3.9)$$

Where the u_{wind} is the monthly average wind speed at 10 m from ERA5. And the equation express the potential accumulative effect over the time period. In this study, this study account the snow season in monthly temporal resolution, starting at September when the value starts accumulate from 0, and ending at September when the value reaches the maximum. During the annual cycle, when the monthly snow depth is below 0.1 m, this value does not accumulate as the snow blowing is not available.

3.3. Gradient Descent Co-registration

DEM often suffer from misalignment, which poses a challenge for accurate change detection and analysis (Paul et al., 2015). While the commonly used NuthKaab coregistration (Nuth & Kääb, 2011) efficiently handles georeferencing errors on the pixel and sub-pixel levels, it is limited in handling the rotations, the different resolutions and the computationally-intensive tasks, which is particularly time-consuming for large datasets and global applications.

This study presents a robust gradient descent-based coregistration (GDC) approach that *treats digital elevation model (DEM) co-registration as a bound-restricted minimizing problem with random noise*.

3.3. Gradient Descent Co-registration

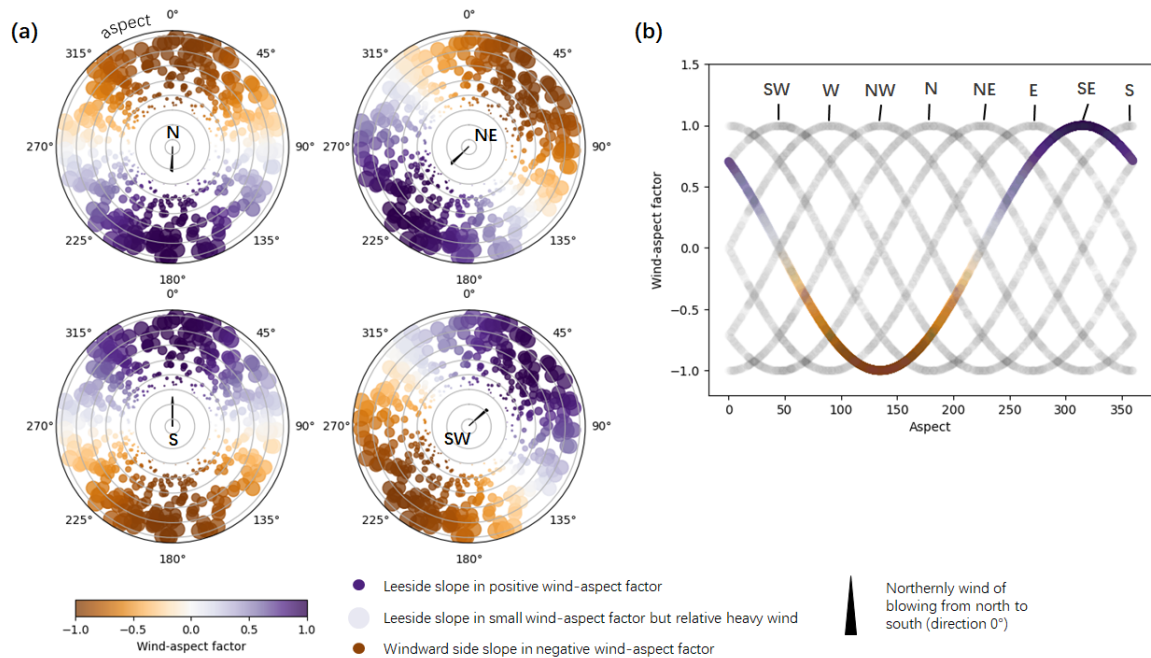


Figure 3.3.: Quantifying the Relationship between Wind and Aspect in Snow Redistribution. The prevailing wind, e.g. from N, NE, S, SW result in negative value on windward side and positive values on leeside (a). And the relationship are decribed by a cousin function (b).

3. Methodologies

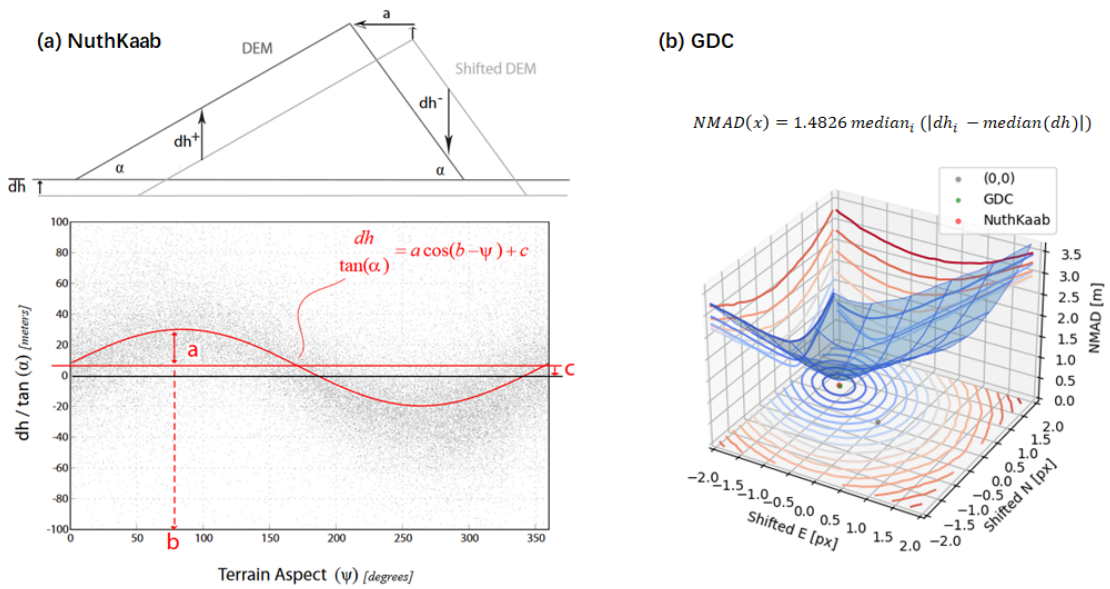


Figure 3.4.: Coregistration Techniques: NuthKaab vs. Gradient Descent. A 2D scheme of elevation difference (dh) induced by a DEM shift in a curve line. It suggests a statistical solution (a) where the dispersion is related to aspect (ψ), slope (α), shifted distance (a), shifted direction (b) and vertical bias (c). By solving the equation, it gives a vector (a, b, c) to shift the DEM back over iterations (Nuth & Käab, 2011). On the other hand, GDC presents dh in a curved surface, it aims finding the shift matrix using gradient descent algorithm, resulted in the local minimal of NMAD (b)

3.4. XGBoost Regression Model

GDC performs co-registration iteratively and efficiently by finding the shift matrix with lower computing consumption without calculating terrain parameters while supporting datasets in different resolutions. Specifically, it aims to minimize the robust Normalized Median Absolute Deviation (NMAD) using the gradient descent algorithm:

$$\min_x f(x) = \min_x \mathbb{E}[F(x, \xi)] \quad (3.10)$$

Here, x represents the value of x that minimizes the function $f(x)$. The function $f(x)$ is defined as the expected value of the function $F(x, \xi)$, where ξ is a random variable that represents uncertainty in the problem.

The goal of the minimization problem is to find the value of x that minimizes the expected value of $F(x, \xi)$, which represents the optimal decision under uncertainty. In the context of DEM coregistration. The function to be minimized is the NMAD. The primary source of noise is from DEMs. And the optimization technique employed in this study is gradient descent algorithm. At each step, GDC gains at a learning rate and ceases when it meets a specified criterion. If there is no optimization techniques, GDC could be regarded as same as an seldom used ‘grid search algorithem’ (Section 2.2.3 discussed other algorithem).

This study aligned DEMs with ICESat-2 snow-free segments tile by tile. The aligned DEM tiles exhibit the minimal NMAD compared to reference ICESat-2 snow-free segments. Although the remaining median error is typically considered a vertical bias, this study did not apply vertical bias correction during co-registration. The rationale for this decision was that the DEMs were not entirely free of snow cover, which could have shifted the median error. Furthermore, in some tiles, the sample size of points was not sufficient to achieve an accurate vertical bias correction. The implementation of the GDC method is available in a Python repository called xDEM (Xdem contributors, 2021).

3.4. XGBoost Regression Model

3.4.1. Bias correction

In this study, XGBoost, a supervised regression model (Section 2.3), was utilized for bias correction and statistical downscaling. Specifically, the model was applied to correct for specific system errors that arise from the digital elevation model (DEM) and ICESat-2 data after coregistration:

$$\sigma_{dh} = \sqrt{\sigma_{dem}^2 + \sigma_{ICESat_2}^2} \quad (3.11)$$

Previous research has highlighted the importance of accurate and precise ICESat-2 elevations and

3. Methodologies

snow-free reference elevations for generating reliable snow depth estimates through elevation differencing (Enderlin et al., 2022). To address discrepancies between these datasets and obtain unbiased results, a two-dimensional bias correction approach was proposed in previous studies (Section 2.5.1). However, the errors, or the inconsistency of the DEM and ICESat-2 can vary across multiple dimensions. Therefore, this study accounts for these errors by employing an XGBoost regression model to predict the error using various features such as terrain parameters, vegetation, and quality metrics from ICESat-2 (see Table 3.1). These features were chosen based on their potential influence on elevation measurements and were obtained from multiple data sources (see Sections 3.2.1 and 3.2.3). And the features are expected to be able to explain the bias in both conditions.

It should be noted that XGBoost regression model requires enough training dataset to predict robust statistical bias correction. XGBoost provides a built-in feature importance metric that can be used to identify the most important features. This information can be used to guide feature engineering. The model tuning and cross-validation will be elaborated upon in Section 3.4.3.

Table 3.1.: Features in the Bias Correction Regressor

| Data source | Features | Descriptions |
|----------------|------------------|---|
| ICESat-2 ATL08 | E | the east grid coordinates |
| | N | the north grid coordinates |
| | h_te_best_fit | the elevation in snow-off condition (m) |
| DTM10 | slope | slope angle (degree) |
| | aspect | slope aspect (degree) |
| | curvature | curvature (m^{-1}), scalar value without direction |
| | planc | curvature (m^{-1}) in a direction of the steepest slope |
| | profcc | curvature (m^{-1}) in a direction perpendicular to the steepest slope |
| | TPI | topographic position index in 3 pixels (30m window size) |
| | TPI_9 | topographic position index in 9 pixels (90m window size) |
| | TPI_27 | topographic position index in 27 pixels (270m window size) |
| ICESat-2 ATL08 | h_te_std | quality metrics, see Section 3.2.1 |
| | h_te_skew | |
| | h_te_uncertainty | |
| | subset_te_flag | |
| | segment_cover | vegetation parameters, see Section 3.2.1 |
| | h_mean_canopy | |

| Data source | Features | Descriptions |
|-------------|------------------|--------------|
| | canopy_openness | |

3.4.2. Statistical downscaling

Statistical downscaling is to bridge the coarse resolution products to fine resolution by establishing an empirical link between a set of predictors X and predictands y by a statistical model (F) (eq. 2.6). It is based on several assumptions (Maraun & Widmann, 2018):

- Predictor have to be realistically and bias free in present climate.
- Informative predictors need to be selected that explain a large fraction of local variability on all timescales of interest. That is so called the stationary assumption.

In this study, the predictand y represents the difference between ICESat-2 derived snow depth and mean snow depth from ERA5 Land at the same location and time. The predictor variables X , or features, are selected based on data availability, as well as factors related to snow melting and redistribution processes. Specifically, the downscaling includes detrending, regression, and retrending in three steps.

(a) Detrend

$$y = \text{Snowdepth}_{ICESat_2} - \text{Snowdepth}_{ERA5} = F(X)$$

Detrended snow depth y is the deviation from mean snow depth, representing the local variability of the snow depth. The subtracted snow depth is the mean value interpolated from ERA5 Land.

Before training the model, quality control measures are implemented to ensure reliable results. Specifically, measurements $\text{Snowdepth}_{ICESat_2}$ with negative values are excluded as they are considered pure noise. Additionally, mean snow depth Snowdepth_{ERA5} less than 0.1 m are excluded as these values indicate that the snow depth is close to zero and therefore meaningless for downscaling purposes.

(b) Regression

As a consequence of snow redistribution, exposed mountain crests and steep slopes are often nearly snow free in the accumulation season. In the opposite, wind-sheltered areas, surface depressions, bases of steep slopes or cliffs, and glaciers receive large amounts of snow. So multiple terrain parameters, slope, aspect, curvature (normal curvature, profile curvature and horizontal curvature), TPI (in 30 m, 90 m, 270 m scales) are inputted as predictors. Vegetation is an important factor for snow distribution, here we get canopy openness, vegetation height, and canopy density from ICESat-2.

3. Methodologies

The wind-aspect factors used in this study are the leeside factor ($W_{uf_{positive}}$) and the windward factor ($W_{uf_{negative}}$), which were accumulated during the snow season (Section 3.2.4). Snow melt accumulation from ERA5 Land monthly was used to determine the scale of snow melt for each grid, while snowfall as well (Section 3.2.4). It should be noted that these variables do not work on a pixel level (10 m), but rather characterize wind redistribution and snow dynamic patterns at the grid level (9 km), which were then downsampled.

Table 3.2.: Features in the Downscaling Regressor

| Data source | Features | Resolution | Descriptions |
|-------------------|-----------------|------------|--|
| ICESat-2 ATL08 | E | - | the east grid coordinates |
| | N | - | the north grid coordinates |
| | h_te_best_fit | - | The surface elevation of middle point of segment (m) |
| DTM10 | slope | 10 m | slope angle (degree) |
| | aspect | 10 m | slope aspect (degree) |
| | curvature | 10 m | |
| | plancl | 10 m | |
| | profcl | 10 m | |
| | TPI | 10 m | |
| | TPI_9 | 10 m | |
| | TPI_27 | 10 m | |
| ICESat-2 ATL08 | segment_cover | 100 m | vegetation parameters, see Section 3.2.1 |
| | h_mean_canopy | 100 m | |
| | canopy_openness | 100 m | |
| ERA5 Land | sfall_acc | 9 km | snow fall accumulation, see Section 3.2.4 |
| | smelt_acc | 9 km | snow melt accumulation, see Section 3.2.4 |
| | wf_negative | 9 km | wind-aspect factor accumulation, see Section 3.2.4 |
| | wf_positive | 9 km | |

(c) Retrend

The last step is to reproduce snow depth at local scale by adding the predicted y with mean snow depth from ERA5 Land. It is important that the assumption, the difference in snow depth measurements between ICESat-2 and ERA5-land, is stable over time. If the difference varies over time, then

the model may not be accurate for all time periods, which could lead to inaccurate snow depth estimates.

3.4.3. Hyperparameters and cross-validation

XGBoost has many hyperparameters that can significantly impact its performance, including the objective function, number of trees, learning rate, and regularization terms. It is important to tune these parameters carefully, and using a validation set to avoid overfitting.

By default, XGBoost uses the `reg:squarederror` objective function, which aims to minimize the mean squared error (MSE) between the predicted and actual values. This objective function is generally suitable for most regression tasks. On the other hand, `reg:absoluteerror` is another objective function that minimizes the mean absolute error (MAE) between the predicted and actual values. MAE is more robust to outliers than MSE. For this reason, this study has opted to use `reg:absoluteerror` in the context of DEM error and snow depth. Furthermore, there are several hyperparameters that can be tuned to improve the performance of XGBoost:

- `n_estimators` (default 100) – This parameter determines the number of trees in the ensemble. Increasing this value results in more weak learners contributing towards the final output but can significantly slow down training time.
- `max_depth` (default 6) – This parameter controls the complexity of the algorithm. A lower value decreases the algorithm's ability to detect patterns (underfitting), while a higher value risks overfitting by making the model too complex.
- `min_child_weight` (default 1) – Overfitting can be prevented by limiting tree depth, which is achieved with this parameter. A higher value reduces chances of overfitting on training data.
- `learning_rate/ eta` (default 0.3) – The rate at which the model learns is inversely proportional to its accuracy. Lowering this parameter improves a model's ability to detect patterns but requires longer training time. Setting it too low may hinder convergence.
- `gamma/ min_split_loss` (default 0) – This regularization parameter influences how strongly regularization should be applied, with higher values reducing chances of overfitting but increasing risk of underfitting if set too high.
- `colsample_bytree` (default 1.0) – This parameter determines what fraction of features/predictors should be used in each tree during training. As different trees may use different features, overfitting can be reduced and training speed improved. The value ranges from 0 to 1.
- `subsample` (default 1.0) – Similar to `colsample_bytree`, this parameter determines what fraction of instances should be used in each tree during training. It also reduces overfitting and improves training time.

Note that these hyperparameters may need to be adjusted according to the dataset being used. One of

3. Methodologies

way to do that is through grid search. The optimal parameters for the regression task in this study have been identified as below. After identifying the optimal hyperparameters for our regression task, this study takes measures to prevent overfitting by dividing the dataset into training and testing subsets, and applying cross-validation techniques as demonstrated in Figure 3.5.

Listing 3.1: The Optimal Hyperparameters by Grid Search.

```
1  params = {  
2      'objective': 'reg:absoluteerror',  
3      'max_depth': 10,  
4      'learning_rate': 0.1,  
5      'n_estimators': 250,  
6      'min_child_weight': 1,  
7      'subsample': 0.7,  
8      'colsample_bytree': 1,  
9      'gamma': 0.1,  
10     }
```

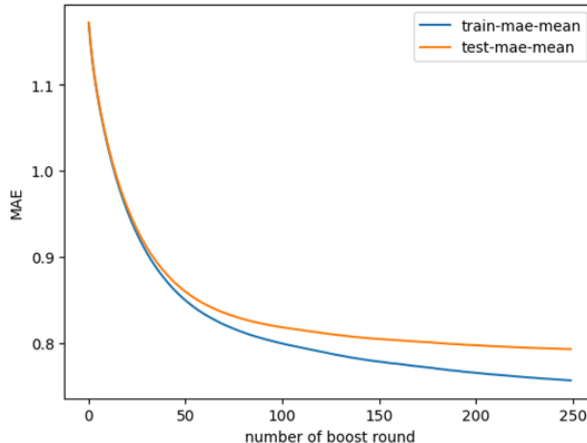


Figure 3.5.: Preventing Overfitting with Cross-validation in XGBoost. In this example, as the number of boosting rounds increases, the training and testing MAE decrease and eventually converge to a stable value (0.793 and 0.756 respectively). It indicates that the model is not overfitting, and n_estimators is reasonable at value of 250.

3.5. Evaluation of Snow Depth

3.5.1. ICESat-2 derived snow depth vs lidar derived snow depth

The purpose of the validation data is to investigate various factors that impact the accuracy and precision of ICESat-2 derived snow depth. These include the resolution and quality of the reference DEM, correctness of bias correction, and fitness of ICESat-2 derived snow depth. To evaluate differences in

3.5. Evaluation of Snow Depth

snow depth, the framework for DEM uncertainties discussed in Section 2.2.2 and 5.2.3 can be applied. Accuracy is quantified using mean, median, while precision (random error) is quantified using NMAD. The fitness of the ICESat-2 derived snow depth to validation data is determined by R-square value.

First of all, elevation differencing can also be used to generate a validation dataset. For example, one such dataset was collected in Hardangervidda, Southern Norway (Figure 3.6, 4.2), where airborne lidar captured snow cover surface while the reference DEM was obtained from a snow-free condition. However, during validation, certain factors such as the date on which snow depth was collected and any possible bias in the reference DEM should be considered. Additionally, it is important to note that since validation datasets only cover a small area, they only account for performance under specific conditions. Further analysis is necessary to determine the impact of slopes, vegetation, and other terrain parameters.



Figure 3.6.: Snow Survey via Drone Lidar in Hardangervidda, Southern Norway. The field trip took place on March 11, 2022, a week later after ICESat-2 flying over the same location. Photo: Eivind Torgersen, UiO

3.5.2. ICESat-2 derived snow depth vs ERA5 Land snow depth

The purpose of this comparison is to determine if there are any discrepancies in snow depth values between the two datasets. Specifically whether ERA5 Land overestimates snow depth, such phenomenon has been noted in previous studies (Orsolini et al., 2019). Additionally, this comparison help to identify differences of using different reference DEMs in snow retrieval. To achieve this, the two datasets were spatially and temporally coupled at daily resolution to get snow depth value from ERA5 Land. The snow depth was aggregated to mean value and visually compared to assess bias at a national scale. As this study does not expect a linear relationship between the two datasets, a

3. Methodologies

scatter plot with the Spearman correlation coefficient will be utilized. Additionally, a histogram will be employed to depict the distribution of the snow depth differences.

The evaluation of snow depth from different sources, at different scales, and with varying representations is a challenging task. ERA5 Land provides coverage for glaciers, lakes, and fjords in a 9 km resolution while ICESat-2-derived snow depth excludes all moving terrain and water areas where reference DEM is unavailable. These disparities in data sources must be taken into consideration when understanding the difference (further discussion in Section 5.3).

3.5.3. Downscaled snow depth vs lidar derived snow depth

The downscaling technique is a useful tool that can generate snow depth values at any specific location and time. However, this process introduces uncertainties due to the regression training dataset and initial condition (the ERA5 Land dataset). The evaluation of downscaled snow depth focuses on whether it can accurately represent the snow depth distribution on a hill-slope scale. If successful, it is vital to identify which features dominate the subgrid distribution most. In contrast, if it fails to do so, it is necessary to identify which conditions cannot be reproduced.

As a contemporary large-scale lidar-based snow depth data was not available for this study, an airborne survey conducted by NVE in Southern Hardangervidda in April 2008 and 2009 will be used for validation purposes instead. It is crucial to acknowledge that the training data for regression were based on observations from the previous four years (2018-2022). Furthermore, predictor features such as terrain, vegetation, and climate conditions may have undergone changes since 2008.

This study produced two types of downscaled snow depth products: point-based and grid-based. The point-based product has the same resolution as the ATL08 product, with almost 20 million points for mainland Norway. On the other hand, the grid-based snow depth product was generated based on DEM resolution; hence no vegetation parameter from ICESat-2 was included as input features.

4. Study Case - mainland Norway

4.1. The Physical Geographical Setting

Norway is located on the western side of the Scandinavian Peninsula in northwestern Europe, situated between latitudes 57° 58' N and 71° 11' N and longitudes 4° 40' E and 30° 58' E. The country's heterogeneous climate is influenced by its diverse topography, ranging from lowland valleys to high mountains. This section provides an overview of Norway's climate characteristics, including patterns of snow distribution, precipitation, wind, and temperature fluctuations.

Snow distribution and variability are primarily influenced by moisture and temperature and vary based on altitude and latitude. The North Atlantic Current, or Gulf stream, moderates the range of temperatures throughout the year, particularly along the coastal areas of Norway (Kaspi & Schneider, 2011; Keil et al., 2020). During winter, the air temperature is usually lower than the water temperature of the current, resulting in higher evaporation rates (*The Physical Geography of Fennoscandia*, 2005). Moist air masses are carried with the westerly winds, leading to heavy precipitation averaging from 1000 to 3000 mm per year in coastal areas when moist air is uplifted by the mountains. Conversely, inland regions experience drier and colder conditions due to the continental climate, such as Dovrefjell (Fokstugu: 435 mm) (Ketzler et al., 2021).

This gradient of climate from the western coast to the eastern inland is reflected in the equilibrium line altitude or snowline. The range of ELA or snowline is approximately between 1000 m to 2000 m with increasing distance from moisture (Etzelmüller et al., 2003). This results in Jostedalsbre Glacier in southwestern Norway, the largest glacier in mainland Europe, covering an area of approximately 487 square kilometers. The North Norwegian coast also witnesses remarkable snow accumulation with an extended duration of snow extent. Here, Glacier Svartisen is the second-largest glacier in Norway. Furthermore, snow accumulation varies from year to year; for instance, winter 2020-2021 experienced significant low snow conditions compared to recent years (Figure 4.1 a,b,c,d).

Coastal regions are exposed to strong winds due to differences in temperature between land and sea. Mountains act as barriers deflecting wind and creates calmer conditions inland. Among these mountains, Hardangervidda is the largest mountain plateau in Europe, with an average elevation of over 1,100 meters. The relatively flat terrain on top of the plateau makes it prone to high winds with intense snow conditions. Finnmark Plateau, located in the northernmost part of Norway, is also known for

4. Study Case - mainland Norway

its strong winds, particularly in the winter with extreme cold temperatures (Ketzler et al., 2021) (Figure 4.1).

In summary, the heavy precipitation and relatively low temperatures at high altitudes result in considerable snow accumulation at elevated locations. This accumulation feeds glaciers, acts as natural reservoirs, and shapes the landscape over extended periods. It is crucial to understand Norway's snow patterns and their variability for effective management of natural resources, adaptation to climate change, and mitigation of associated risks.

4.2. The Data Setting

From 2018 Oct 14 to 2022 Oct 12, there are 3968 granules of ATL08 products covered the mainland Norway. And the measurements on land surface have 14918709 segments after droping NaN, where 4,959,085 snow-free segments are on land, excluding moving terrain (permenent ice and inland water), and 9,213,030 segements are with snow-cover over land and inland water area (Figure 4.2).

Airborne lidar data was collected for a 240 km² area on Hardangervidda mountain plateau using a Leica ALS50-II instrument. The data was collected during two different time periods in 3-21 Arpil 2008 and 21-24 April 2009 to determine the overall snow condition. Each time, six flight-lines of lidar data were collected, with each flight-line being 80 km long, following a west-east orientation and having a scanning width of approximately 1000 m. The snow depth is calculated on 2m resolution bare ground DEM (some small perennial snowpatches still exist) (Melvold & Skaugen, 2013)

A near real-time snow survey was conducted using DJI Zenmuse L1 in Hardangervidda on March 11, 2022, one week after ICESat-2 flew over the same location. The survey covered only a strip of land measuring 3,700 meters in length and 700 meters in width with relatively flat terrain, sparse vegetation. Snow depth measurements were obtained based on DTM1 as the reference.

To cover the entire mainland of Norway and to use as reference DEMs, four Digital Elevation Models (DEMs) were used, namely DTM1, DTM10, Copernicus GLO-30 (GLO30), and FABDEM (FAB) [Hawker et al. (2022); Agency (2021); ©Kartverket]. DTM1 was divided into approximately 15 x 15 km tiles while DTM10 and COP30 were divided into approximately 50 x 50 km tiles. FABDEM was divided into 1° x 1° tiles. All DEMs were transformed to WGS 84 - UTM33N projection (EPSG:32633) and vertical datum EGM2008 (EPSG:3855).

4.3. DEM Coregistration

The gradient-descent-based coregistration algorithm is utilized to rectify the horizontal misalignment of DEMs and achieve a minimized NMAD of samples. Specificaly, it is the minimal NMAD of the el-

4.3. DEM Coregistration

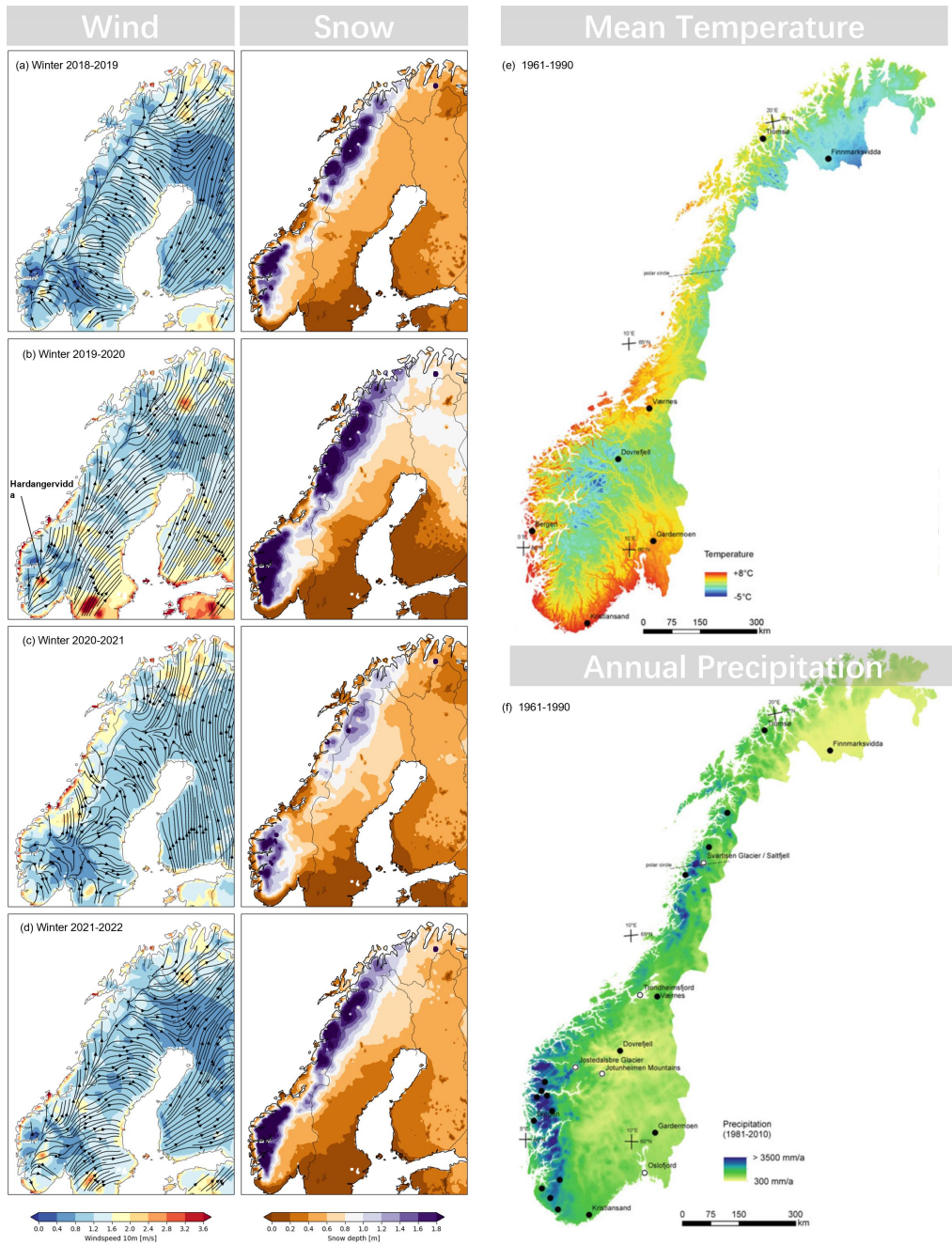


Figure 4.1.: The Climate of Norway. The wind patterns and snow distribution during winter from 2018 to 2022 on the Scandinavian Peninsula(a, b, c, d). Average air temperature for the period of 1961–1990 (e) . Precipitation on the basis of station data and geostatistical modelling for the period of 1961–1990 (f) Notably, the 10 most intensive precipitation events from 1950 to 2008 are marked with black dot in western coastal foreland. Figure e and f from Ketzler et al. (2021). Data source: Lussana (2018); Muñoz Sabater (2021b).

4. Study Case - mainland Norway

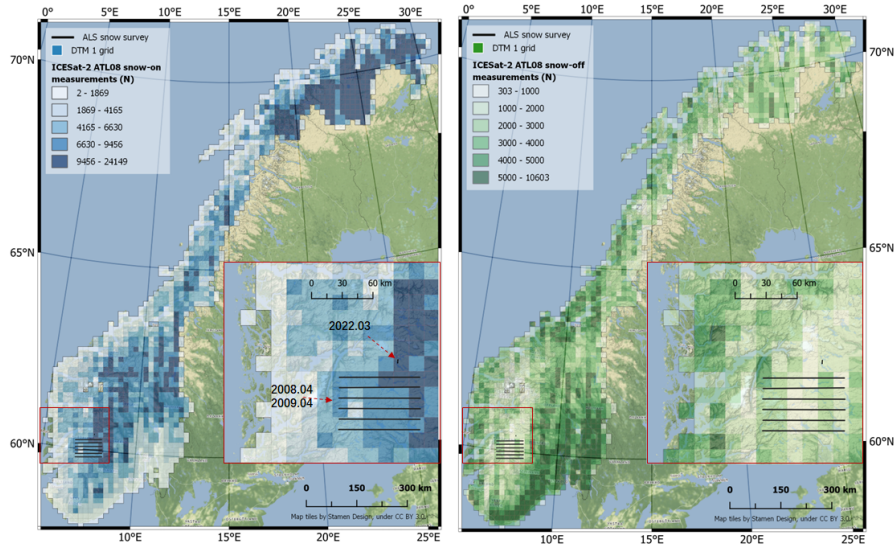


Figure 4.2.: The ICESat-2 Segments and Snow Surveys. The ICESat-2 Segments, which are presented separately in DTM1 tiles, include snow-on segments in blue and snow-free segments in green. The validation dataset from NVE’s ALS snow survey conducted in 2008.04 and 2009.04 in Hardangervidda, Southern Norway, as well as the field trip conducted in 2022.03 by this study, were used for validation purposes. NVE data source: Melvold & Skaugen (2019)

elevation difference between values from DEM and values from ICESat-2 snow free segments. Table 4.1 presents the results of DEM coregistration. The NMAD shows a 2% improvement for DTM1, while DTM10, GLO30, and FAB exhibit an improvement of 22%, 21%, and 35%, respectively. Subsequently, after coregistration, the percentage of points with a deviation less than 0.5 m from ICESat-2 snow-free segments is calculated to be 48.9%, 49.13%, 23.7%, and 27.2% for DTM1, DTM10, GLO30, and FAB, respectively. However, it should be noted that the minimal NMAD of samples may not always guarantee the best coregistration if there is potential noise interference in samples (see Section 5.1.1 for further discussion). To diminish the effect of noise, this study employed different weightings on elevation differences through *subset_te_flag*, which is a quality metric derived from ICESat-2. Nevertheless, despite adjusting the weights, final statistics, such as NMAD, were calculated evenly to represent the performance of coregistration.

Table 4.1.: The Improvement of DEM by Coregistration

| Metrics | Co-registration | DTM10 | DTM1 | GLO30 | FAB |
|-----------|-----------------|-----------|-----------|-----------|-----------|
| N | - | 5,443,945 | 5,443,945 | 5,443,945 | 5,443,945 |
| <0.5m (%) | before | 41.839 | 48.729 | 18.108 | 18.985 |

4.3. DEM Coregistration

| Metrics | Co-registration | DTM10 | DTM1 | GLO30 | FAB |
|-----------|-----------------|--------|--------|--------|--------|
| <0.5m (%) | after | 48.923 | 49.130 | 23.720 | 27.295 |
| <1.0m (%) | before | 59.785 | 65.441 | 31.078 | 34.002 |
| <1.0m (%) | after | 65.628 | 65.679 | 37.965 | 45.782 |
| NMAD (m) | before | 0.992 | 0.774 | 2.533 | 2.381 |
| NMAD (m) | after | 0.772 | 0.760 | 2.058 | 1.611 |

Table 4.2.: The Improvement of DEM by Coregistration (*subset_te_flag* equals 5)

| Metrics | Co-registration | DTM10 | DTM1 | GLO30 | FAB |
|-----------|-----------------|-----------|-----------|-----------|-----------|
| N | - | 3,609,933 | 3,609,933 | 3,609,933 | 3,609,933 |
| <0.5m (%) | before | 51.630 | 60.137 | 23.121 | 22.875 |
| <0.5m (%) | after | 60.688 | 60.712 | 31.608 | 33.931 |
| <1.0m (%) | before | 71.633 | 78.419 | 38.780 | 40.130 |
| <1.0m (%) | after | 78.858 | 78.753 | 49.150 | 55.365 |
| NMAD (m) | before | 0.682 | 0.511 | 2.007 | 1.961 |
| NMAD (m) | after | 0.507 | 0.498 | 1.450 | 1.228 |

Figure 4.3 depicts the shift pixels in which all four DEMs indicate a misalignment towards the west and north directions. The analysis shows that most DTM10 tiles experienced an improvement through a ‘half’ pixel (5 to 10 m) shift, as did GLO30 and FAB. However, when DEM resolution comes to 1 m, the misalignment of one to three pixels (1 to 3 m) may not be significant relative to the native accuracy of DEM (Figure 4.4 a and A.2 a).

Moreover, approximately 67% of the ICESat-2 segments have *te_subset_flg* equals to 5, indicating superior match with DEMs (Table 4.2). This demonstrates the exceptional accuracy can potentially be achieved, with NMAD values as good as 0.51 m and 0.50 m for DTM1 and DTM10, 1.5 m and 1.3 m for GLO30 and FAB respectively, which are better than previous studies cases (W. Chen et al., 2022; Deschamps-Berger et al., 2022; H. Li et al., 2022). On the other hand, it also indicates uncertainties in ICESat-2 ATL08 under inferior observation conditions (more discussion in Section 5.2.1).

Overall, these findings emphasize the significance of accurate coregistration for DEMs, and highlight the potential for enhancing accuracy by utilizing quality metrics of ICESat-2 data. For residual errors, further analysis must be exercised.

4. Study Case - mainland Norway

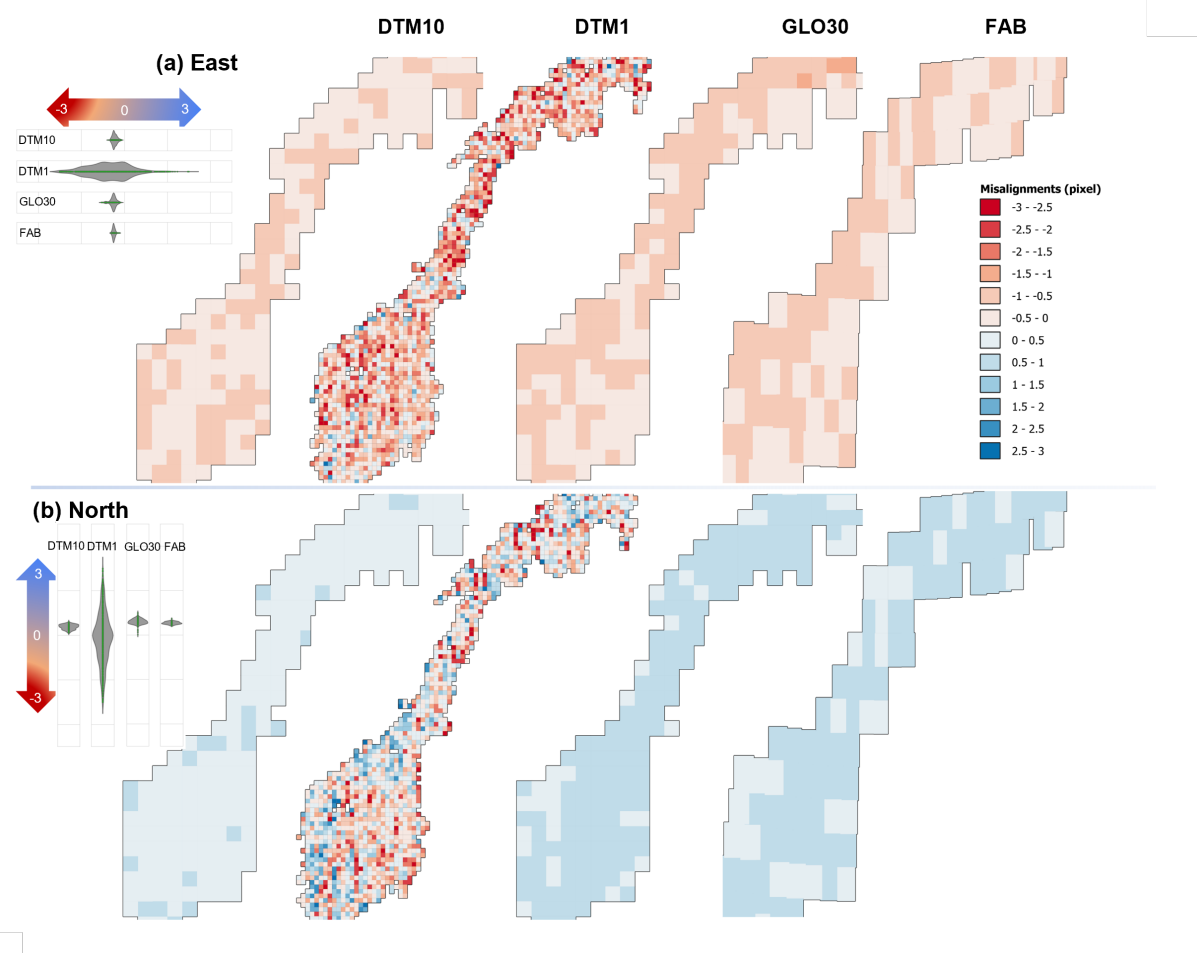


Figure 4.3.: The Misalignment of DEMs. The shift pixels in East (a) and North (b) direction ranges from -3 to 3, which can cause significant errors in the accuracy of the DEMs.

4.4. Bias Binning Analysis: DEM Comparison

Statistical binning is a visualization tool used to identify patterns and trends in data, which is useful for investigating residual errors between aligned DEM and ICESat-2 snow-free segments. Figure 4.4 illustrates an example of DTM10 in each steps, including raw, after co-registration, and correction. The residual errors are clustered into bins based on different attributes such as elevation, aspect, slope, curvature, and TPI. In Figure 4.4 a, the aspect-dependent error, or the fingerprint of misalignment, is depicted and removed through co-registration, where the median value (Q2) is located close to zero for all bins. However, the 25% quantile (Q1) and the 75% quartile (Q3) are skewed negative severely (i.e., $Q_3 - Q_1 < Q_2 - Q_1$).

Additionally, significant negative bias has been identified in slope categories (Figure 4.4 b) as there exists a nearly linear relationship between median and slope. Some studies have applied vertical bias correction based on slope [Enderlin et al. (2022)], slope and vegetation (Magruder et al., 2021), or laser incidence angles and vegetation (Tian & Shan, 2021). However, this study shows that the bias does exist over convex terrain but is not significant over concave terrain, indicated by TPI and curvature bins. Therefore, (1) this study applies XGBoost regression where terrain, vegetation, and ICESat-2 quality metrics are used, instead of just slope, to predict the residual errors; (2) Furthermore, the profile curvature behavior differently with curvature, plan curvature and TPI (Figure 4.5 e). This study is going to discuss the negative bias further from geomorphology perspective (Section 5.2.1).

Figure 4.5 quantifies the residual errors in terms of mean error and NMAD. Each grid represent 5% quantiles, ranging from the smallest value of attributes to the highest. For instance, prior to co-registration, DTM10 has aspect-dependent mean error (Figure 4.5 a), and a slope-dependent bias (Figure 4.5 b), and a negative bias over convex terrain (Figure 4.5 c). GLO30 exhibits a widespread negative bias due to vegetation (Figure 4.5 d). FAB has removed forest, instead, it has a positive bias over convex terrain, but a negative bias over concave terrain (Figure 4.5 f).

Aftyer the bias correction, the comparison between DTM1 and DTM10 indicates that they both achieved a high level of accuracy on low slope categories, with less than 1 m and 0.5 m NMAD in 65% and 35% of cases, respectively. However, the worst NMAD result was observed in the top 5% of slope quantiles and the least 5% of *n_photons* quantiles, which resulted in an NMAD of 2.4 m and 1.8 m, respectively. The bias correction applied to GLO30 produced better results than to FAB, with approximately 40% of measurements showing an NMAD of less than 1 m on the low slopes category. These improvements demonstrate the effectiveness of our approach in eliminating biases.

The overall distribution plot (Figure 4.6) show that all distributions exhibit a negative skewness with long tails on the left side. Prior to bias correction, Copernicus GLO30 had a median of -1.30 m, while FAB, which is a version of GLO30 with vegetation and building removed, exhibited less skewness. Although DTM1 and DTM10 had similar shapes, their 25% quantiles (Q1) suggested the presence of sys-

4. Study Case - mainland Norway

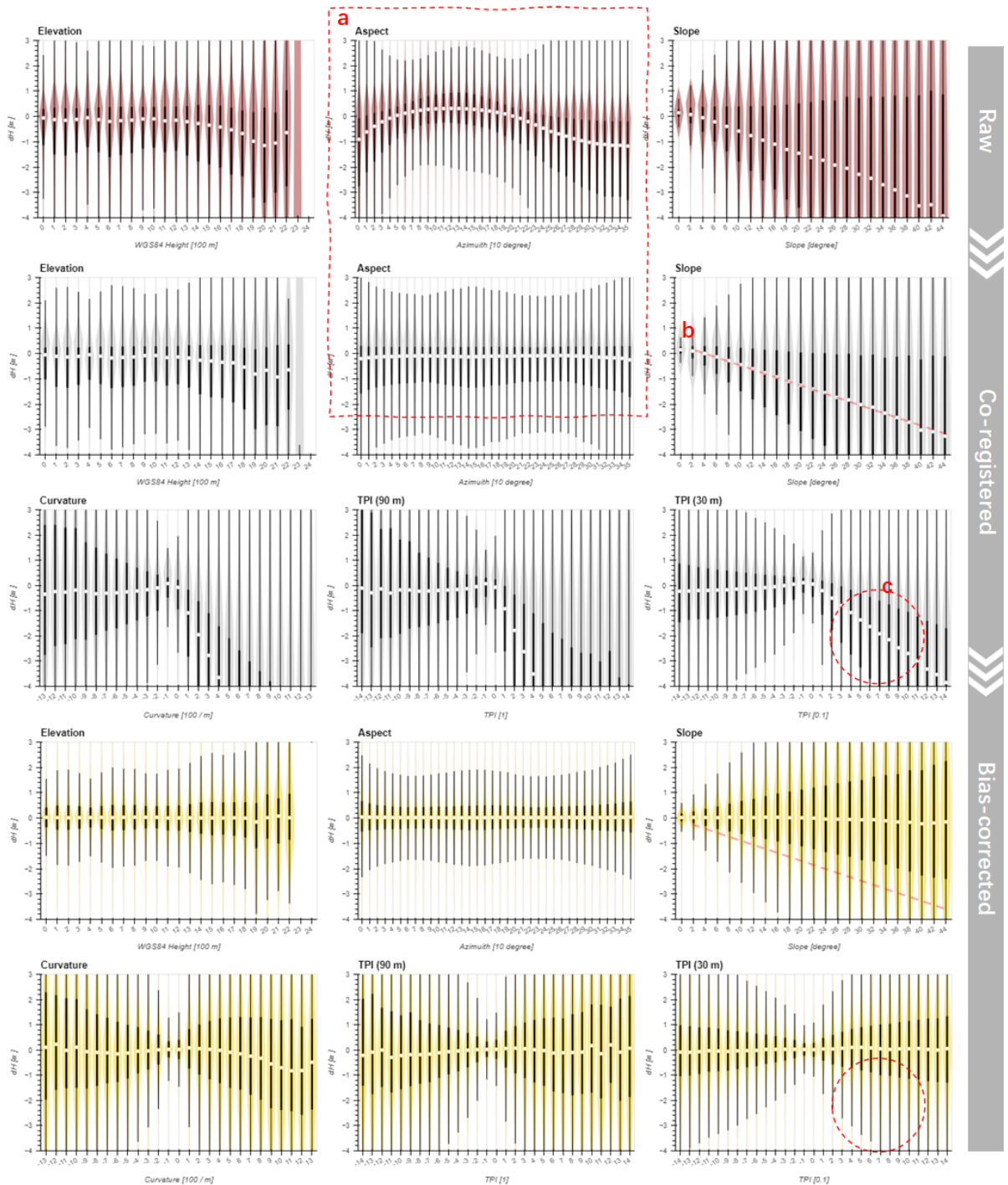


Figure 4.4.: Statistic binning Analysis of DEM Errors: Coregistration and Bias correction (ICESat-2 - DTM10). The dataset was divided into categories at three stages, and for each category, a violin plot displays the distribution of data. The median of each dataset is represented by a white dot at the center of the violin. The thick bar illustrates the 25% and 75% quantiles, respectively. If the violin is skewed to one side, it indicates a deviation from normal distribution. The aspect-dependent bias is identified and eliminated by co-registration (a); The negative bias are widespread after co-registration (a, b, c).

4.5. Features Importance and Regression Performance

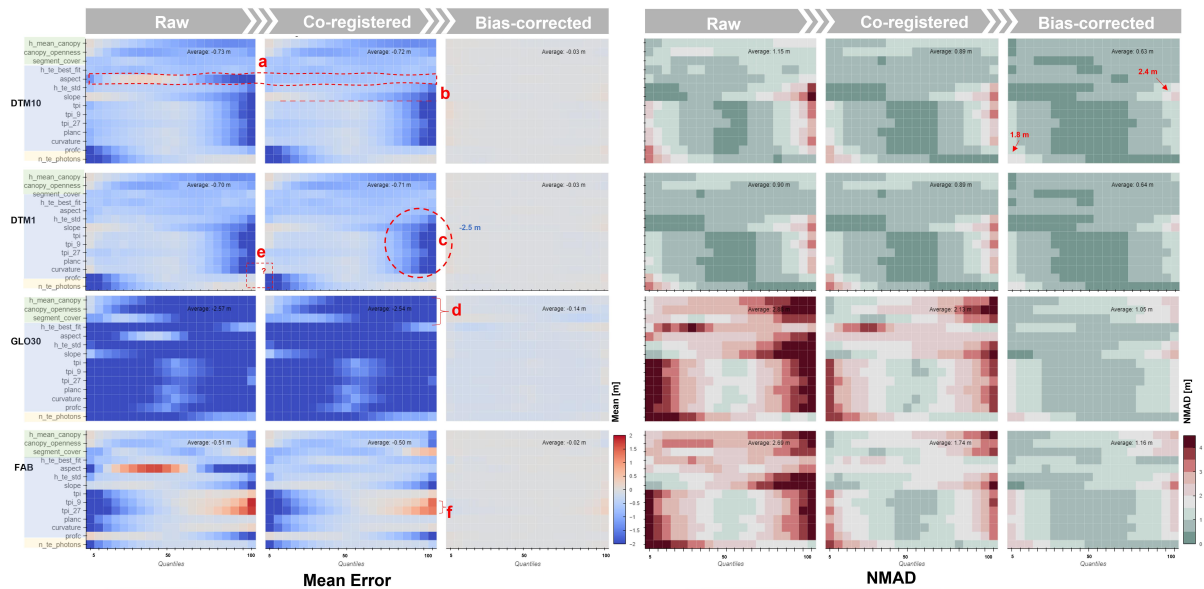


Figure 4.5.: The Mean Error and NMAD of Quantiles: Coregistration and Bias correction. Three vegetation features, ten terrain parameters and number of photons of ICESat-2 ATL08 segments are used to bin the residual errors. From left to right, each grid represent 5% measurements, and $N = 5,443,945$.

tematic biases.

After implementing the bias correction technique, there was a noticeable enhancement in the overall symmetry observed across all four scenarios. This was supported by the fact that Q1 moved nearer to the median, while Q3 remained relatively stable (with the exception of GLO30). Ultimately, there is an overall NMAD of 0.56 m and 0.57 m for DTM10 and DTM1, respectively. In contrast, GLO30 and FAB had higher NMAD scores of 0.98 m and 1.08 m. It is evident that bias correction led to a significant improvement in the accuracy of the results.

4.5. Features Importance and Regression Performance

After training the XGBoost model, the next step is to predict the bias correction and apply it to snow-on scenarios. The map in Figure 4.7 illustrates significant variations in predicted bias correction across different regions, depending on various factors such as slope, vegetation cover, and the number of photons. Negligible differences are observed between DTM10 and DTM1, with bias patterns being very similar to the slope at an aggregated scale. For instance, Hardangervidda and Finndmark are relatively flat areas with minimal bias on four DEMs. In contrast, GLO30 needs to be corrected heavily for vegetation removal in the eastern valleys, while FAB requires extra correction over vegetation area as well for unclear reasons. It is important to note that bias correction only corrects the DEMs

4. Study Case - mainland Norway

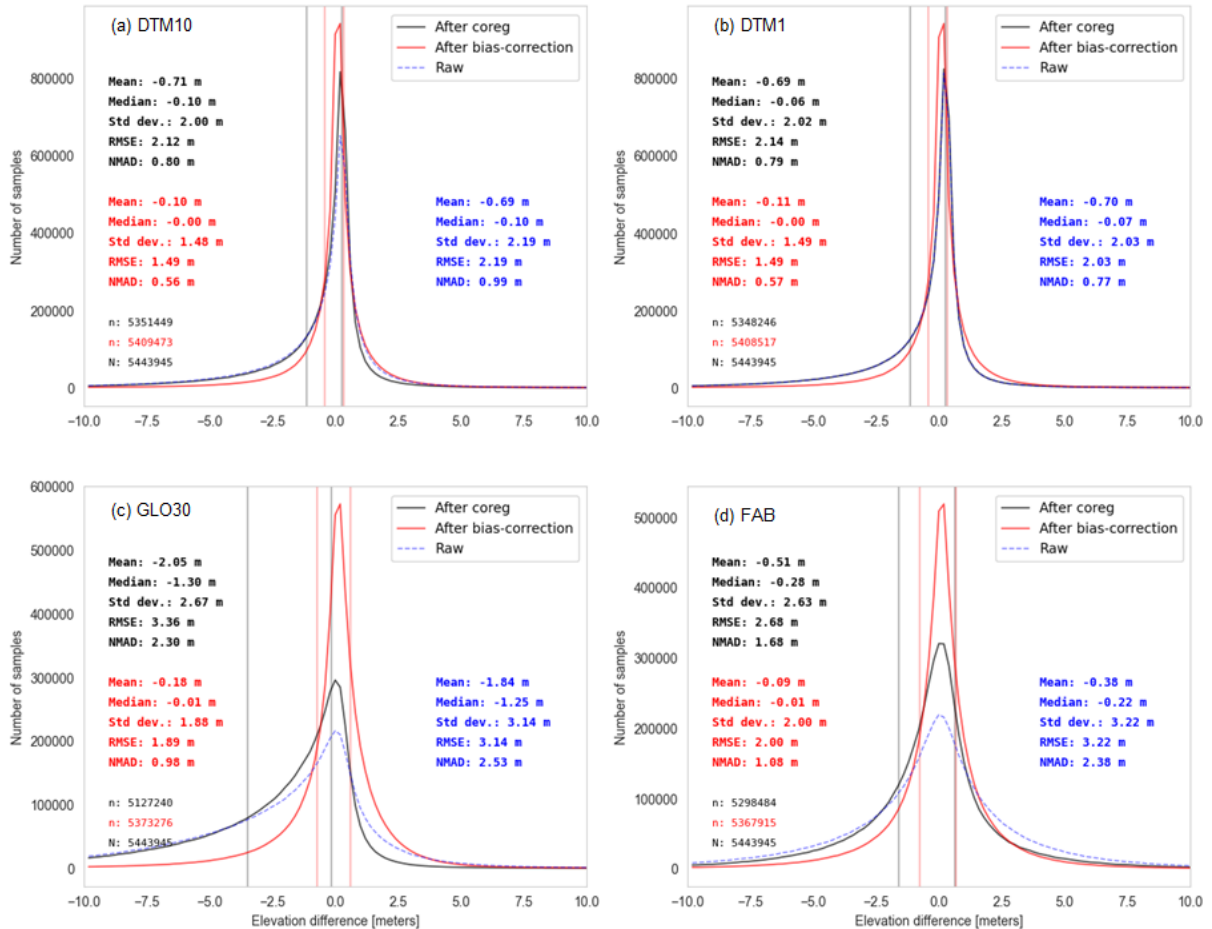


Figure 4.6.: The Overall Distribution of DEM errors. The statistical data for raw, after-coregistration, and bias-correction are represented by blue, black, and red colors respectively. The 25% quantile (Q1) and the 75% quantile (Q3) are displayed from left to right along the x-axis. Please note that a window of -10m to 10m was used to filter outliers in the metrics employed. And, the number of measurements is given by n and N (total).

4.5. Features Importance and Regression Performance

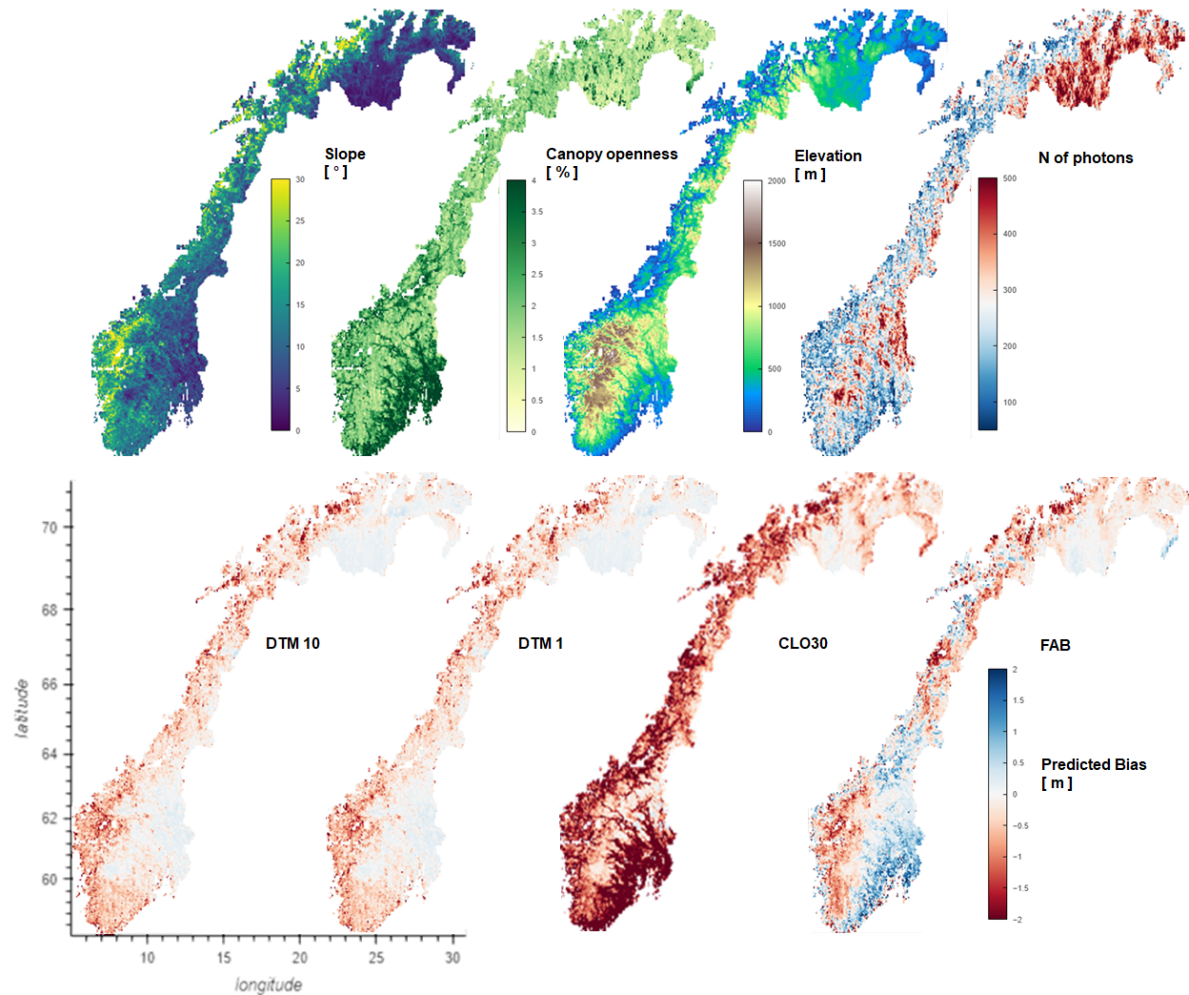


Figure 4.7.: Bias Correction Map for Snow-on Scenarios. This figure shows variations in predicted bias correction across different regions, depending on factors such as slope, vegetation cover, and the number of photons.

4. Study Case - mainland Norway

to their “ICESat-2 ATL08 snow-free condition,” which is not equivalent to the “true surface” but rather still encompasses errors from both DEM and ICESat-2 ATL08 side (further discussion in Sections 5.2.1 ,5.2.2).

The dataset’s most informative features for splitting and characterizing patterns are presented in Figure 4.8. The feature importance scores indicate the usefulness of each feature in predicting error patterns, with higher scores implying more important features. Among these features, terrain slope describes the slope along the track. The standard deviation of photons in segments (*t_te_std*) is crucial for DTM10 and DTM1 models as it represents terrain surface roughness. Canopy height and openness are also essential despite not being displayed at an aggregated map (Figure 4.7). Therefore, it is necessary to pay extra attention to errors related to canopy parameters. Conversely, metrics like *night_flag*, *pair* and *beam* of ICESat-2, and *region* (ascending or descending pass of satellite) are less important (refer to Section 5.2.1 for further discussion). For GLO30 models, top features include *Eastness* and *Northness*, suggesting that most vegetation is located in the east and south. Overall, analyzing feature importance provides valuable insights into dataset characteristics and helps identify relevant features for predicting error patterns. Section 5.2.3 will further discuss the uncertainties induced by features over snow-on and snow-free surface.

The training dataset has been divided into two parts: the training and test datasets, with 80% of the data used for training and the remaining 20% used for testing. The performances of bias correction presented in Table 4.3. The DEM10 model exhibits slightly better performance than the DTM1 model, with an NMAD of 0.549 m compared to 0.551 m for DTM1. This difference in performance could be attributed to the fact that the terrain features used as input were calculated based on DTM10, and some of them may not be able to explain differences at finer scales.

Table 4.3.: Cross Validation of Bias Correction Regression

| Model | Tree Depth | N_estimators | NMAD (m) | RMSE (m) | MAE (m) |
|-----------------|------------|--------------|----------|----------|---------|
| DTM1 - ICESat2 | 10 | 250 | 0.551 | 1.345 | 0.778 |
| DTM10 - ICESat2 | 10 | 250 | 0.549 | 1.342 | 0.774 |
| GLO30 - ICESat2 | 10 | 250 | 0.901 | 1.640 | 1.042 |
| FAB - ICESat2 | 10 | 250 | 1.036 | 1.894 | 1.219 |

4.6. ICESat-2 Derived Snow Depth and Validation

The aggregated mean snow depth observed from ICESat-2 from 2018 to 2022 (all seasons) is presented in Figure 4.9. The snow depth retrieval using DTM10 and DTM1 as reference ground exhibits similar

4.6. ICESat-2 Derived Snow Depth and Validation

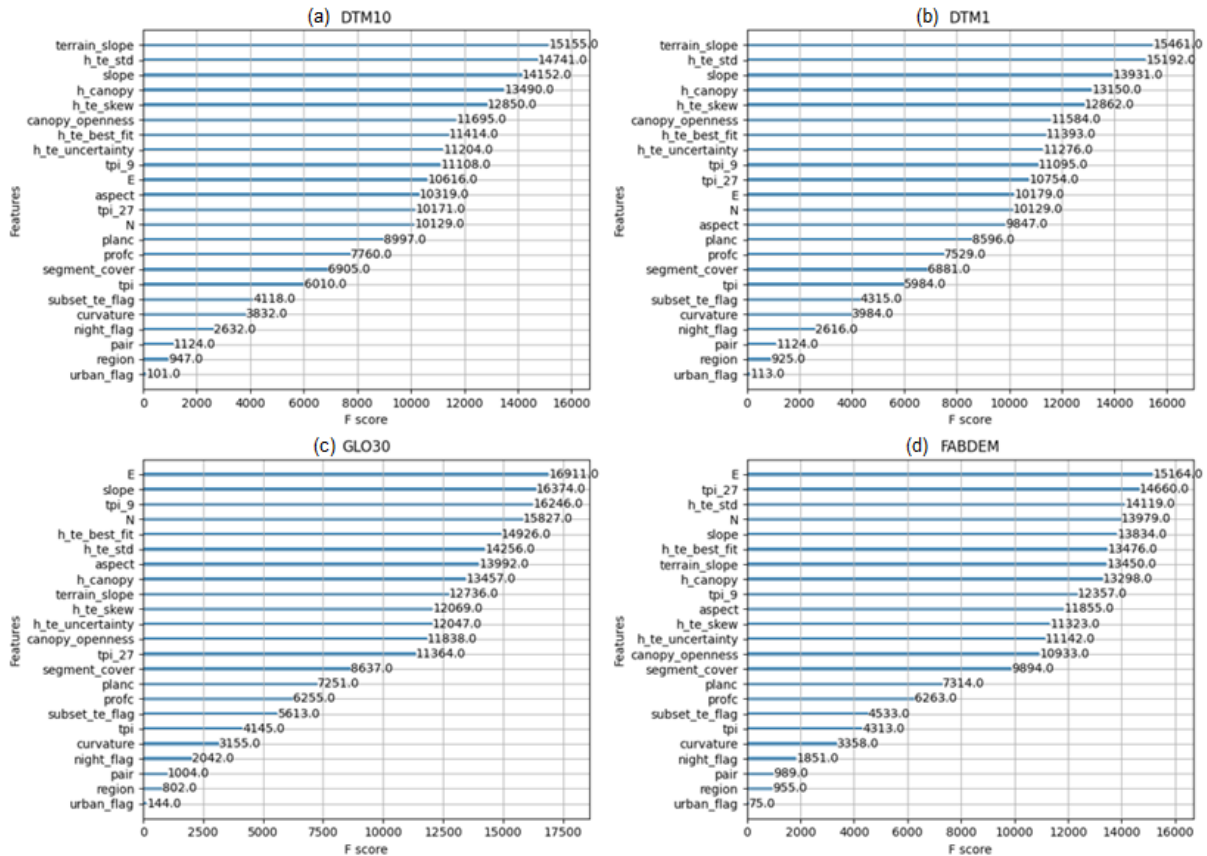


Figure 4.8.: Features Importance of Bias Correction Regression. Specifically, terrain slope, is one of the features obtained from ICESat-2, describes the slope along the track. Further explanation regarding features can be found in Section 3.2.1

4. Study Case - mainland Norway

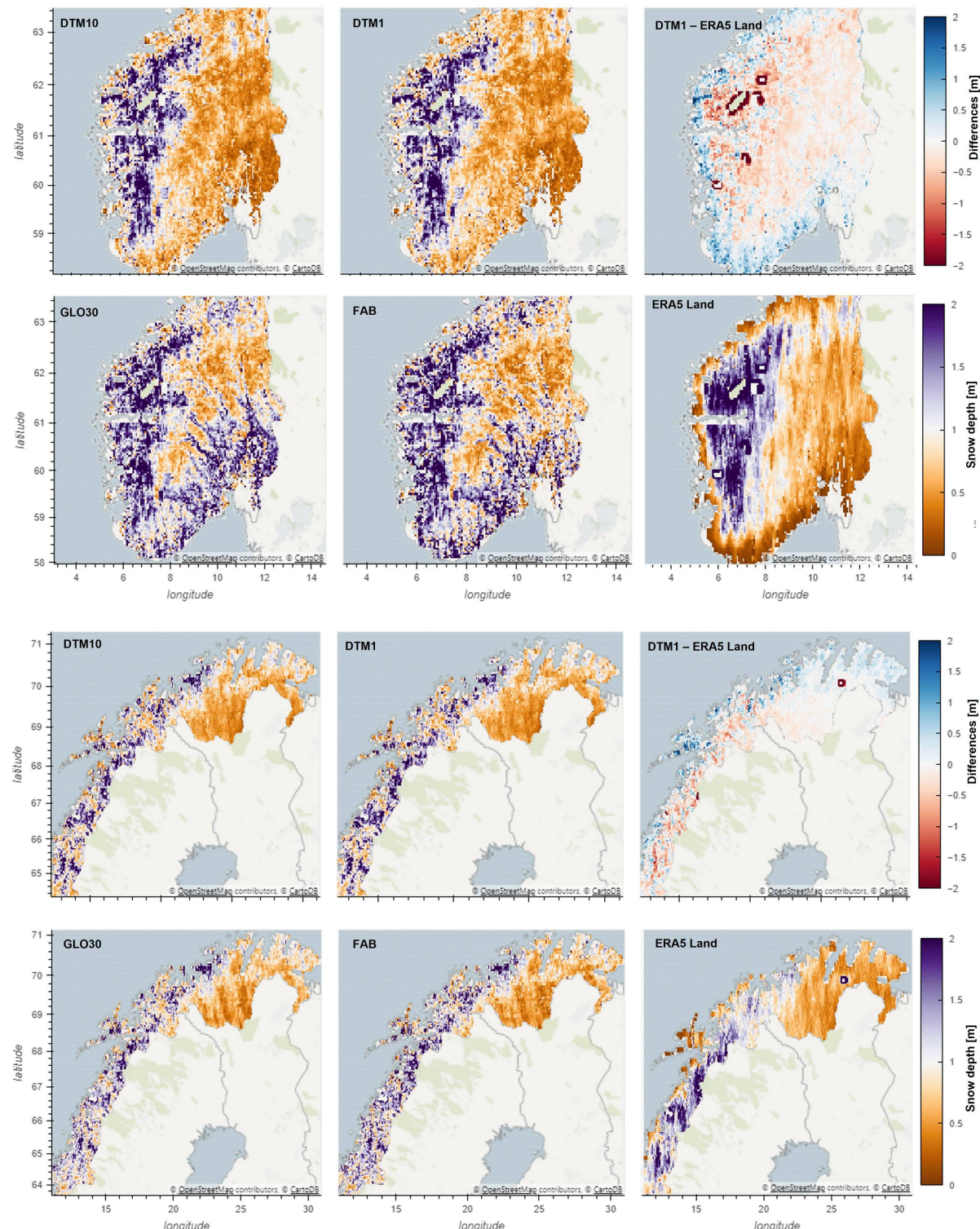


Figure 4.9.: Snow Depth from ICESat-2 and Four DEMs, 2018-2022. This figure shows the mean snow depth observed from ICESat-2 over a four-year period, using four DEMs. Purple areas indicate heavy snow accumulation, while orange indicates minimal or no snow. The cutting-out values used for DTM10 and DTM1 were -0.1m, while GLO30 and FAB used -0.5m (Section 5.3)

4.7. Dowscaled Snow Depth and Validation

patterns. GLO30 and FAB exhibited a residual bias causing an overestimation of snow depth in vegetated areas located in the eastern region. Conversely, relative flat areas with sparse canopies, such as Hardangervidda and Finnmark, display high consistency over the four DEMs.

Upon comparison of the snow depths derived from DTM1 to those obtained from ERA5 Land, it was observed that thin snow packs exhibit higher snow depth while thick snow packs exhibit lower depth. This phenomenon can be attributed to several factors including resolution effects, glacier areas, and cut-off factors. For a more detailed discussion on this differences, refer to Section 5.3.

In addition to comparing different references DEM and ERA5 Land snow depth, this section also includes a comparison with validation snow depth from a lidar survey at local scales. ICESat-2 had a pass on 5th March 2022 in Hardangervidda, followed by a drone trip on 11th March 2022. The drone trip produced 68 valid snow-on-surface measurements that corresponded to the ATL08 segments. Figure 4.10 shows a scatter plot indicating a slight difference to validation, where the ICESat-2 - DTM1 model has an R-squared of 0.94 and RMSE of 0.22 m.

The results demonstrate the high accuracy of snow depth obtained from the ICESat-2 - DTM1 model. It is important to note that although the DTM10 has a resolution of 10-meters and an R-squared value of only 0.77 with an RMSE of 0.40 m, the validation snow depth is calculated based on DTM1 as reference ground. On the other hand, global DEMs such as GLO30 and FAB achieve good fitness after applying bias correction, with R-squared values of 0.76 and 0.74 and RMSEs of 0.49 m and 0.53 m, respectively.

However, it should be noted that Hardangervidda is a unique area with relative flat terrain, thick snow-packs, and sparse vegetation. Therefore, the bias correction does not significantly improve the results over DTM1 and DTM10. The field trip also covered a limited area and cannot represent the overall performance of ICESat-2 derived snow depth. This study cannot further explore the error sources and characterize the snow distribution, such as covariance (COV). Additionally, the validation snow depth was produced using DTM1 as a reference ground which contains possible errors from DTM1 - particularly since some DTM1 tiles in this area are not entirely snow-free, as noted by Melvold & Skaugen (2013). Instead, the ICESat-2 - DTM1 model has applied the bias correction to deal with this issue (further discussion about uncertainties in Section 5.2.3).

Overall, the validation results suggest that the snow-on surface derived from ICESat-2 exhibits a high level of consistency with that obtained from lidar. However, different DEMs acting as reference can impact the accuracy performance of the snow depth product. To mitigate this effect, bias correction is necessary and useful. Aggregating the final results from GLO30 and FAB using suitable techniques could also be a solution to increase the reliability and accuracy of the date.

4. Study Case - mainland Norway

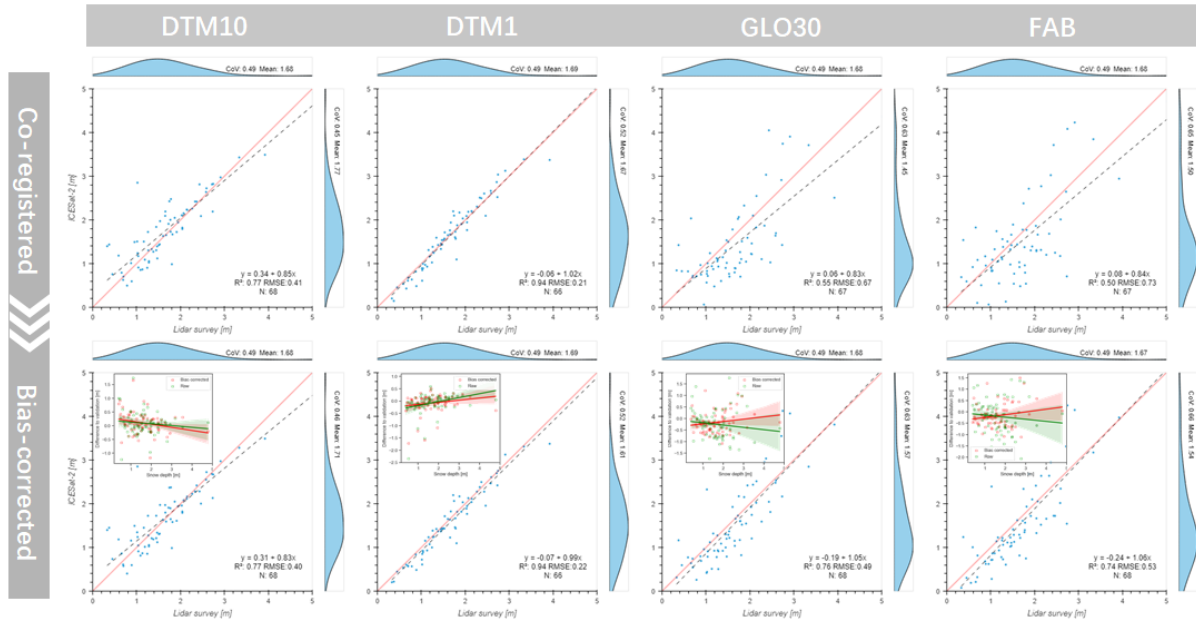


Figure 4.10.: The Vidaliltion of ICESat-2 Derived Snow Depth. The snow surface are captured by lidar, and the snow depth for validation was retrieved based on DTM1. The bias correction significant improved GLO30 and FAB.

4.7. Downscaled Snow Depth and Validation

The downscaled snow depth gives the ‘normal distribution’ of the snow depth at hillslope scales. The hillshade present many channels ranging from 10 - 30 m wide, acting as a shelter with thick snow accumulation (> 6 m from validation), and the hilltops with thin snowpack instead (Figure 4.11). The primary challenge of downscaled snow depth is related to thick snowpack in channels, which is prevalent in this area but may not be a common occurrence over the domains of features used in downscaling.

The R-square value for all DEMs is between 0.66 and 0.67. Without bias correction, DTM1 can also reach up to 0.46. The raw snow depth of GLO30 and FAB without bias correction have no correlation with validation snow depth (Figure 4.12)

There are terrain parameters, canopy information, and grid characteristics such as wind, snowfall, and snowmelt accumulation from ERA5 Land. The most critical feature is East, followed by aspect, slope, elevation, tpi and snow melting (Figure 4.13).

In summary, the downscaling of snow depth enables a normal pattern of snow distribution at hillslope scale. However, challenges arise when dealing with thick snowpacks in channels that are common in some areas but may not others. The similar ‘extreme value’ problem also exists in other downscalings, such as precipitation. The possible solution will be discussed in Section 5.4.

4.7. Downscaled Snow Depth and Validation

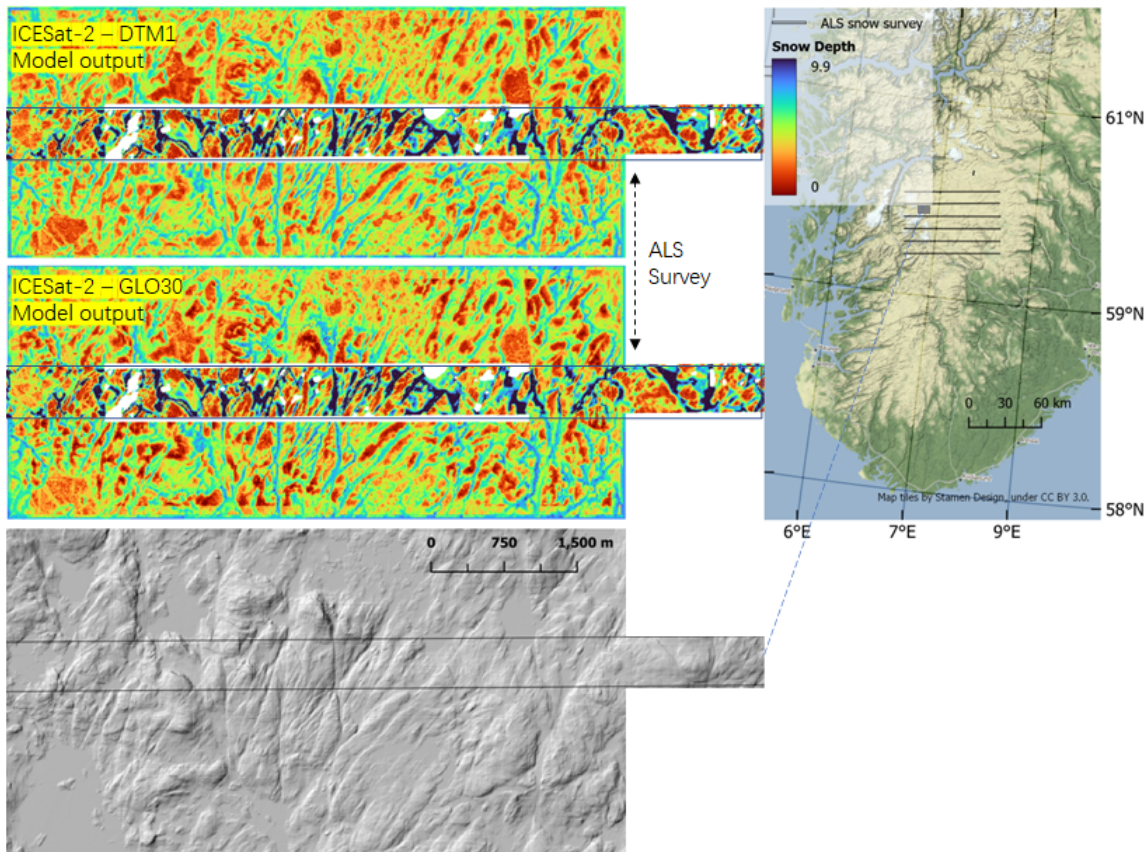


Figure 4.11.: The Vidaliltion of Snow Depth Downscaling: Map. The NVE's ALS snow survey conducted at April 2008 offered the validation snow depth. The validation strip from the northwest of the survey area shows significant variations of snow depth across channels and hilltops. The same strip also displayed in Melvold & Skaugen (2013) (Figure 3)

4. Study Case - mainland Norway

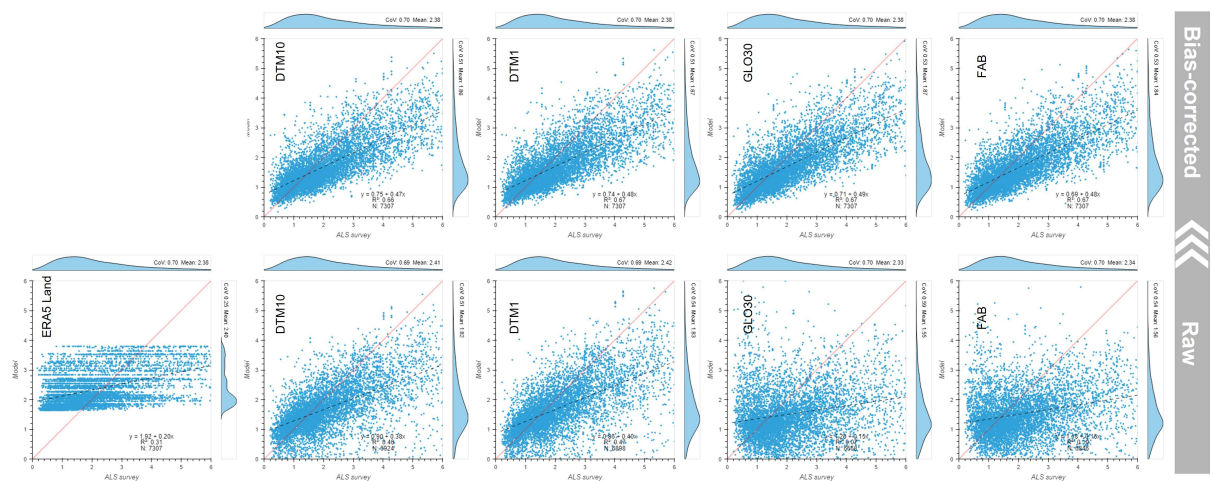


Figure 4.12.: The Vidaliltion of Snow Depth Downscaling: Scatter Plot. This figure demonstrates the significant improvement in correlation between DTM1 and validation snow depth after applying bias correction.

4.7. Downscaled Snow Depth and Validation

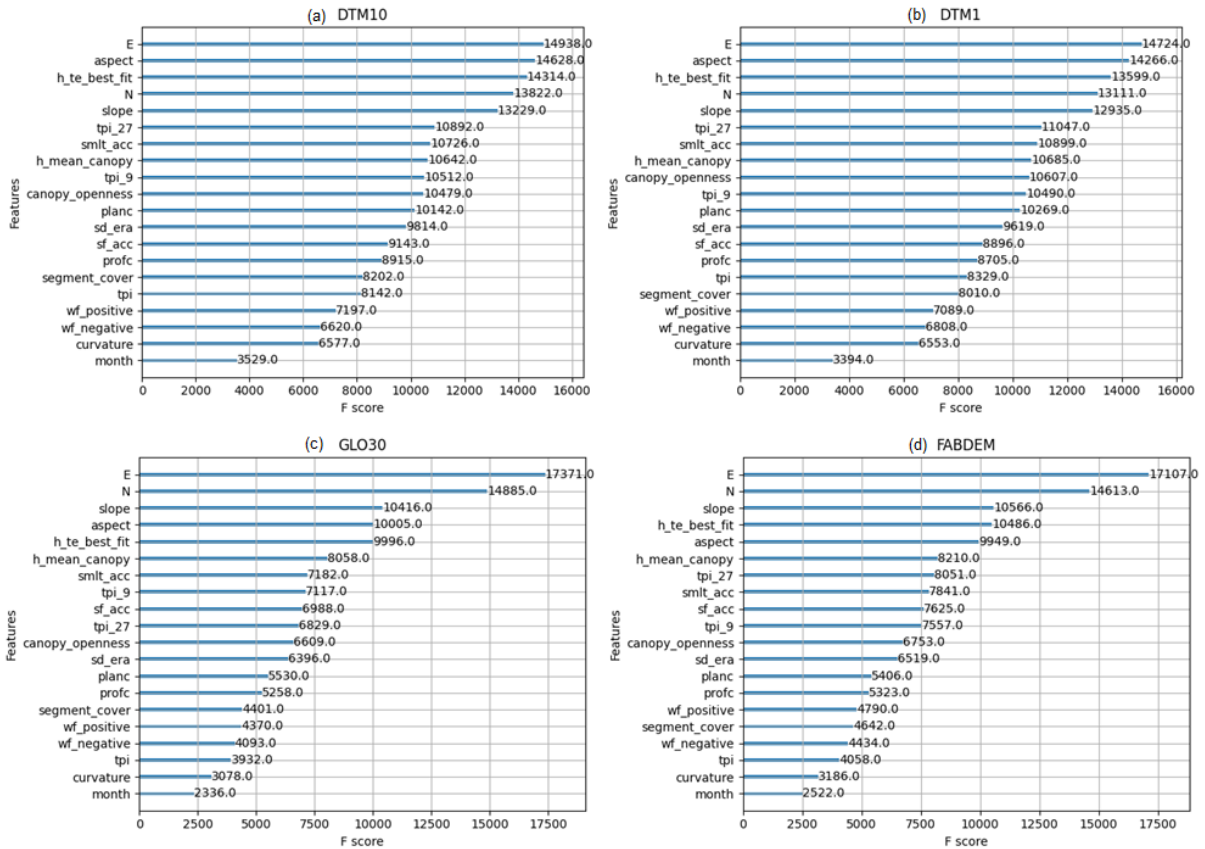


Figure 4.13.: Features Importance of Snow Depth Downscaling. The regional difference (E,N) are the most significant features. Then the elevation (t_te_best_fit) and slope, aspect, TPI. The full explanation about feature's name are described in Section 3.2.1

5. Discussion

5.1. GDC vs NuthKaab Co-registration: Which and Why

GDC (Gradient Descent Co-registration) and NuthKaab (Nuth & Kääb, 2011) address the same problem but using distinct techniques. These methods are used when georeferenced DEMs are not perfectly aligned. In cases where georeferencing information is absent, LS3D (Least Squares 3D Surface Matching), or other ICP-based algorithm, are preferred. GDC and NuthKaab solve the coregistration problem solve coregistration as a bound-restricted minimizing problem with random noise. This problem is often referred to as subpixel coregistration, which is true in most cases where the resolution is 10 m or coarser, with a misalignment of less than 10 m. However, at resolutions of 1 m or 2 m, it is no longer considered a subpixel problem. In such cases, it is recommended to solve it within the bounds of 3-5 pixels, as suggested by this study.

NuthKaab solves the coregistration problem by minimizing NMAD statistically (as implemented in xDEM) and requires calculation of terrain parameters such as slope, aspect, and sometimes curvature at least once. It operates efficiently for low workload tasks with coarse resolution or small coverage of DEMs. On the other hand, GDC solves the same problem more quickly and without requiring terrain parameters calculation. The gradient descent algorithm is used to expedite searching. During coregistration with NuthKaab, the DEM to be aligned is iteratively shifted by updating the transformation parameters in each iteration, requiring interpolation to calculate elevation differences until convergence. However, GDC only performs interpolation task on selecting points.

From a technical perspective, for scenarios requiring fine resolution DEM or extensive coverage involving large workloads, GDC is highly recommended over NuthKaab. Additionally, GDC is more suitable for coregistering two DEMs with different resolutions or for coregistering a DEM with points. Although some implementations of NuthKaab (Xdem contributors, 2021) can also handle point coregistration, it has critical requirements regarding the number of points..

5.1.1. Noise suppression

The process of coregistering DEMs using GDC requires special attention to the noise problem. If the DEM is intentionally shifted, the coregistration between the original and shifted DEM will result in a

5. Discussion

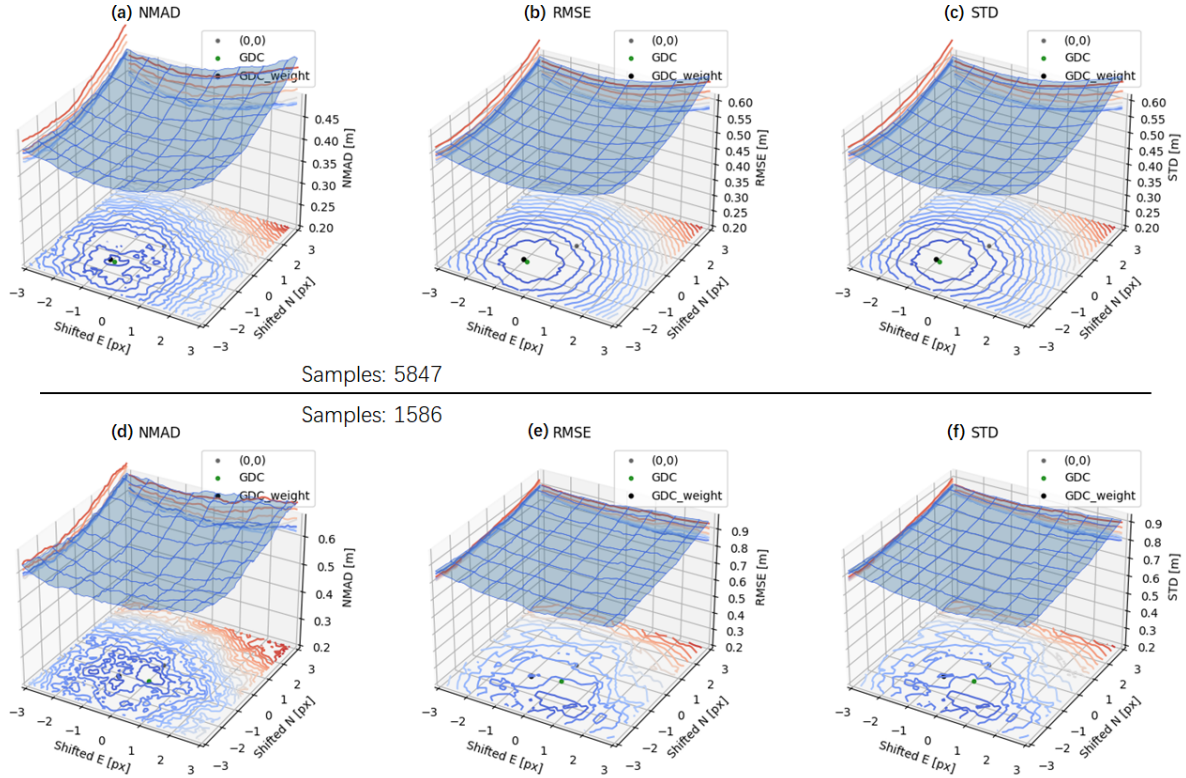


Figure 5.1.: Brute-force test on gradient descent coregistration. The plot presents the coregistration of DTM1 with 5487 points ICESat-2. It shows that NMAD offers a steeper converging surface, compared with RMSE and STD (a,b,c), where each contour line represent 3% improvements from outside to inside, and the final results of GDC and weight-enhanced GDC has inegible difference (in green and black dots). When the number of points decreases to 1586 points (d,e,f) the surface is not converging anymore as more noise interference. However, the weight-enhanced GDC still has a higher chance to give the similar results as before.

5.2. The Uncertainties: ICESat-2, DEM and Snow Depth

noise-free coregistration, and the NMAD of the final match will be technically zero. However, in practice, the two dataset to be coregistered are produced using different techniques, through different processing, transformations, interpolations, at different dates. The noise exhibits on both datasets and interferes with the real difference produced by misalignment. Therefore, excluding moving terrain and suppressing noise to achieve high-quality coregistration are critical steps.

To address this issue, this study employs snow-free segments from ICESat-2 ATL08 as a reference for coregistration. However, limited snow-free measurements are available in high altitude areas when DTM1 has relatively small coverage. To mitigate noise interference, several practices can be implemented:

- Increasing the number of sampling points: Each ATL08 segment has five subsegments. When there are not enough points, this study used the subsegments as well.
- Using points with good qualities. This study adopted weight for points from ICESat-2 quality features and masked out low-quality points.
- Using a robust estimator to reduce the influence of outliers. NMAD is better than RMSE or STD (Figure 5.1) as a cost function under critical conditions. It gives sharper and more robust results compared to RMSE or STD, which are sensitive to outliers and vertical bias.
- Filtering by standard deviation or quantiles can also exclude outliers by t-distribution.
- In some cases of coregistration, vertical bias correction may be useful. However, this study cautions against applying vertical bias correction if there is no confirmation that the DEM was produced under snow-free conditions since snowpack on surfaces can lead to incorrect vertical bias correction due to negative skewness.

Overall, suppressing noise during coregistration is crucial for achieving accurate results. Employing these practices can help mitigate noise interference and ensure high-quality coregistration results.

5.2. The Uncertainties: ICESat-2, DEM and Snow Depth

5.2.1. ICESat-2 ATL08: skewness and curvature

The stability and consistency over different conditions and periods are crucial for a reliable dataset. The data binning can be used to quantify errors and determine if there are any systematic biases. As shown in Figure 5.2 the elevation difference between ATL08 snow-free and DTM1 are dividing into smaller groups, where the following factors have been considered under control:

- The background noise is a significant factor affecting bias. The lidar sensor experiences interference from skylight, resulting in better performance at night. The median of the differences between night observations and DTM1 is stable at 0 m, while day observations have a negative

5. Discussion

median ranging from -0.05 m to -0.1 m, both tending to give negative estimations, indicating by Q1 and Q3 (Figure 5.2 a)

- The quantity of photons is crucial as it affects ground-finding algorithms' performance. The Figure fig@quantile_metrics in previous section show that the least 5% of $n_{photons}$ quantiles has biggest NMAD and negative mean error, comparing to conditions with sufficient photons.
- The snow free segments is produced under 'snow free condition' classified by NOAA daily snow mask products. The brightness reveals the presence of small snowpack which is wrongly classified into 'snow free condition'. Figure 5.2 c show that the 'snow pack' contributes the positive bias (~ 0.2 m to 0.3 m).
- The pair 1,2,3 exhibit a slightly negative bias of around 0.1 m (Figure 5.2 b)
- The interpolation algorithms such as h_{te_interp} or $h_{te_bestfit}$ can affect accuracy. Some studies show that $t_{te_best_fit}$ has slightly higher accuracy and smaller variation than h_{te_interp} (Neuenschwander & Pitts, 2019; Tian & Shan, 2021). This study test on h_{te_interp} it does make the results better.
- The strong or weak beams play an important role in signal-to-noise ratios over low reflectance objects (such as sea) or complex geometry (such as dense vegetation) (Neuenschwander & Pitts, 2019). However, there is no noticeable bias between strong and weak beams on this snow-free dataset of this study.
- Moreover, the consistency from the year 2018 to 2022 appears to be acceptable (Figure 5.2 a,b,c).

The most critical issue with ATL08 products identified in this study, as well as previous studies, is the vertical sampling error. The ground-finding algorithm of ICESat-2 relies on a probability distribution function (PDF) of the reflecting surface. So that, the dense vegetation can hinder photons from accurately reaching the ground surface, leading to this error (Neuenschwander et al., 2022). This error can also impact canopy height determination consequently. Additionally, slope naturally translates horizontal shift (i.e., footprint or geolocation error) into vertical shift (Deems et al., 2013), which may be related to negative skewness noted in many studies (Enderlin et al., 2022; Tian & Shan, 2021). This study highlights that negative bias exists on all pairs of ATL08 snow-free - DEMs in terms of slope, with GLO30 and FAB exhibiting more severe negative bias than DTM10 and DTM1 (Figure 4.4, A.2). However, the significant negative bias is observed only on convex terrain while being totally different over concave terrain indicated by positive TPI, curvature, plan curvature and negative profile curvature (Figure 4.4 and 4.5).

Figure 5.3 utilizes profile curvature and plan curvature to show the mean value of elevation differences under various curvature combinations. The plot reveals that convex ridged terrain (positive plan curvature and negative profile curvature) typically exhibits the negative skewness (Figure 5.3 a). A concave bowl-shaped terrain with negative profile curvature does not much negative skewness, even at high slopes (Figure 5.3 c), thereby indicating that the observed linear relationship between bias and slope (Figure 4.4 b) is mainly contributed by plan curvature. Moreover, the canopy height contributes

5.2. The Uncertainties: ICESat-2, DEM and Snow Depth

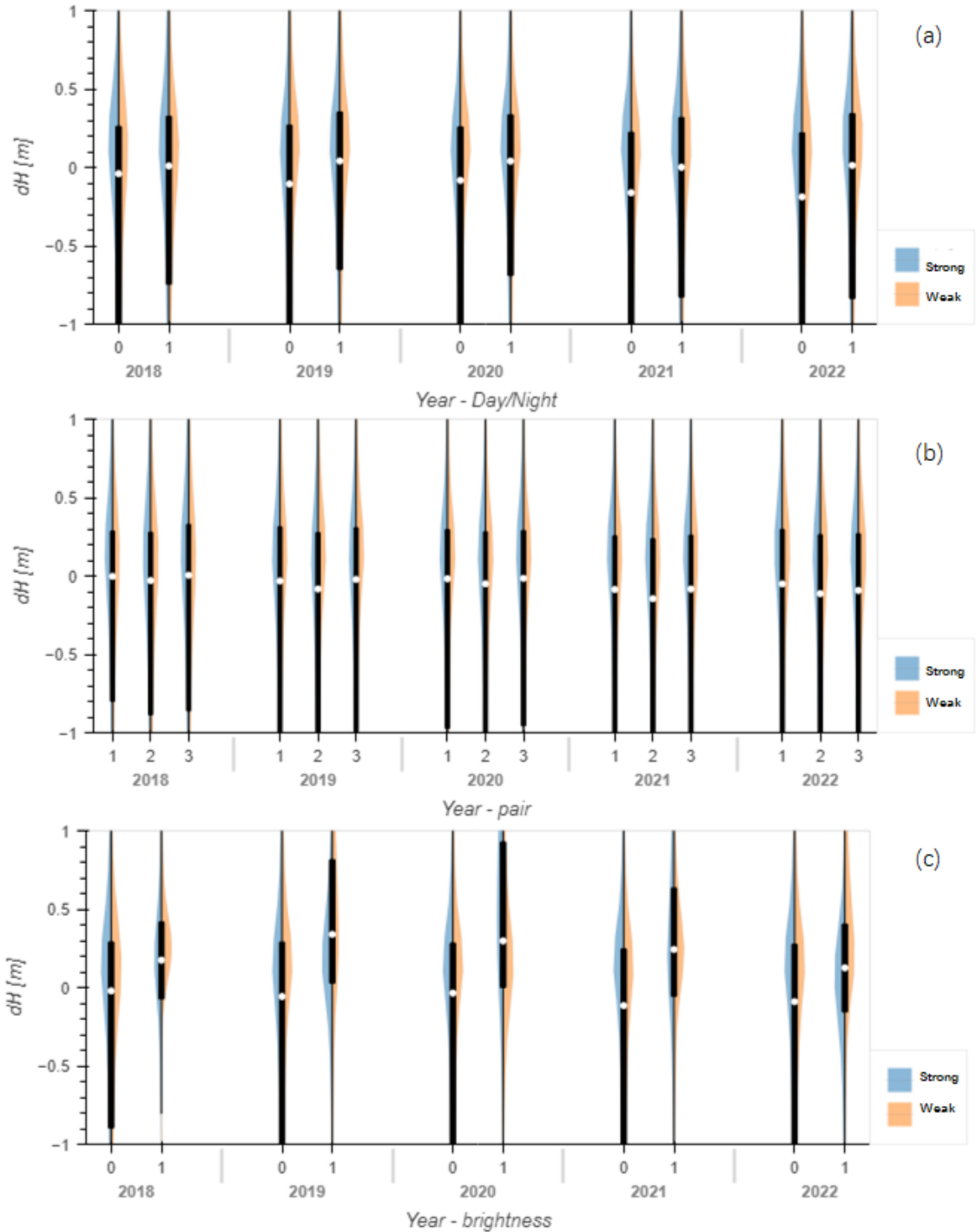


Figure 5.2.: ICESat-2 Consistency: Year, Day/night, Strong/Weak, Beams and Pairs. The x-axis is grouped by year and further sub-categorized by day/night (0/1), pair (1/2/3), and brightness (0/1). The plot is split based on the strong and weak beam. The median is represented by a white dot, while the thick bar's edge indicates the 25% (Q1) and 75% quantiles (Q3), respectively.

5. Discussion

significantly to positive bias when the canopy is short upon concave terrain, but it cannot equalize for all the observed negative skewness as well (Figure 5.3 d). Therefore, it can be inferred that plan curvature plays a significant role in influencing skewness. Based on these findings, this study does not recommend any bias correction based solely on slope and/or canopy height.

The mechanism responsible for the observed negative skewness remains unclear. If the DTM1 is deemed to be an accurate representation of the surface, then this study can attribute the bias to ATL08. In such scenario, it is plausible that ATL08's ground finding algorithm employed has a tendency to capture lower signals, resulting in an underestimation ((estimate lower than the actual)) of convex surfaces while accurately capturing concave surfaces.

The two possible components may contribute: (1) Naturally, there is overestimation over concave, but underestimation of convex due to the limitation of coarse resolution (or footprint, see examples in Figure 5.4 a and A.3 a). Still, this should be symmetrical bias and not as significant as what we observed in terms of negative skewness. (2) Trees present in concave and convex may lead to skewness. As observed overestimation on convex terrain (Figure 5.3 d, with a reddish tint at the bottom left) may have occurred due to the misclassification of short canopy as terrain surface. This misclassification is less likely to occur in concave terrain or areas with taller trees because trees are discernible from their surroundings due to their height. However, both misclassification and resolution limitations cannot fully account for such significant negative skewness. On the other hand, if ATL08 provides an accurate surface representation, it is possible that DTM1 overestimates convex surface.

5.2.2. Uncertainties in DEMs: vegetation, resolution

The presence of surface objects, such as vegetation and buildings, can also introduce negative bias in this analysis. COP30, for instance, is susceptible to such biases (Figure 4.7), which can complicate error assessment. Therefore, it is crucial to evaluate whether bias correction techniques can eliminate the impact of surface feature, and identify any residual errors after correction. One way to investigate this is by comparing COP30 with FAB DEMs that exclude trees and buildings. To facilitate this comparison, we can use DTM1 as a reference surface for evaluating the two DEMs before and after bias correction. By doing so, we can gain insights into the effectiveness of bias correction methods in mitigating the impact of surface objects on terrain data analysis.

The Figure 5.4 illustrates the differences between FAB, GLO30, and DTM1 in terms of plan curvature and canopy height. The scatter points are symmetrically distributed, indicating an balanced spread of trees over convex and concave terrain. The color scheme shows that FAB has effectively removed the forest, resulting in a positive bias over concave areas and a negative bias over convex areas with equal strength due to resolution limitations. GLO30 has a higher surface than DTM1 due to the presence of trees, which masks the difference except when canopy height cancels with negative bias over convex terrain, where GLO30 suffers from similar limitation due to resolution (Figure fig@:dem_dtm1 a,b).

5.2. The Uncertainties: ICESat-2, DEM and Snow Depth

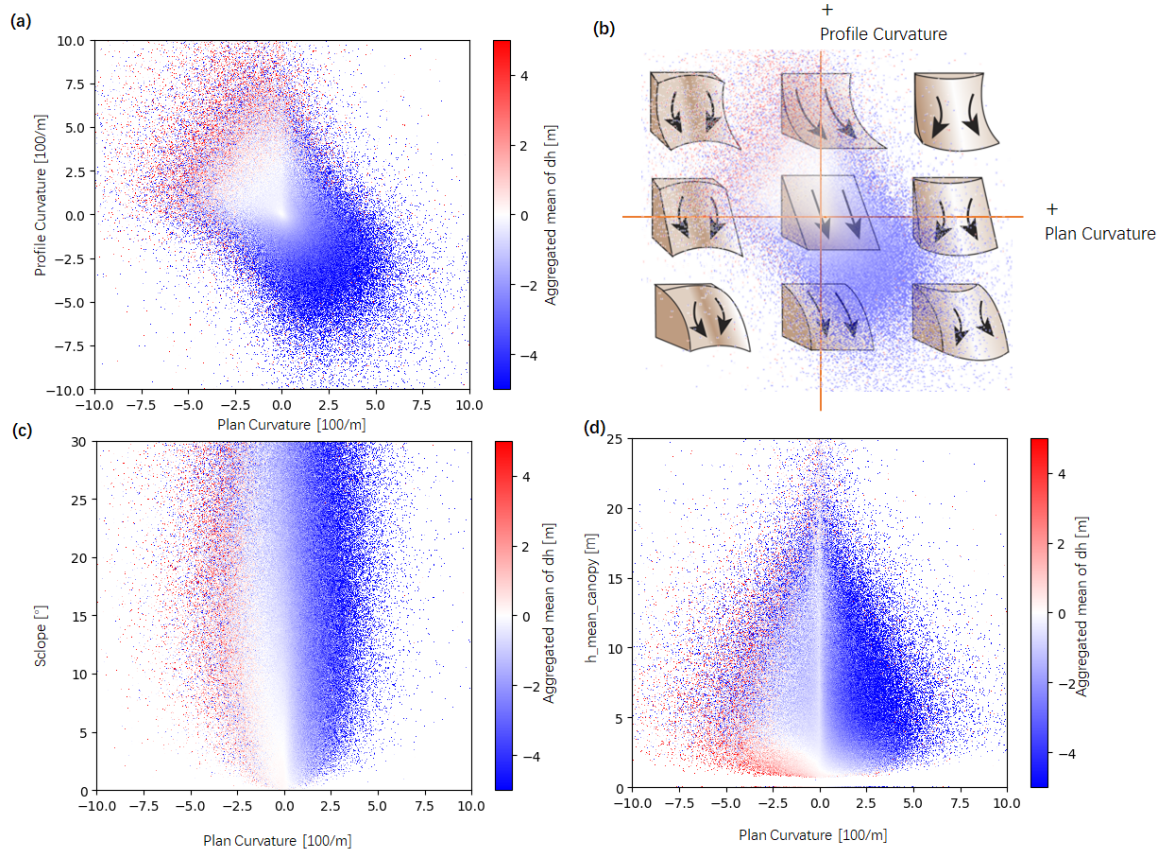


Figure 5.3.: Skewness Variations in Convex and Concave Terrains. The elevation difference is between ICESat-2 snow free segments and DTM1 after co-registration. The color points indicate the aggregated mean value of the elevation difference. Plots (a), (c) and (d) depict the bias pattern along plan curvature, profile curvature, slope and canopy height. A triangle window (a) indicating a bias free condition, the rest of area either give negative bias (blue) or positive bias (red). Plot (b) shows a schematic of curvature combinations, with dots representing the same sampling points with (a). The plot reveals that there is a negative correlation between profile curvature and plan curvature. For instance, the negative profile curvature always indicates positive profile curvatures Peckham (2011). Plot (b) is modified from Kimerling et al. (2016)

5. Discussion

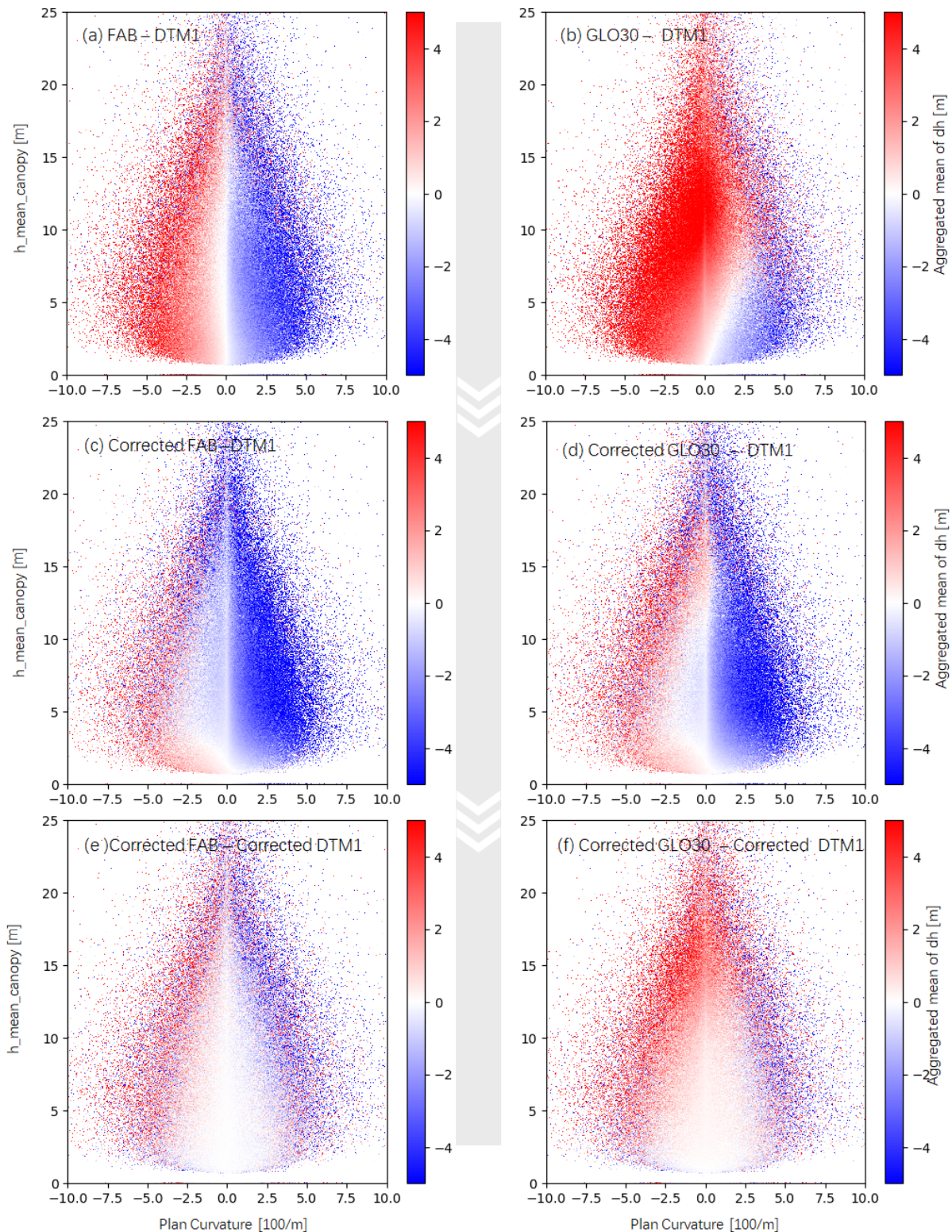


Figure 5.4.: Comparison of FAB, GLO30, and DTM1 in terms of Plan Curvature and Canopy Height. The color points indicate the aggregated mean value of the elevation difference of DEMs.

5.2. The Uncertainties: ICESat-2, DEM and Snow Depth

The bias correction process involves using ICESat-2 snow-free segments to correct DEMs. This results in corrected DEMs with similar patterns (Figures 5.4 c,d and 5.3 d (ICESat-2 - DTM1)). After applying the same bias correction on DTM1, FAB remains higher over concave terrain and lower over convex terrain compared to DTM1. Meanwhile, GLO30 retains vegetation height primarily for concave terrain. Both DEMs retain residual errors from the initial condition that will be considered in determining the final snow depth. However, the triangular area also indicates a bias-free window over flat terrain with short canopy (Figures 5.4 e,f)

DTM1 and DTM10 are produced using lidar technology, which involves a crucial step in removing non-ground objects, such as vegetation and buildings (X. Liu, 2008). Therefore, it is critical to determine if the forest has been effectively removed; however, this study does not have validation for this claim. Additionally, it is important to consider whether DTM1 and DTM10 have retained any snowpacks. As training elevation from snow-free segments is strictly snow-free; if DTM1 overestimates the surface height due to snowpack, it will be corrected to bare ground by ATL08.

5.2.3. Uncertainties of snow depth: assumptions and solutions

5.2.3.1. A bias and variance framework of elevation differencing

How do uncertainties in DEMs impact the accuracy of snow depth measurements? What are the consequences of using a DEM that is not completely free of snow cover? In error propagation practice (Equation 3.11), a dataset with three times better precision than another accounts for 90% of the variance in the output of elevation differencing. Therefore, a more precise dataset can be used as a true surface (Höhle & Höhle, 2009; Maune, 2007) to evaluate and correct any biased dataset. These surfaces are usually obtained from ground-based surveys or airborne lidar.

The framework for evaluating snow depth from elevation differences is depicted in Figure 5.5. The snow-on surface obtained from lidar can be considered as the true surface, and the distance between the lidar snow-on surface and the DTM1 reference represents the snow depth for validation (SD_{vd}). Previous analysis has demonstrated that the snow depth obtained from ICESat-2 snow-on segments to DTM1 (SD_{id}) and bias-corrected DTM1 (SD_{idd}) display a substantial R-squared value of 0.94 to validation, indicating that the influence of errors in snow-on segments (dh_{iv}) and bias correction on DTM1 (dh_{ddd}) is relatively negligible. In contrast, other DEMs are unable to achieve such a good fitness due to quality issues involving both bias and variance (See Figure 4.10).

The elevation differencing method can be used to retrieve snow depth in four scenarios. (1) The first scenario involves repeat ICESat-2 segments, where the retrieved snow depth is assumed to be bias-free after two independent measurements, and the variance is the sum of the variance of two measurements. (2) In the second scenario, when the reference snow-free DEM exhibits higher accuracy and precision, uncertainties mainly arise due to ICESat-2 snow-on surface (dh_{iv}). (3) On the other hand,

5. Discussion



Figure 5.5.: Framework for Evaluating Snow Depth from Elevation Differencing: the assumption and the uncertainties. This figure illustrates the four scenarios in which the elevation differencing method can be employed for retrieving snow depth, depending on the accuracy and precision of reference DEM and ICESat-2. Due to the limited cross-over points available with ICESat-2, the use of a reference DEM and bias correction is necessary. The fundamental assumption underlying this method is that both snow-on and snow-free segments exhibit the same bias trend, thereby allowing for equalization of the bias stemming from ICESat-2.

5.2. The Uncertainties: ICESat-2, DEM and Snow Depth

if the reference snow-free DEM possesses lower accuracy and precision, a bias correction trained by ICESat-2 snow-free surface must be applied to minimize the bias. The residual bias and variance of regression model can be used as quality metrics for retrieved snow depth. (4) In case both possess similar precision and accuracy, DEM should still be corrected to act like a ‘snow-free segment’ to equalize the bias on snow-on surface. The variance of snow depth should be the sum variance of regression model and double dh_{iv} .

To summarize, the bias from either DEM or ICESat-2 can be removed using a regression model of bias correction based on ‘same bias assumption’. The overall variances of elevation differencing snow depth can be described by summing up the variance of regression model (as shown in Table 4.3) and ICESat-2’s variance.

5.2.3.2. Assumptions: snow-on vs snow-free

The workflow presented in this study assumes that there is a consistent bias pattern in ICESat-2 elevation measurements, regardless of the presence or absence of snow. However, it is crucial to assess the validity of this assumption. Does the elevation difference between snow-on and DEM display the same bias pattern as the elevation variation between snow-off and DEM? Currently, no fieldwork or studies have collected data on snow surfaces over such a large area when ICESat-2 passes in real-time.

When transitioning from a snow-free surface to a snow-covered surface, the bias of ICESat-2 may fluctuate due to changes in surface roughness, reflectivity, and canopy height caused by snow cover. Generally, the bias is lower when more photons are available, leading to lower uncertainties. This is reflected in features such as the number of photons (*n_te_photons*), signal-to-noise (*snr*), and uncertainties (Figure 5.7).

However, it’s important to note that the bias correction model is trained on a snow-free surface, predicting the bias for *snow-free segment - DEM*:

- The correction may be over if applied this correction to snow-on segments, particularly where DEM offer accurate surface and when there is no extra features describe the bias of ICESat-2.
- The correction may be under, when there are features mainly describing the bias of ICESat-2, but ignoring the feature explaining bias from DEM, especially where DEM has a more significant impact on the results

5.2.3.3. Solutions: feature engineering

Feature engineering is the process of selecting, extracting, and transforming useful features from raw data to create new input variables that can improve the performance of machine learning models.

5. Discussion

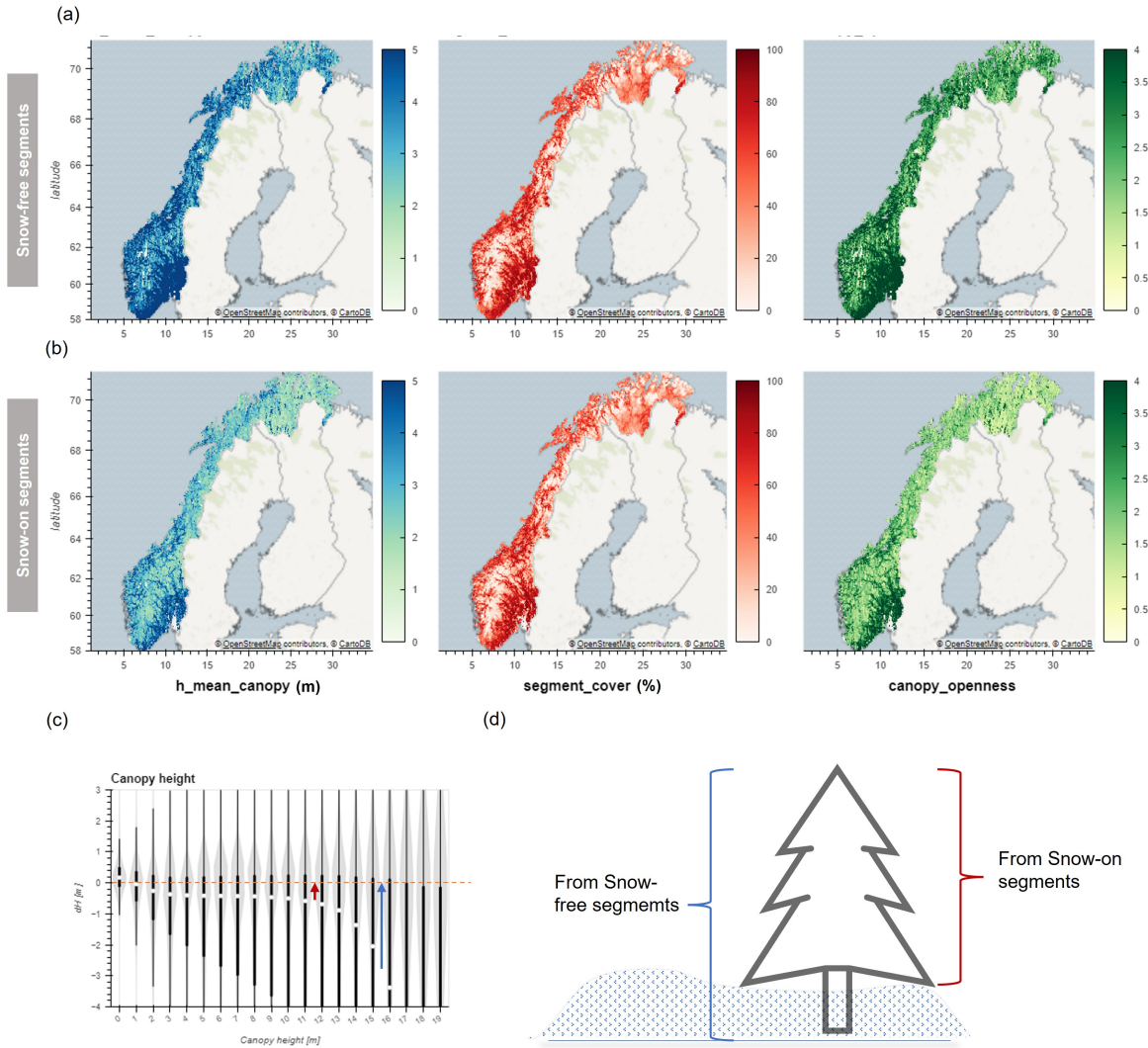


Figure 5.6.: Distribution of Vegetation Height in Snow-free and Snow-on Segments. This figure shows the difference in mean canopy height between snow-free and snow-on segments, as well as the canopy openness (a,b). The presence of snow cover results in a reduction of relative height between the canopy top and ground (d). The vegetation height can affect bias correction and potentially lead to underestimation of correction when the canopy is shorter (d). The segment_cover is a third-party metric that follows the same distribution, which indicates that the differences observed are not a result of sampling bias.

5.3. ICESat-2 Derived Snow Depth VS ERA5 Land: Cutting-out and Overestimation

Specifically, the regression model of bias correction is influenced by selected features such as vegetation height and canopy openness. Figure 5.6 illustrates that vegetation height varies greatly between snow-free and snow-on segments, with the mean canopy height being significantly taller under snow-free conditions. When the ground surface is covered by snow, the elevation measurement from the ICESat-2 lidar will include the snow surface height, and thus the resulting canopy height shorter than the actual height of the vegetation canopy. Furthermore, canopy openness (i.e., standard deviation of canopy height) is also larger under snow-free conditions indicating fewer photons classified as canopy photons.

Therefore, using canopy features from ICESat-2 in bias correction may underestimate the true value due to shorter canopies under snow-on conditions, requiring a correction method (Figure 5.6 c). Correcting the canopy height from snow-on condition to snow-free condition can be a challenging task, as the amount and distribution of snow can vary greatly within the segment. One possible approach is to use machine learning algorithms to develop a model that can predict the canopy height based on the canopy height from snow-free conditions and other relevant variables. Furthermore, it is recommended to incorporate the third-party vegetation ancillary data to mitigate this limitation, such as *segment_cover* from Copernicus Global Land Cover (Buchhorn et al., 2020). In this study, additional regression models was applied to both *h_mean_canopy* and *canopy_openness* from snow-on segments before implementing them into the model (See Appendix A.3).

On the other hand, after careful comparison, it is not recommended to use other features such as the number of photons (*n_te_photons*) and signal-to-noise (*snr*) in the regression model. These feature are efficiently explain the accuracy and precision of ICESat-2, for example, ICESat-2 has more photons available and yield lower uncertainties over snow-on surface. They do not provide consistent results across all surfaces. Their behavior is highly variable and dependent on the presence or absence of snow cover. As such, including them in a regression model would not yield reliable predictions.

In summary, to achieve an accurate regression model, one must consider and understand the potential biases present within both ICESat-2 and DEM. The predictors may seem essential initially; however, their effectiveness could vary significantly depending on external factors like snow cover. As a result, selecting more reliable predictors that consistently produce dependable results across all surfaces is key when building an effective model.

5.3. ICESat-2 Derived Snow Depth VS ERA5 Land: Cutting-out and Overestimation

After applying the bias correction to elevation difference between snow on segments and DEM, mainly to compensate the negative skewness, the residual differences are interpreted as snow depth. Figure 5.8 show the difference between ICESat-2 derived snow depth (2018-2022) with snow depth coupled

5. Discussion

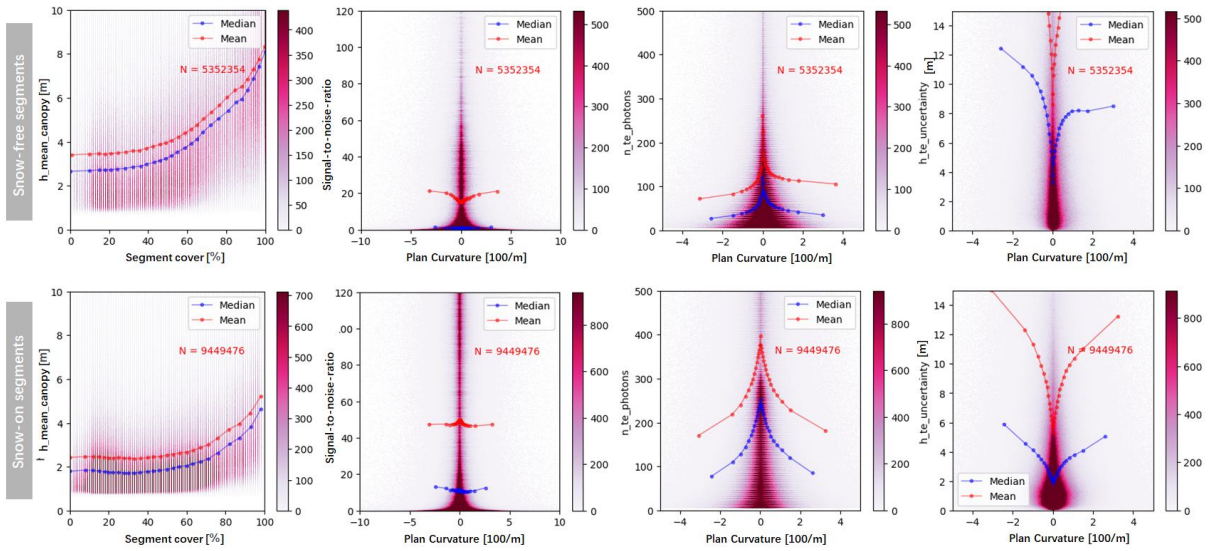


Figure 5.7.: Features Related to Snow-on and Snow-free surface. The features in different surface behavior very different in terms of canopy height, number of photons, signal-to-noise-ratio, and uncertainties. These features play a crucial role in explaining the accuracy and precision of ICESat-2. However, they fail to account for the bias introduced by DEM when it is the primary source of bias. The extra correction may need when use these features. The density of point has been normalized.

from ERA5 Land reanalysis. The aggregated mean snow depth represent mean bias at the national scales. Redish represents the overestimation of ERA5 Land snow depth, or could also be interpreted as underestimation of ICESat-2 derived approach. The density plot indicates that as the snow depth increases, the magnitude of the difference also increases.

The difference can attributed to several factors. Firstly, due to the edge effect of a 9 km resolution grid, pixels located outside the glacier mask still contain thick snow from aggregation, leading to overestimation. Similarly, in areas with a transition from snow-free coast to thick snow mountain, ERA5 Land underestimates the snow depth for the same reason (Figure 5.8). On the other hand, the ICESat-2 approach in areas with thin snow coverage could also lead to overestimation. This is related to ‘negative snow depth’, a typical phenomenon from elevation differencing, which results in overestimation if not deal with appropriately. Melvold & Skaugen (2013) used a threshold of -1 m as cutting out values in NVE’s ALS snow survey.

The cutting-out of negative values can significantly impact snow depth statistics, particularly in the coastal region. This study set cutting-out values between -1 m and 0 m resulted in significant changes to statistics, particularly for coarse resolution DEMs. Approximately 2 million data points fell between -1 m and 0 m, and after removing these points, the median and mean shifted by 0.2 m to 0.3 m (Figure 5.9). Therefore, researchers must exercise caution when selecting thresholds for cutting-out negative values.

5.3. ICESat-2 Derived Snow Depth VS ERA5 Land: Cutting-out and Overestimation

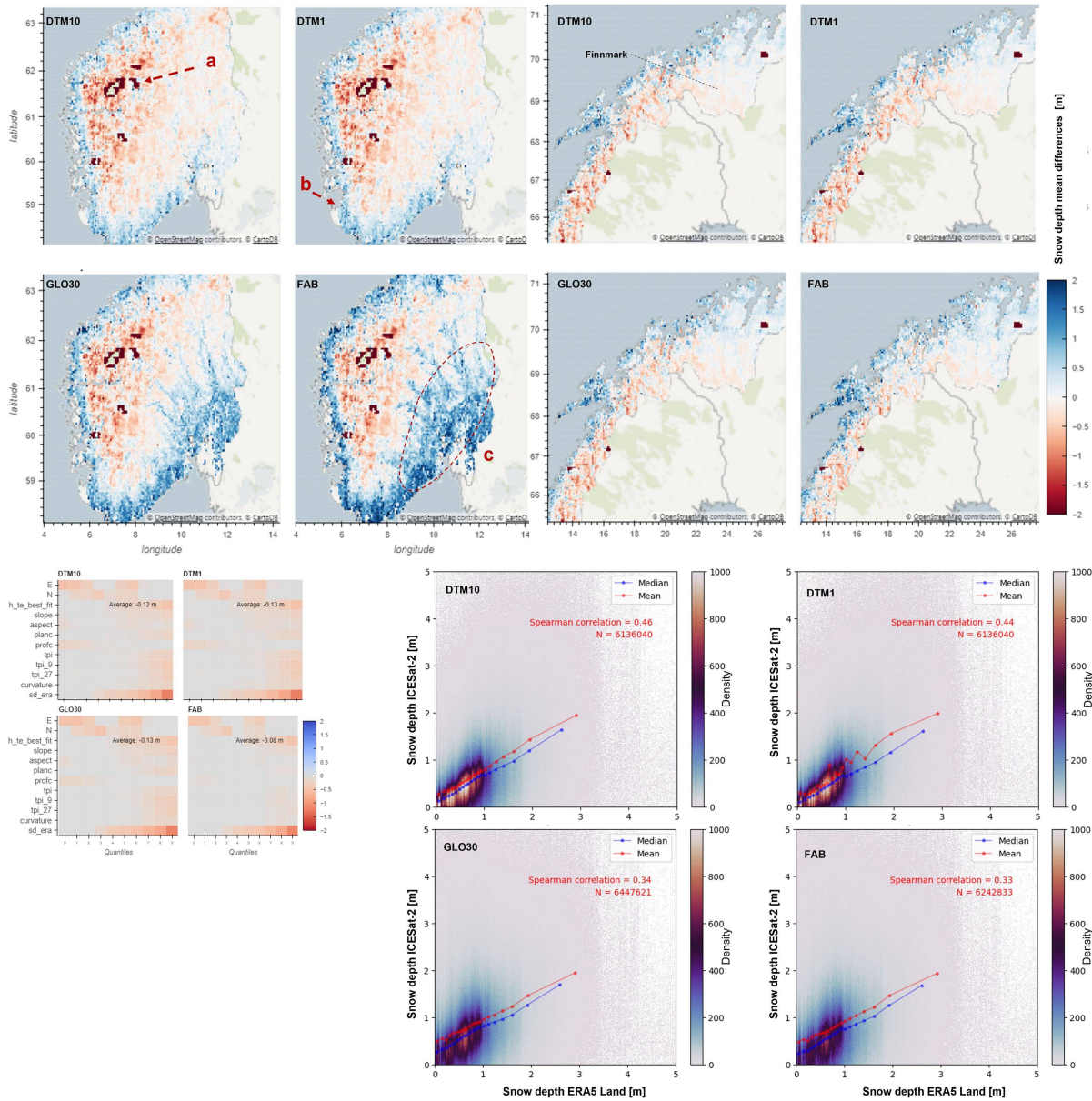


Figure 5.8.: ICESat-2 Derived Snow Depth VS ERA5 Land Snow Depth. The figure displays the difference between ICESat-2 derived snow depth (2018-2022) and snow depth coupled from ERA5 Land reanalysis. The comparison highlights a systematic bias between the two datasets, with variations observed across different regions, such as glacier areas (a), coastlines (b), and tree coverage areas (c). Notably, the Finnmark region exhibits minimal differences in snow depth measurements. The cutting-out values is 0 for all four models.

5. Discussion

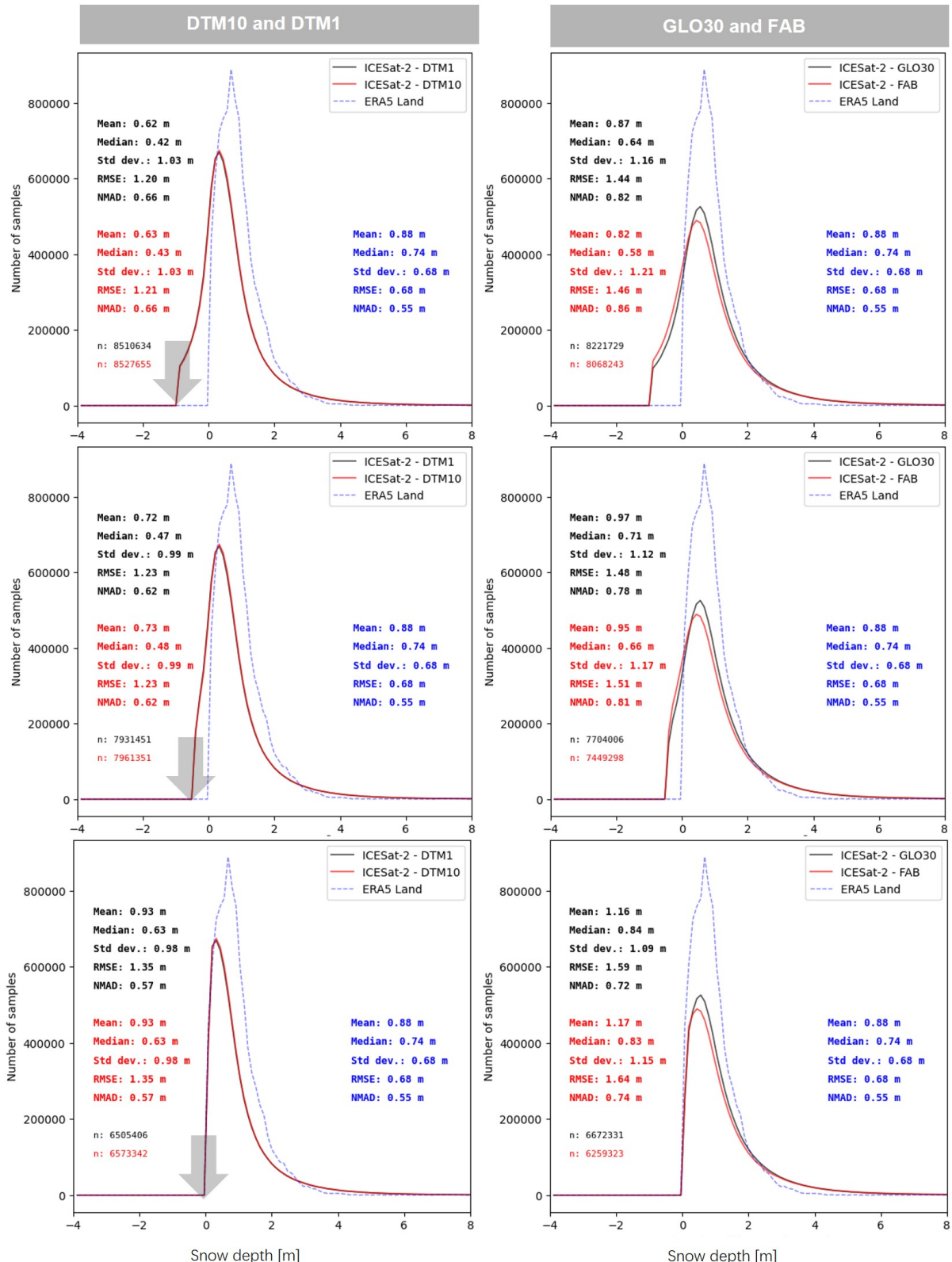


Figure 5.9.: Impact of Cutting-out Negative Values on Snow Depth Statistics. Histograms depict the variation in median, mean, and range of snow depth values for different cutting-out thresholds, highlighting the importance of careful threshold selection

5.4. Downscaling and subgrid distribution

The bias correction applied in this study made the distribution more symmetrical but did not entirely eliminate negative values. Nonetheless, it is worth noting that this comparison does not determine which dataset is more accurate.

5.4. Downscaling and subgrid distribution

The downscaling of snow depth has several limitations. Firstly, the variables used are insufficient to fully express the snow depth distribution. For instance, the model ignores the seasonal changes in vegetation, and the wind variables are coarse in resolution (9 km), which does not fully capture the variability of wind with respect to vegetation, terrain aspect, and surface roughness. Secondly, the model disregards gravity processes such as avalanches. Thirdly, potential errors may be introduced by the ERA5 data. Its consistency in performance during accumulation and melting periods may vary. Therefore, the bias pattern could differ, but the regression model does not correct for this inconsistency intentionally. Lastly, a historical training dataset of 4 years is insufficient since climate studies require a 10 to 30 year dataset to represent climate normal (Arguez & Vose, 2011).

To improve results, several possible ways can be explored. Firstly, it is important to note that snow depth follows a gamma distribution as shown in Gisnås et al. (2016). Therefore, instead of assuming that $x - \mu$ follows a normal distribution in regression where x represents sample values of snow depth and μ represents true mean of population (the snow depth from ERA5 Land); it is better to determine what kind of distribution can represent local variability of snow more accurately. Secondly, further quality control on ICESat-2 derived snow depth should be done with additional imagery datasets that can detect thin snowpacks accurately and correct ICESat-2's derived snow depth measurements accordingly. Lastly, feature engineering such as vegetation parameters can be improved by incorporating third-party data sources.

In summary, improving downscaling methods for snow depth requires addressing limitations such as inadequate variables and ignoring gravity processes like avalanches while considering potential errors from ERA5 data and historical training datasets' short length. Possible solutions include using gamma distributions for accurate representation of local variability in snow depths; incorporating additional imagery data for quality control of ICESat-2 derived snow depth; and improving feature engineering with third-party data sources.

A. Appendix

A.1. Additional Figures

A.2. Technical Details of ICESat-2 ATL08

A.2.1. Processing and QC Steps of ICESat-2 ATL08 Land products

This is a set of instructions for computing segment parameters for the land products from Neuen-schwander et al. (2022):

1. The first step is to determine the classed photons for each 100-meter segment, classifying them as ground, canopy, or top of canopy. If there are fewer than 50 classed photons in a segment, do not calculate land or canopy products. If there are 50 or more classed photons in a segment, extract the ground photons to create the land products.
2. Next, if the number of ground photons is greater than 5% of the total number of classed photons within the segment, compute statistics on the ground photons including mean, median, min, max, standard deviation, mode, and skew. These heights will be reported on the product as h_te_mean, h_te_median, h_te_min, h_te_max, h_te_mode, and h_te_skew.
3. Compute the standard deviation of the ground photons about the interpolated terrain surface, FINALGROUND. This value is reported as h_te_std.
4. Compute the residuals of the ground photon Z heights about the interpolated terrain surface, FINALGROUND. The product is the root sum of squares of the ground photon residuals combined with the sigma_atlas_land. This parameter is reported as h_te_uncertainty.
5. Compute a linear fit on the ground photons and report the slope. This parameter is terrain_slope.
6. Calculate a best fit terrain elevation at the mid-point location of the 100-meter segment. Calculate each terrain photon's distance along-track into the 100-meter segment using the corresponding ATL03 20-meter products segment_length and dist_ph_along, and determine the mid-segment distance (expected to be $50\text{ m} \pm 0.5\text{ m}$). Use the mid-segment distance to linearly interpolate a mid-segment time (delta_time). Use the mid-segment time to linearly interpolate

A. Appendix

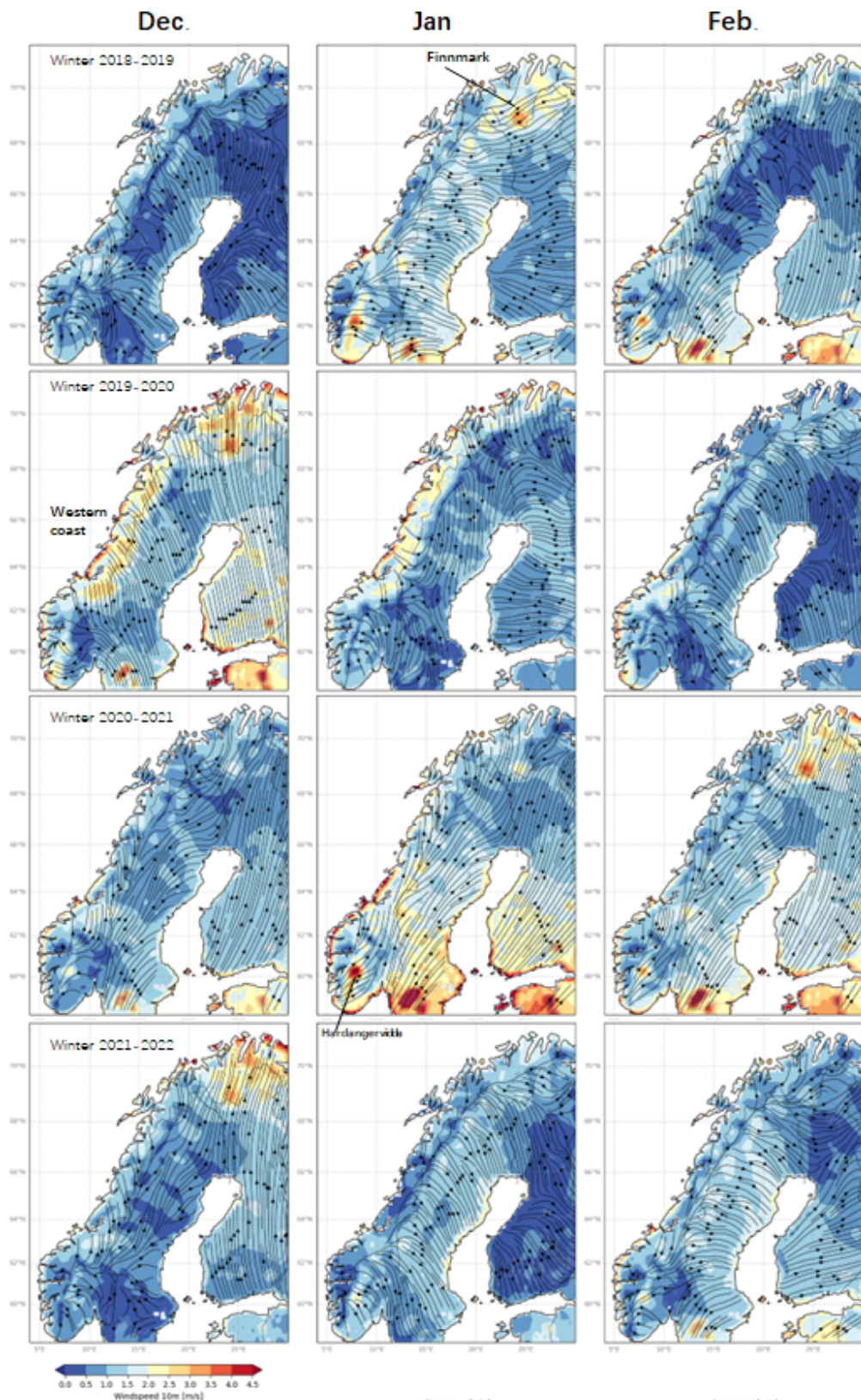


Figure A.1.: The Monthly Average of Wind Speed and Direction in Winter (2019-2022). Data source: ERA5-Land.
84

A.2. Technical Details of ICESat-2 ATL08

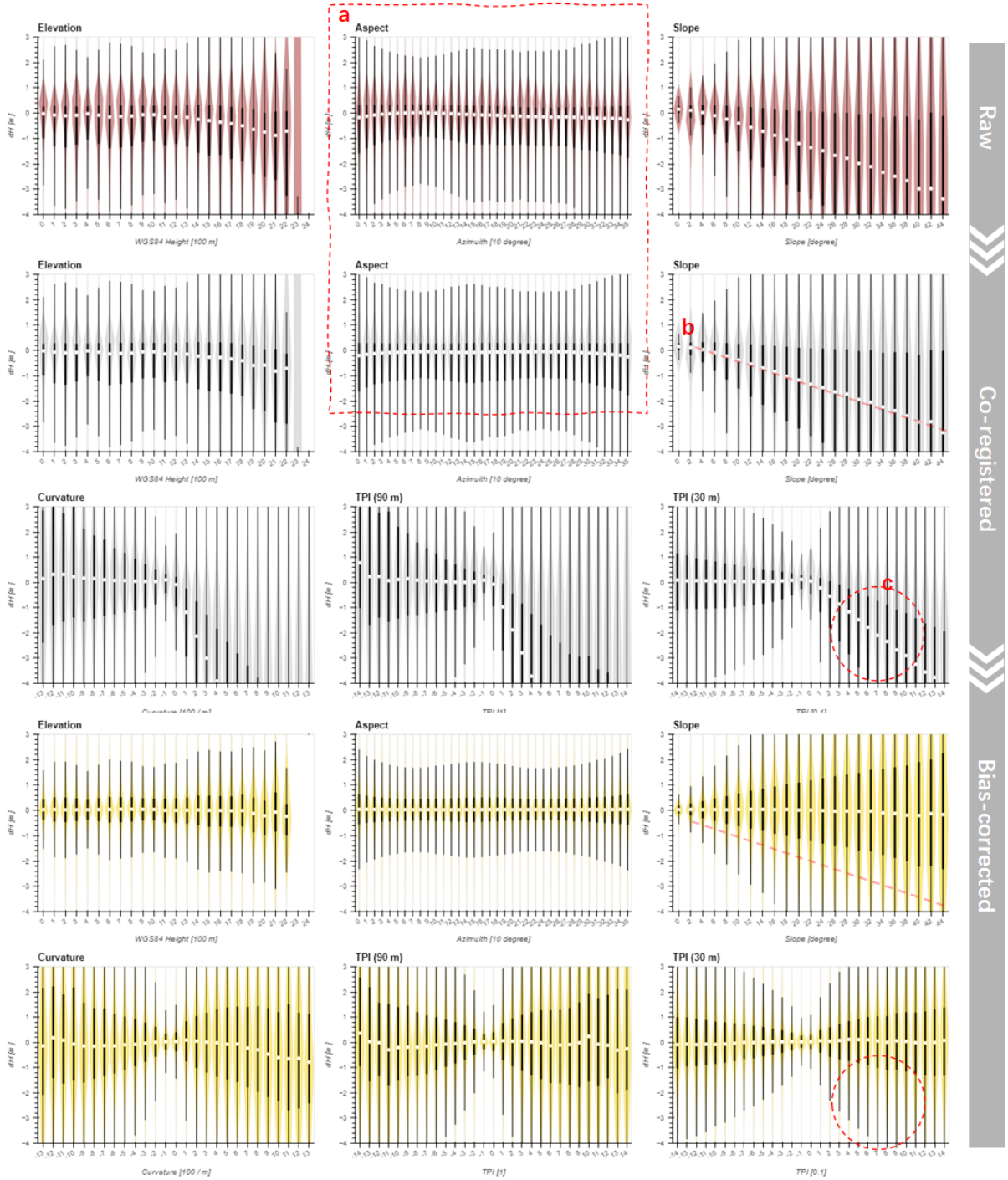


Figure A.2.: Statistic binning Analysis of DEM Errors: Coregistration and Bias correction (ICESat-2 - DTM1). The dataset was divided into categories at three stages, and for each category, a violin plot displays the distribution of data. The median of each dataset is represented by a white dot at the center of the violin. The thick bar illustrates the 25% and 75% quantiles, respectively. If the violin is skewed to one side, it indicates a deviation from normal distribution. The aspect-dependent bias is identified and eliminated by co-registratuion (a); The negative bias are widespread after co-registration (a, b, c).

A. Appendix

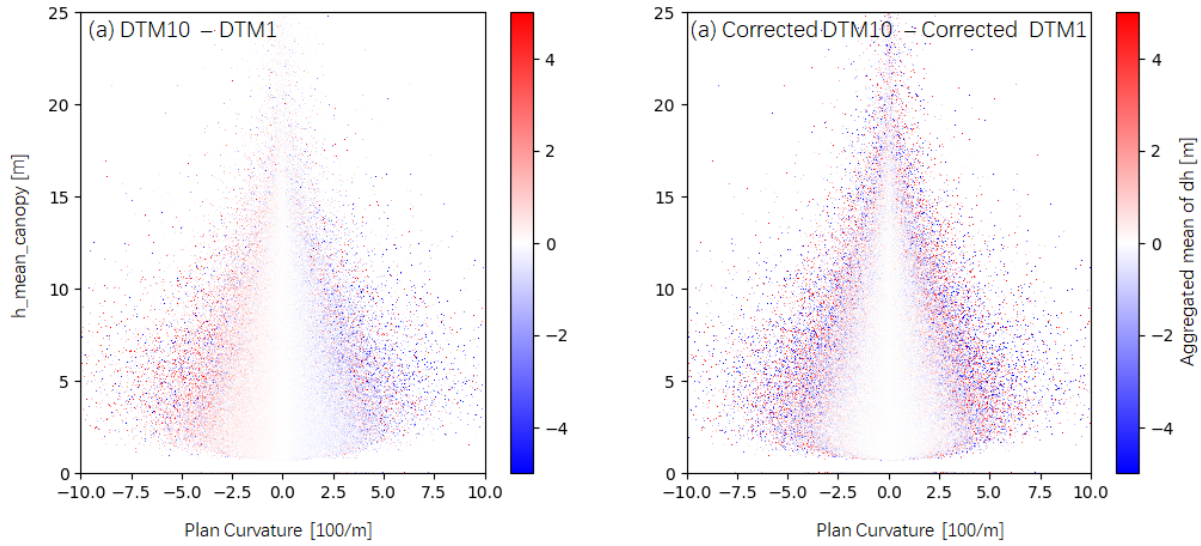


Figure A.3.: Comparision of DTM1 and DTM10 in terms of Plan Curvature and Canopy Height. The resolution limitation of DTM10 produced a positive bias over convave terrain and a negative bias over convex terrain (a). The patterns does not keep after bias correction (b).

other mid-segment parameters: interpolated terrain surface, FINALGROUND, as `h_te_interp`; latitude and longitude.

7. Calculate a linear fit as well as 3rd and 4th order polynomial fits to the terrain photons in the segment. Create a slope-adjusted and weighted mid-segment variable, weighted Z, from the linear fit. Use `terrain_slope` to apply a slope correction to each terrain photon by subtracting the terrain photon heights from the linear fit. Determine the mid-segment location of the linear fit, and add that height to the slope-corrected terrain photons. Apply a linear weighting to each photon based on its distance to the mid-segment location: $1 / \sqrt{(\text{photon distance along} - \text{mid-segment distance})^2}$. Calculate the weighted mid-segment terrain height, `weightedZ` as $\text{sum}(\text{each adjusted terrain height} * \text{its weight}) / \text{sum}(\text{all weights})$.
8. Finally, determine which of the three fits is best by calculating the mean and standard deviation of the fit errors. If one of the fits has both the smallest mean and standard deviations, use that fit. Else, use the fit with the smallest standard deviation. If more than one fit has the same mean and standard deviation, use the linear fit.

The full version please refer to Neuenschwander et al. (2022)

A.3. Recommendation For Winter Canopy Height Correction

A.2.2. Processing and QC Steps of ICESat-2 ATL08 Canopy products

This is a set of instructions for computing various parameters related to canopy height and structure using photon data from Neuenschwander et al. (2022) :

1. Classify photons as ground, canopy, or top of canopy for each 100m segment.
2. Only compute canopy height products if the number of canopy photons is > 5% of the total number of classed photons within the segment.
3. Compute statistics on the relative canopy heights (min, mean, median, max, and standard deviation).
4. Sort the heights and compute a cumulative distribution of the heights. Select the height associated with the 98% maximum height to get h_canopy.
5. Using the cumulative distribution of relative canopy heights, select the heights associated with the canopy_h_metrics percentile distributions (10, 15, 20, 25, 30, 35, 40, 45, 50, 55, 60, 65, 70, 75, 80, 85, 90, 95), and report as listed.
6. Compute the difference between h_canopy and canopy_h_metrics(50) to get h_dif_canopy, which represents an amount of canopy depth.
7. Compute the standard deviation of all photons that were labeled as Top of Canopy (flag 3) in the photon labeling portion to get toc_roughness.
8. Compute the quadratic mean height, h_canopy_quad, using the equation shown.

The full version please refer to Neuenschwander et al. (2022)

A.3. Recommendation For Winter Canopy Height Correction

Vegetation height has a significant impact on the quality of DEM and ground sampling of ICESat-2. It shows high feature importance in the regression model of bias correction (Figure 4.8). However, the bias caused by vegetation height is uneven across different terrains (refer to Sections 5.2.1 and 5.2.2). It has been observed that if we directly use canopy height from ICESat-2, it could lead to an underestimation of the correction strength (refer to Section 5.2.3.2). Therefore, it is crucial to use accurate canopy information.

Based on canopy information from ICESat-2 snow-free segments, the solution used in this study present here:

- (1) Training a binary regression model to determine the presence or absence of tree.
- (2) Training a canopy height regression model to estimate the canopy height.
- (3) Applying the estimated canopy height (2) snow-on segments according to the result from (1).

A. Appendix

A.4. Code Repository

A.4.1. Gradient Descent Coregistration

The gradient descent coregistration algorithm used in this study was implemented in Python and can be accessed on GitHub at <https://github.com/GlacioHack/xdem>. A brief overview, an application case, a discussion of the algorithm is provided in Section 3.3 4.3 5.1, but for a detailed and actual code implementation, please refer to the online repository.

A.4.2. XSnow

Xsnow is the production repository in this study, it contains the following function / scripts:

- (1) Download data from ERA5 Land Renalysis
- (2) Download data from ICESat-2
- (3) Process the data (3) into dataframe formats.
- (4) Extract, couple the dataframe (3) with climate dataset (1)
- (5) Pipeline the processes of DEM coregistration
- (6) Bias correction regression model
- (7) Snow depth downscaling regression model
- (8) Various plot function for this study.

References

- Abdalla, S., Abdeh Kolahchi, A., Ablain, M., Adusumilli, S., Aich Bhowmick, S., Alou-Font, E., Amarouche, L., Andersen, O. B., Antich, H., Aouf, L., Arbic, B., Armitage, T., Arnault, S., Artana, C., Aulicino, G., Ayoub, N., Badulin, S., Baker, S., Banks, C., ... Zlotnicki, V. (2021). Altimetry for the future: Building on 25 years of progress. *Advances in Space Research*, 68(2), 319–363. <https://doi.org/10.1016/j.asr.2021.01.022>
- Agency, E. S. (2021). Copernicus Global Digital Elevation Model. *Distributed by OpenTopography*. <https://doi.org/10.5069/G9028PQB>
- AMAP. (2017). *Snow, Water, Ice and Permafrost in the Arctic (SWIPA) 2017*.
- Amazon. (2023). *What Is Amazon SageMaker? - Amazon SageMaker*. <https://docs.aws.amazon.com/sagemaker/latest/dg/whatis.html>
- Anderson, E. A. (1968). Development and testing of snow pack energy balance equations. *Water Resources Research*, 4(1), 19–37. <https://doi.org/10.1029/WR004I001P00019>
- Arguez, A., & Vose, R. S. (2011). The Definition of the Standard WMO Climate Normal: The Key to Deriving Alternative Climate Normals. *Bulletin of the American Meteorological Society*, 92(6), 699–704. <https://doi.org/10.1175/2010BAMS2955.1>
- Atwood, D. K., Guritz, R. M., Muskett, R. R., Lingle, C. S., Sauber, J. M., & Freymueller, J. T. (2007). DEM Control in Arctic Alaska With ICESat Laser Altimetry. *IEEE Transactions on Geoscience and Remote Sensing*, 45(11), 3710–3720. <https://doi.org/10.1109/TGRS.2007.904335>
- Barnett, T. P., Adam, J. C., & Lettenmaier, D. P. (2005). Potential impacts of a warming climate on water availability in snow-dominated regions. *Nature*, 438(7066), 303–309. <https://doi.org/10.1038/nature04141>
- Bennett, K. E., Miller, G., Busey, R., Chen, M., Lathrop, E. R., Dann, J. B., Nutt, M., Crumley, R., Dillard, S. L., Dafflon, B., Kumar, J., Bolton, W. R., Wilson, C. J., Iversen, C. M., & Wullschleger, S. D. (2022). Spatial patterns of snow distribution in the sub-Arctic. *The Cryosphere*, 16(8), 3269–3293. <https://doi.org/10.5194/tc-16-3269-2022>
- Besl, P. J., & McKay, N. D. (1992). A method for registration of 3-D shapes. *IEEE Transactions on Pattern Analysis and Machine Intelligence*, 14(2), 239–256. <https://doi.org/10.1109/34.121791>
- Bormann, K. J., Brown, R. D., Derksen, C., & Painter, T. H. (2018). Estimating snow-cover trends from space. *Nature Climate Change*, 8(11), 924–928. <https://doi.org/10.1038/s41558-018-0318-3>
- Breiman, L. (2001). Random Forests. *Machine Learning*, 45(1), 5–32. <https://doi.org/10.1023/A:1010933404324>

A. Appendix

- Brenner, A. C., Blndschadler, R. A., Thomas, R. H., & Zwally, H. J. (1983). Slope-induced errors in radar altimetry over continental ice sheets. *Journal of Geophysical Research*, 88(C3), 1617. <https://doi.org/10.1029/JC088iC03p01617>
- Brenner, A. C., DiMarzio, J. P., & Zwally, H. J. (2007). Precision and Accuracy of Satellite Radar and Laser Altimeter Data Over the Continental Ice Sheets. *IEEE Transactions on Geoscience and Remote Sensing*, 45(2), 321–331. <https://doi.org/10.1109/TGRS.2006.887172>
- Brown, R. D., & Mote, P. W. (2009). The Response of Northern Hemisphere Snow Cover to a Changing Climate*. *Journal of Climate*, 22(8), 2124–2145. <https://doi.org/10.1175/2008JCLI2665.1>
- Buchhorn, M., Smets, B., Bertels, L., Roo, B. D., Lesiv, M., Tsendbazar, N.-E., Herold, M., & Fritz, S. (2020). *Copernicus Global Land Service: Land Cover 100m: Collection 3: Epoch 2019: Globe*. Zenodo. <https://zenodo.org/record/3939050>
- Callaghan, T. V., & Johansson, M. (2021). Snow, ice, and the biosphere. In *Snow and Ice-Related Hazards, Risks, and Disasters* (pp. 137–164). Elsevier. <https://linkinghub.elsevier.com/retrieve/pii/B9780128171295000123>
- Callaghan, T. V., Johansson, M., Brown, R. D., Groisman, P. Ya., Labba, N., Radionov, V., Bradley, R. S., Blangy, S., Bulygina, O. N., Christensen, T. R., Colman, J. E., Essery, R. L. H., Forbes, B. C., Forchhammer, M. C., Golubev, V. N., Honrath, R. E., Juday, G. P., Meshcherskaya, A. V., Phoenix, G. K., ... Wood, E. F. (2011). Multiple Effects of Changes in Arctic Snow Cover. *AMBIO*, 40(S1), 32–45. <https://doi.org/10.1007/s13280-011-0213-x>
- Carrer, M., Dibona, R., Prendin, A. L., & Brunetti, M. (2023). Recent waning snowpack in the Alps is unprecedented in the last six centuries. *Nature Climate Change*, 1–6. <https://doi.org/10.1038/s41558-022-01575-3>
- Carroll, M. L., Townshend, J. R., DiMiceli, C. M., Noojipady, P., & Sohlberg, R. A. (2009). A new global raster water mask at 250 m resolution. *International Journal of Digital Earth*, 2(4), 291–308. <https://doi.org/10.1080/17538940902951401>
- Chang, A. T. C., Foster, J. L., & Hall, D. K. (1987). Nimbus-7 SMMR Derived Global Snow Cover Parameters. *Annals of Glaciology*, 9, 39–44. <https://doi.org/10.3189/S0260305500200736>
- Chen, T., & Guestrin, C. (2016). XGBoost. *Proceedings of the 22nd ACM SIGKDD International Conference on Knowledge Discovery and Data Mining*, 785–794. <https://doi.org/10.1145/2939672.2939785>
- Chen, W., Yao, T., Zhang, G., Li, F., Zheng, G., Zhou, Y., & Xu, F. (2022). Towards ice-thickness inversion: An evaluation of global digital elevation models (DEMs) in the glacierized Tibetan Plateau. *The Cryosphere*, 16(1), 197–218. <https://doi.org/10.5194/tc-16-197-2022>
- Chen, X., Long, D., Hong, Y., Liang, S., & Hou, A. (2017). Observed radiative cooling over the Tibetan Plateau for the past three decades driven by snow cover-induced surface albedo anomaly. *Journal of Geophysical Research: Atmospheres*, 122(12), 6170–6185. <https://doi.org/10.1002/2017JD026652>
- Connor, L. N., Laxon, S. W., Ridout, A. L., Krabill, W. B., & McAdoo, D. C. (2009). Comparison of Envisat radar and airborne laser altimeter measurements over Arctic sea ice. *Remote Sensing of Environment*,

A.4. Code Repository

- ment, 113(3), 563–570. <https://doi.org/10.1016/j.rse.2008.10.015>
- Crawford, C. J. (2015). MODIS Terra Collection 6 fractional snow cover validation in mountainous terrain during spring snowmelt using Landsat TM and ETM+. *Hydrological Processes*, 29(1), 128–138. <https://doi.org/10.1002/hyp.10134>
- Dee, D. P., Balmaseda, M., Balsamo, G., Engelen, R., Simmons, A. J., & Thépaut, J.-N. (2014). Toward a Consistent Reanalysis of the Climate System. *Bulletin of the American Meteorological Society*, 95(8), 1235–1248. <https://doi.org/10.1175/BAMS-D-13-00043.1>
- Dee, D. P., Uppala, S. M., Simmons, A. J., Berrisford, P., Poli, P., Kobayashi, S., Andrae, U., Balmaseda, M. A., Balsamo, G., Bauer, P., Bechtold, P., Beljaars, A. C. M., van de Berg, L., Bidlot, J., Bormann, N., Delsol, C., Dragani, R., Fuentes, M., Geer, A. J., ... Vitart, F. (2011). The ERA-Interim reanalysis: Configuration and performance of the data assimilation system. *Quarterly Journal of the Royal Meteorological Society*, 137(656), 553–597. <https://doi.org/10.1002/qj.828>
- Deems, J. S., Painter, T. H., & Finnegan, D. C. (2013). Lidar measurement of snow depth: A review. *Journal of Glaciology*, 59(215), 467–479. <https://doi.org/10.3189/2013JoG12J154>
- Deschamps-Berger, C., Gascoin, S., Berthier, E., Deems, J., Gutmann, E., Dehecq, A., Shean, D., & Dumont, M. (2020). Snow depth mapping from stereo satellite imagery in mountainous terrain: Evaluation using airborne laser-scanning data. *The Cryosphere*, 14(9), 2925–2940. <https://doi.org/10.5194/tc-14-2925-2020>
- Deschamps-Berger, C., Gascoin, S., Shean, D., Besso, H., Guiot, A., & López-Moreno, J. I. (2022). *Evaluation of snow depth retrievals from ICESat-2 using airborne laser-scanning data* [Preprint]. Snow/Remote Sensing. <https://tc.copernicus.org/preprints/tc-2022-191/>
- Dietz, A. J., Kuenzer, C., Gessner, U., & Dech, S. (2012). Remote sensing of snow – a review of available methods. *International Journal of Remote Sensing*, 33(13), 4094–4134. <https://doi.org/10.1080/01431161.2011.640964>
- DVORNIKOV, Y. (2015). GIS and field data based modelling of snow water equivalent in shrub tundra. *Fennia – International Journal of Geography*. <https://doi.org/10.11143/46363>
- Enderlin, E. M., Elkin, C. M., Gendreau, M., Marshall, H. P., O’Neil, S., McNeil, C., Florentine, C., & Sass, L. (2022). Uncertainty of ICESat-2 ATL06- and ATL08-derived snow depths for glacierized and vegetated mountain regions. *Remote Sensing of Environment*, 283, 113307. <https://doi.org/10.1016/j.rse.2022.113307>
- Estilow, T. W., Young, A. H., & Robinson, D. A. (2015). A long-term Northern Hemisphere snow cover extent data record for climate studies and monitoring. *Earth System Science Data*, 7(1), 137–142. <https://doi.org/10.5194/essd-7-137-2015>
- Etzelmüller, B., Berthling, I., & Sollid, J. L. (2003). Aspects and concepts on the geomorphological significance of Holocene permafrost in southern Norway. *Geomorphology*, 52(1-2), 87–104. [https://doi.org/10.1016/S0169-555X\(02\)00250-7](https://doi.org/10.1016/S0169-555X(02)00250-7)
- Fiddes, J., Aalstad, K., & Lehning, M. (2022). TopoCLIM: Rapid topography-based downscaling of regional climate model output in complex terrain v1.1. *Geoscientific Model Development*, 15(4),

A. Appendix

- 1753–1768. <https://doi.org/10.5194/gmd-15-1753-2022>
- Fiddes, J., & Gruber, S. (2014). TopoSCALE v.1.0: Downscaling gridded climate data in complex terrain. *Geoscientific Model Development*, 7(1), 387–405. <https://doi.org/10.5194/gmd-7-387-2014>
- Fowler, H. J., Blenkinsop, S., & Tebaldi, C. (2007). Linking climate change modelling to impacts studies: Recent advances in downscaling techniques for hydrological modelling. *International Journal of Climatology*, 27(12), 1547–1578. <https://doi.org/10.1002/joc.1556>
- Fox-Kemper, B., Hewitt, H. T., Xiao, C., Aðalgeirsdóttir, G., Drijfhout, S. S., Edwards, T. L., Golledge, N. R., Hemer, M., Kopp, R. E., Krinner, G., Mix, A., Notz, D., Nowicki, S., Nurhati, I. S., Ruiz, L., Sallée, J.-B., Slanger, A. B. A., & Yu, Y. (2021). Chapter 9: Ocean, cryosphere, and sea level change. *Climate Change 2021: The Physical Science Basis. Contribution of Working Group I to the Sixth Assessment Report of the Intergovernmental Panel on Climate Change*, 1211–1361. <https://doi.org/10.1017/9781009157896.011>
- Freudiger, D., Kohn, I., Seibert, J., Stahl, K., & Weiler, M. (2017). Snow redistribution for the hydrological modeling of alpine catchments. *Wiley Interdisciplinary Reviews: Water*, 4(5), e1232. <https://doi.org/10.1002/wat2.1232>
- Girod, L., Nuth, C., Kääb, A., McNabb, R., & Galland, O. (2017). MMASTER: Improved ASTER DEMs for Elevation Change Monitoring. *Remote Sensing*, 9(7), 704. <https://doi.org/10.3390/rs9070704>
- Girotto, M., Musselman, K. N., & Essery, R. L. H. (2020). Data Assimilation Improves Estimates of Climate-Sensitive Seasonal Snow. *Current Climate Change Reports*, 6(3), 81–94. <https://doi.org/10.1007/s40641-020-00159-7>
- Gisnås, K., Westermann, S., Schuler, T. V., Melvold, K., & Etzelmüller, B. (2016). Small-scale variation of snow in a regional permafrost model. *The Cryosphere*, 10(3), 1201–1215. <https://doi.org/10.5194/tc-10-1201-2016>
- Grgić, M., Bašić, T., Grgić, M., & Bašić, T. (2021). *Radar Satellite Altimetry in Geodesy - Theory, Applications and Recent Developments*. IntechOpen. <https://www.intechopen.com/chapters/76245>
- Gruber, A., Wessel, B., Huber, M., & Roth, A. (2012). Operational TanDEM-X DEM calibration and first validation results. *ISPRS Journal of Photogrammetry and Remote Sensing*, 73, 39–49. <https://doi.org/10.1016/j.isprsjprs.2012.06.002>
- Gruen, A., & Akca, D. (2005). Least squares 3D surface and curve matching. *ISPRS Journal of Photogrammetry and Remote Sensing*, 59(3), 151–174. <https://doi.org/10.1016/j.isprsjprs.2005.02.006>
- Grünwald, T., Stötter, J., Pomeroy, J. W., Dadic, R., Moreno Baños, I., Marturià, J., Spross, M., Hopkinson, C., Burlando, P., & Lehning, M. (2013). Statistical modelling of the snow depth distribution in open alpine terrain. *Hydrology and Earth System Sciences*, 17(8), 3005–3021. <https://doi.org/10.5194/hess-17-3005-2013>
- Gulev, S. K., Thorne, P. W., Ahn, J., Dentener, F. J., Domingues, C. M., Gerland, S., Gong, D., Kaufman, D. S., Nnamchi, H. C., Quaas, J., Rivera, J. A., Sathyendranath, S., Smith, S. L., Trewin, B., von Schuckmann, K., & Vose, R. S. (2021). Chapter 2 Changing state of the climate system (V. Masson-Delmotte,

A.4. Code Repository

- P. Zhai, A. Pirani, S. L. Connors, C. Péan, S. Berger, N. Caud, Y. Chen, L. Goldfarb, M. I. Gomis, M. Huang, K. Leitzell, E. Lonnoy, J. B. R. Matthews, T. K. Maycock, T. Waterfield, O. Yelekçi, R. Yu, & B. Zhou, Eds.; pp. 287–422). Cambridge University Press. <https://doi.org/10.1017/9781009157896.004>.
- Hall, D. K., Riggs, G. A., & Salomonson, V. V. (2006). MODIS Snow and Sea Ice Products. *Earth Science Satellite Remote Sensing*, 154–181. https://doi.org/10.1007/978-3-540-37293-6_9
- Harpold, A. A., & Molotch, N. P. (2015). Sensitivity of soil water availability to changing snowmelt timing in the western U.S. *Geophysical Research Letters*, 42(19), 8011–8020. <https://doi.org/10.1002/2015GL065855>
- Hawker, L., Uhe, P., Paulo, L., Sosa, J., Savage, J., Sampson, C., & Neal, J. (2022). A 30 m global map of elevation with forests and buildings removed. *Environmental Research Letters*, 17(2), 024016. <https://doi.org/10.1088/1748-9326/ac4d4f>
- Henderson, G. R., Peings, Y., Furtado, J. C., & Kushner, P. J. (2018). Snow–atmosphere coupling in the Northern Hemisphere. *Nature Climate Change*, 8(11), 954–963. <https://doi.org/10.1038/s41558-018-0295-6>
- Hersbach, H., Bell, B., Berrisford, P., Hirahara, S., Horányi, A., Muñoz-Sabater, J., Nicolas, J., Peubey, C., Radu, R., Schepers, D., Simmons, A., Soci, C., Abdalla, S., Abellan, X., Balsamo, G., Bechtold, P., Biavati, G., Bidlot, J., Bonavita, M., ... Thépaut, J. (2020). The ERA5 global reanalysis. *Quarterly Journal of the Royal Meteorological Society*, 146(730), 1999–2049. <https://doi.org/10.1002/qj.3803>
- Hobeichi, S., Nishant, N., Shao, Y., Abramowitz, G., Pitman, A., Sherwood, S., Bishop, C., & Green, S. (2023). Using Machine Learning to Cut the Cost of Dynamical Downscaling. *Earth's Future*, 11(3), e2022EF003291. <https://doi.org/10.1029/2022EF003291>
- Hock, R., Rasul, G., Adler, C., Cáceres, B., Gruber, S., Hirabayashi, Y., Jackson, M., Kääb, A., Kang, S., Kutuzov, S., Noetzli, J., Rixen, C., & Zhang, Y. (2019). Chapter 2: High mountain areas. In *The Ocean and Cryosphere in a Changing Climate: Special Report of the Intergovernmental Panel on Climate Change* (1st ed., pp. 131–202). Cambridge University Press. <https://doi.org/10.1017/9781009157964.004>.
- Höhle, J., & Höhle, M. (2009). Accuracy assessment of digital elevation models by means of robust statistical methods. *ISPRS Journal of Photogrammetry and Remote Sensing*, 64(4), 398–406. <https://doi.org/10.1016/j.isprsjprs.2009.02.003>
- Hu, X., Hao, X., Wang, J., Huang, G., Li, H., & Yang, Q. (2022). Can the Depth of Seasonal Snow be Estimated From ICESat-2 Products: A Case Investigation in Altay, Northwest China. *IEEE Geoscience and Remote Sensing Letters*, 19, 1–5. <https://doi.org/10.1109/LGRS.2021.3078805>
- Hugonnet, R., Brun, F., Berthier, E., Dehecq, A., Mannerfelt, E. S., Eckert, N., & Farinotti, D. (2022). Uncertainty analysis of digital elevation models by spatial inference from stable terrain. 17. <https://doi.org/10.1109/JSTARS.2022.3188922>.
- Hugonnet, R., McNabb, R., Berthier, E., Menounos, B., Nuth, C., Girod, L., Farinotti, D., Huss, M., Dus-

A. Appendix

- saillant, I., Brun, F., & Kääb, A. (2021). Accelerated global glacier mass loss in the early twenty-first century. *Nature*, 592(7856), 726–731. <https://doi.org/10.1038/s41586-021-03436-z>
- Immerzeel, W. W., Lutz, A. F., Andrade, M., Bahl, A., Biemans, H., Bolch, T., Hyde, S., Brumby, S., Davies, B. J., Elmore, A. C., Emmer, A., Feng, M., Fernández, A., Haritashya, U., Kargel, J. S., Koppes, M., Kraaijenbrink, P. D. A., Kulkarni, A. V., Mayewski, P. A., ... Baillie, J. E. M. (2020). Importance and vulnerability of the world's water towers. *Nature*, 577(7790), 364–369. <https://doi.org/10.1038/s41586-019-1822-y>
- Kaspi, Y., & Schneider, T. (2011). Winter cold of eastern continental boundaries induced by warm ocean waters. *Nature*, 471(7340), 621–624. <https://doi.org/10.1038/nature09924>
- Keil, P., Mauritzen, T., Jungclaus, J., Hedemann, C., Olonscheck, D., & Ghosh, R. (2020). Multiple drivers of the North Atlantic warming hole. *Nature Climate Change*, 10(7), 667–671. <https://doi.org/10.1038/s41558-020-0819-8>
- Ketzler, G., Römer, W., & Beylich, A. A. (2021). The Climate of Norway. In A. A. Beylich (Ed.), *Landscapes and Landforms of Norway* (pp. 7–29). Springer International Publishing. https://doi.org/10.1007/978-3-030-52563-7_2
- Kimerling, A. J., Buckley, A. R., Muehrcke, P. C., & Muehrcke, J. O. (2016). *Map Use: Reading, Analysis, Interpretation*. Esri Press Academic. <https://books.google.com?id=22HPjwEACAAJ>
- Kingsford, C., & Salzberg, S. L. (2008). What are decision trees? *Nature Biotechnology*, 26(9), 1011–1013. <https://doi.org/10.1038/nbt0908-1011>
- Klehmets, K., Geyer, B., & Rockel, B. (2013). A regional climate model hindcast for Siberia: Analysis of snow water equivalent. *The Cryosphere*, 7(4), 1017–1034. <https://doi.org/10.5194/tc-7-1017-2013>
- Kraaijenbrink, P. D. A., Stigter, E. E., Yao, T., & Immerzeel, W. W. (2021). Climate change decisive for Asia's snow meltwater supply. *Nature Climate Change*, 11(7), 591–597. <https://doi.org/10.1038/s41558-021-01074-x>
- Kumar, P., Saharwardi, Md. S., Banerjee, A., Azam, Mohd. F., Dubey, A. K., & Murtugudde, R. (2019). Snowfall Variability Dictates Glacier Mass Balance Variability in Himalaya-Karakoram. *Scientific Reports*, 9(1), 1–9. <https://doi.org/10.1038/s41598-019-54553-9>
- Kunkel, K. E., Robinson, D. A., Champion, S., Yin, X., Estilow, T., & Frankson, R. M. (2016). Trends and Extremes in Northern Hemisphere Snow Characteristics. *Current Climate Change Reports*, 2(2), 65–73. <https://doi.org/10.1007/s40641-016-0036-8>
- Kwok, R., & Cunningham, G. F. (2008). ICESat over Arctic sea ice: Estimation of snow depth and ice thickness. *Journal of Geophysical Research*, 113(C8). <https://doi.org/10.1029/2008JC004753>
- Laloyaux, P., Balmaseda, M., Dee, D., Mogensen, K., & Janssen, P. (2016). A coupled data assimilation system for climate reanalysis. *Quarterly Journal of the Royal Meteorological Society*, 142(694), 65–78. <https://doi.org/10.1002/qj.2629>
- Li, G., Wang, Z. S., & Huang, N. (2018). A Snow Distribution Model Based on Snowfall and Snow Drifting Simulations in Mountain Area. *Journal of Geophysical Research: Atmospheres*, 123(14), 7193–7203.

A.4. Code Repository

- <https://doi.org/10.1029/2018JD028434>
- Li, H., Deng, Q., & Wang, L. (2017). Automatic Co-Registration of Digital Elevation Models Based on Centroids of Subwatersheds. *IEEE Transactions on Geoscience and Remote Sensing*, 55(11), 6639–6650. <https://doi.org/10.1109/TGRS.2017.2731048>
- Li, H., Zhao, J., Yan, B., Yue, L., & Wang, L. (2022). Global DEMs vary from one to another: An evaluation of newly released Copernicus, NASA and AW3D30 DEM on selected terrains of China using ICESat-2 altimetry data. *International Journal of Digital Earth*, 15(1), 1149–1168. <https://doi.org/10.1080/17538947.2022.2094002>
- Li, T., Hu, Y., Liu, B., Jiang, L., Wang, H., & Shen, X. (2022). Co-registration and residual correction of digital elevation models: A comparative study. *The Cryosphere Discussions*, 1–22. <https://doi.org/10.5194/tc-2022-205>
- Lievens, H., Brangers, I., Marshall, H.-P., Jonas, T., Olefs, M., & De Lannoy, G. (2022). Sentinel-1 snow depth retrieval at sub-kilometer resolution over the European Alps. *The Cryosphere*, 16(1), 159–177. <https://doi.org/10.5194/tc-16-159-2022>
- Lievens, H., Demuzere, M., Marshall, H.-P., Reichle, R. H., Brucker, L., Brangers, I., de Rosnay, P., Dumont, M., Girotto, M., Immerzeel, W. W., Jonas, T., Kim, E. J., Koch, I., Marty, C., Saloranta, T., Schöber, J., & De Lannoy, G. J. M. (2019). Snow depth variability in the Northern Hemisphere mountains observed from space. *Nature Communications*, 10(1), 4629. <https://doi.org/10.1038/s41467-019-12566-y>
- Liu, A. (2021). Performance evaluation of GEDI and ICESat-2 laser altimeter data for terrain and canopy height retrievals. *Remote Sensing of Environment*, 16.
- Liu, X. (2008). Airborne LiDAR for DEM generation: Some critical issues. *Progress in Physical Geography: Earth and Environment*, 32(1), 31–49. <https://doi.org/10.1177/0309133308089496>
- Livneh, B., & Badger, A. M. (2020). Drought less predictable under declining future snowpack. *Nature Climate Change*, 10(5), 452–458. <https://doi.org/10.1038/s41558-020-0754-8>
- Luojuus, K., Pulliainen, J., Takala, M., Lemmetyinen, J., Mortimer, C., Derksen, C., Mudryk, L., Moisander, M., Hiltunen, M., Smolander, T., Ikonen, J., Cohen, J., Salminen, M., Norberg, J., Veijola, K., & Venäläinen, P. (2021). GlobSnow v3.0 Northern Hemisphere snow water equivalent dataset. *Scientific Data*, 8(1), 163. <https://doi.org/10.1038/s41597-021-00939-2>
- Lussana, C. (2018). *seNorge_2018 daily mean temperature 1957-2017*. Zenodo. <https://doi.org/10.5281/zenodo.2023997>
- Macander, M. J., Swingley, C. S., Joly, K., & Reynolds, M. K. (2015). Landsat-based snow persistence map for northwest Alaska. *Remote Sensing of Environment*, 163, 23–31. <https://doi.org/10.1016/j.rse.2015.02.028>
- Magruder, L., Neuenschwander, A., & Klotz, B. (2021). Digital terrain model elevation corrections using space-based imagery and ICESat-2 laser altimetry. *Remote Sensing of Environment*, 264, 112621. <https://doi.org/10.1016/j.rse.2021.112621>
- Maraun, D., & Widmann, M. (2018). *Statistical Downscaling and Bias Correction for Climate Research*.

A. Appendix

- 10.1017/9781107588783
- Markus, T., Neumann, T., Martino, A., Abdalati, W., Brunt, K., Csatho, B., Farrell, S., Fricker, H., Gardner, A., Harding, D., Jasinski, M., Kwok, R., Magruder, L., Lubin, D., Luthcke, S., Morison, J., Nelson, R., Neuenschwander, A., Palm, S., ... Zwally, J. (2017). The Ice, Cloud, and land Elevation Satellite-2 (ICESat-2): Science requirements, concept, and implementation. *Remote Sensing of Environment*, 190, 260–273. <https://doi.org/10.1016/j.rse.2016.12.029>
- Matiu, M., Crespi, A., Bertoldi, G., Carmagnola, C. M., Marty, C., Morin, S., Schöner, W., Cat Berro, D., Chiogna, G., De Gregorio, L., Kotlarski, S., Majone, B., Resch, G., Terzago, S., Valt, M., Beozzo, W., Cianfarra, P., Gouttevin, I., Marcolini, G., ... Weilguni, V. (2021). Observed snow depth trends in the European Alps: 1971 to 2019. *The Cryosphere*, 15(3), 1343–1382. <https://doi.org/10.5194/tc-15-1343-2021>
- Maune, D. (2007). *Digital elevation model technologies and applications: The DEM users manual*.
- Melvold, K., & Skaugen, T. (2013). Multiscale spatial variability of lidar-derived and modeled snow depth on Hardangervidda, Norway. *Annals of Glaciology*, 54(62), 273–281. <https://doi.org/10.3189/2013AoG62A161>
- Melvold, K., & Skaugen, T. (2019). *Snow depth on Hardangervidda, South Norway 2008-2009*. Zenodo. <https://doi.org/10.5281/zenodo.2572732>
- Meredith, M., Sommerkorn, M., Cassotta, S., Derksen, C., Ekaykin, A., Hollowed, A., Kofinas, G., Mackintosh, A., Melbourne-Thomas, J., Muelbert, M., Ottersen, G., Pritchard, H., & A. G., S. (2019). Chapter 3: Polar Regions. IPCC Special Report on the Ocean and Cryosphere in a Changing Climate. In *The Ocean and Cryosphere in a Changing Climate: Special Report of the Intergovernmental Panel on Climate Change*. Cambridge University Press. <https://www.cambridge.org/core/product/identifier/9781009157964/type/book>
- Mesa-Mingorance, J. L., & Ariza-López, F. J. (2020). Accuracy Assessment of Digital Elevation Models (DEMs): A Critical Review of Practices of the Past Three Decades. *Remote Sensing*, 12(16), 2630. <https://doi.org/10.3390/rs12162630>
- Mo, H. M., Dai, L. Y., Fan, F., Che, T., & Hong, H. P. (2016). Extreme snow hazard and ground snow load for China. *Natural Hazards*, 84(3), 2095–2120. <https://doi.org/10.1007/s11069-016-2536-1>
- Mott, R., Vionnet, V., & Grunewald, T. (2018). The Seasonal Snow Cover Dynamics: Review on Wind-Driven Coupling Processes. *Frontiers in Earth Science*, 6. <https://doi.org/10.3389/feart.2018.00197>
- Mudryk, L. R., Derksen, C., Kushner, P. J., & Brown, R. (2015). Characterization of Northern Hemisphere Snow Water Equivalent Datasets, 1981–2010. *Journal of Climate*, 28(20), 8037–8051. <https://doi.org/10.1175/JCLI-D-15-0229.1>
- Mudryk, L., Santolaria-Otín, M., Krinner, G., Ménégoz, M., Derksen, C., Brutel-Vuilmet, C., Brady, M., & Essery, R. (2020). Historical Northern Hemisphere snow cover trends and projected changes in the CMIP6 multi-model ensemble. *The Cryosphere*, 14(7), 2495–2514. <https://doi.org/10.5194/tc-14-2495-2020>

A.4. Code Repository

- Muñoz Sabater, J. (2021a). *ERA5-Land hourly data from 1950 to present, Copernicus Climate Change Service (C3S) Climate Data Store (CDS)*. 10.24381/cds.e2161bac
- Muñoz Sabater, J. (2021b). *ERA5-Land monthly data from 1950 to present, Copernicus Climate Change Service (C3S) Climate Data Store (CDS)*. 10.24381/cds.68d2bb30
- Muñoz-Sabater, J., Dutra, E., Agustí-Panareda, A., Albergel, C., Arduini, G., Balsamo, G., Boussetta, S., Choulga, M., Harrigan, S., Hersbach, H., Martens, B., Miralles, D. G., Piles, M., Rodríguez-Fernández, N. J., Zsoter, E., Buontempo, C., & Thépaut, J.-N. (2021). ERA5-Land: A state-of-the-art global reanalysis dataset for land applications. *Earth System Science Data*, 13(9), 4349–4383. <https://doi.org/10.5194/essd-13-4349-2021>
- Musselman, K. N., Addor, N., Vano, J. A., & Molotch, N. P. (2021). Winter melt trends portend widespread declines in snow water resources. *Nature Climate Change*, 11(5), 418–424. <https://doi.org/10.1038/s41558-021-01014-9>
- Myers-Smith, I. H., Kerby, J. T., Phoenix, G. K., Bjerke, J. W., Epstein, H. E., Assmann, J. J., John, C., Andreu-Hayles, L., Angers-Blondin, S., Beck, P. S. A., Berner, L. T., Bhatt, U. S., Bjorkman, A. D., Blok, D., Bryn, A., Christiansen, C. T., Cornelissen, J. H. C., Cunliffe, A. M., Elmendorf, S. C., ... Wipf, S. (2020). Complexity revealed in the greening of the Arctic. *Nature Climate Change*, 10(2), 106–117. <https://doi.org/10.1038/S41558-019-0688-1>
- Neuenschwander, A., & Pitts, K. (2019). The ATL08 land and vegetation product for the ICESat-2 Mission. *Remote Sensing of Environment*, 221, 247–259. <https://doi.org/10.1016/j.rse.2018.11.005>
- Neuenschwander, A., Pitts, K., Jelley, B., Robbins, J., Markel, J., Popescu, S., Nelson, R., Harding, D., Klotz, B., & Sheridan, R. (2022). *Ice, Cloud, and Land Elevation Satellite 2 (ICESat-2) algorithm theoretical basis documents (ATBD) for Land-Vegetation along-track products (ATL08)*.
- Neumann, T., Brenner, A., Hancock, D., Robbins, J., Saba, J., Harbeck, K., Gibbons, A., Lee, J., Luthcke, S., & Rebold, T. (2021). *Ice, Cloud, and Land Elevation Satellite - 2 (ICESat-2) Project Algorithm Theoretical Basis Document (ATBD) for Global Geolocated Photons ATL03*. NASA Goddard Space Flight Center. <https://doi.org/10.5067/D0VQW9KX3GTU>
- Nolin, A. W. (2010). Recent advances in remote sensing of seasonal snow. *Journal of Glaciology*, 56(200), 1141–1150. <https://doi.org/10.3189/002214311796406077>
- Nuth, C., & Kääb, A. (2011). Co-registration and bias corrections of satellite elevation data sets for quantifying glacier thickness change. *The Cryosphere*, 5(1), 271–290. <https://doi.org/10.5194/tc-5-271-2011>
- Oksanen, J., & Sarjakoski, T. (2006). Uncovering the statistical and spatial characteristics of fine toposcale DEM error. *International Journal of Geographical Information Science*, 20(4), 345–369. <https://doi.org/10.1080/13658810500433891>
- Olvmo, M., Holmer, B., Thorsson, S., Reese, H., & Lindberg, F. (2020). Sub-arctic palsa degradation and the role of climatic drivers in the largest coherent palsa mire complex in Sweden (Vissátvuopmi), 1955–2016. *Scientific Reports*, 10(1), 8937. <https://doi.org/10.1038/s41598-020-65719-1>
- Orsolini, Y., Wegmann, M., Dutra, E., Liu, B., Balsamo, G., Yang, K., de Rosnay, P., Zhu, C., Wang, W.,

A. Appendix

- Senan, R., & Arduini, G. (2019). Evaluation of snow depth and snow cover over the Tibetan Plateau in global reanalyses using in situ and satellite remote sensing observations. *The Cryosphere*, 13(8), 2221–2239. <https://doi.org/10.5194/tc-13-2221-2019>
- Palmer, S., McMillan, M., & Morlighem, M. (2015). Subglacial lake drainage detected beneath the Greenland ice sheet. *Nature Communications*, 6(1), 8408. <https://doi.org/10.1038/ncomms9408>
- Paul, F., Bolch, T., Kääb, A., Nagler, T., Nuth, C., Scharrer, K., Shepherd, A., Strozzi, T., Ticconi, F., Bham bri, R., Berthier, E., Bevan, S., Gourmelen, N., Heid, T., Jeong, S., Kunz, M., Lauknes, T. R., Luckman, A., Merryman Boncori, J. P., ... Van Niel, T. (2015). The glaciers climate change initiative: Methods for creating glacier area, elevation change and velocity products. *Remote Sensing of Environment*, 162, 408–426. <https://doi.org/10.1016/j.rse.2013.07.043>
- Peckham, S. (2011, May 30). *Profile, Plan and Streamline Curvature: A Simple Derivation and Applications*.
- PENG, S., PIAO, S., CIAIS, P., FANG, J., & WANG, X. (2010). Change in winter snow depth and its impacts on vegetation in China. *Global Change Biology*, 16(11), no-no. <https://doi.org/10.1111/j.1365-2486.2010.02210.x>
- Perovich, D. K., Light, B., Eicken, H., Jones, K. F., Runciman, K., & Nghiem, S. V. (2007). Increasing solar heating of the Arctic Ocean and adjacent seas, 1979–2005: Attribution and role in the ice-albedo feedback. *Geophysical Research Letters*, 34(19). <https://doi.org/10.1029/2007GL031480>
- Pritchard, H. D., Ligtenberg, S. R. M., Fricker, H. A., Vaughan, D. G., van den Broeke, M. R., & Padman, L. (2012). Antarctic ice-sheet loss driven by basal melting of ice shelves. *Nature*, 484(7395), 502–505. <https://doi.org/10.1038/nature10968>
- Qin, Y., Abatzoglou, J. T., Siebert, S., Huning, L. S., AghaKouchak, A., Mankin, J. S., Hong, C., Tong, D., Davis, S. J., & Mueller, N. D. (2020). Agricultural risks from changing snowmelt. *Nature Climate Change*, 10(5), 459–465. <https://doi.org/10.1038/s41558-020-0746-8>
- Quante, L., Willner, S. N., Middelanis, R., & Levermann, A. (2021). Regions of intensification of extreme snowfall under future warming. *Scientific Reports*, 11(1), 16621. <https://doi.org/10.1038/s41598-021-95979-4>
- Rashmi, K. V., & Gilad-Bachrach, R. (2015, May 7). *DART: Dropouts meet Multiple Additive Regression Trees*. <https://doi.org/10.48550/arXiv.1505.01866>
- Rasmussen, R., Baker, B., Kochendorfer, J., Meyers, T., Landolt, S., Fischer, A. P., Black, J., Thériault, J. M., Kucera, P., Gochis, D., Smith, C., Nitu, R., Hall, M., Ikeda, K., & Gutmann, E. (2012). How Well Are We Measuring Snow: The NOAA/FAA/NCAR Winter Precipitation Test Bed. *Bulletin of the American Meteorological Society*, 93(6), 811–829. <https://doi.org/10.1175/BAMS-D-11-00052.1>
- Réveillet, M., Dumont, M., Gascoin, S., Lafaysse, M., Nabat, P., Ribes, A., Nheili, R., Tuzet, F., Ménégoz, M., Morin, S., Picard, G., & Ginoux, P. (2022). Black carbon and dust alter the response of mountain snow cover under climate change. *Nature Communications*, 13(1), 5279. <https://doi.org/10.1038/s41467-022-32501-y>
- Revuelto, J., López-Moreno, J. I., Azorin-Molina, C., & Vicente-Serrano, S. M. (2014). Topographic con-

A.4. Code Repository

- trol of snowpack distribution in a small catchment in the central Spanish Pyrenees: Intra- and inter-annual persistence. *The Cryosphere*, 8(5), 1989–2006. <https://doi.org/10.5194/tc-8-1989-2014>
- Rhoades, A. M., Hatchett, B. J., Risser, M. D., Collins, W. D., Bambach, N. E., Huning, L. S., McCrary, R., Siirila-Woodburn, E. R., Ullrich, P. A., Wehner, M. F., Zarzycki, C. M., & Jones, A. D. (2022). Asymmetric emergence of low-to-no snow in the midlatitudes of the American Cordillera. *Nature Climate Change*, 12(12), 1151–1159. <https://doi.org/10.1038/s41558-022-01518-y>
- Riihelä, A., Bright, R. M., & Anttila, K. (2021). Recent strengthening of snow and ice albedo feedback driven by Antarctic sea-ice loss. *Nature Geoscience*, 14(11), 832–836. <https://doi.org/10.1038/s41561-021-00841-x>
- Rosen, P. A., Hensley, S., Joughin, I. R., Li, F. K., Madsen, S. N., Rodriguez, E., & Goldstein, R. M. (2000). Synthetic aperture radar interferometry. *Proceedings of the IEEE*, 88(3), 333–382. <https://doi.org/10.1109/5.838084>
- Rott, H., & Nagler, T. (1993). *Capabilities of ERS-1 SAR for snow and glacier monitoring in Alpine areas*.
- Sachindra, D. A., Ahmed, K., Rashid, Md. M., Shahid, S., & Perera, B. J. C. (2018). Statistical downscaling of precipitation using machine learning techniques. *Atmospheric Research*, 212, 240–258. <https://doi.org/10.1016/j.atmosres.2018.05.022>
- Sandberg Sørensen, L., Simonsen, S. B., Forsberg, R., Khvorostovsky, K., Meister, R., & Engdahl, M. E. (2018). 25 years of elevation changes of the Greenland Ice Sheet from ERS, Envisat, and CryoSat-2 radar altimetry. *Earth and Planetary Science Letters*, 495, 234–241. <https://doi.org/10.1016/j.epsl.2018.05.015>
- Schutz, B. E., Zwally, H. J., Shuman, C. A., Hancock, D., & DiMarzio, J. P. (2005). Overview of the ICESat Mission. *Geophysical Research Letters*, 32(21). <https://doi.org/10.1029/2005GL024009>
- Schweizer, J., Bartelt, P., & van Herwijnen, A. (2021). Snow avalanches. In *Snow and Ice-Related Hazards, Risks, and Disasters* (pp. 377–416). Elsevier. <https://doi.org/10.1016/B978-0-12-817129-5.00001-9>
- Schweizer, J., Bruce Jamieson, J., & Schneebeli, M. (2003). Snow avalanche formation. *Reviews of Geophysics*, 41(4). <https://doi.org/10.1029/2002RG000123>
- Seppälä, M. (1994). Snow depth controls palsu growth. *Permafrost and Periglacial Processes*, 5(4), 283–288. <https://doi.org/10.1002/ppp.3430050407>
- Siirila-Woodburn, E. R., Rhoades, A. M., Hatchett, B. J., Huning, L. S., Szinai, J., Tague, C., Nico, P. S., Feldman, D. R., Jones, A. D., Collins, W. D., & Kaatz, L. (2021). A low-to-no snow future and its impacts on water resources in the western United States. *Nature Reviews Earth & Environment*, 2(11), 800–819. <https://doi.org/10.1038/s43017-021-00219-y>
- Smith, B., Fricker, H. A., Holschuh, N., Gardner, A. S., Adusumilli, S., Brunt, K. M., Csatho, B., Harbeck, K., Huth, A., Neumann, T., Nilsson, J., & Siegfried, M. R. (2019). Land ice height-retrieval algorithm for NASA's ICESat-2 photon-counting laser altimeter. *Remote Sensing of Environment*, 233, 111352. <https://doi.org/10.1016/j.rse.2019.111352>
- Snauffer, A. M., Hsieh, W. W., & Cannon, A. J. (2016). Comparison of gridded snow water equivalent

A. Appendix

- products with in situ measurements in British Columbia, Canada. *Journal of Hydrology*, 541, 714–726. <https://doi.org/10.1016/j.jhydrol.2016.07.027>
- Sturm, M., Holmgren, J., McFadden, J. P., Liston, G. E., Chapin, F. S., & Racine, C. H. (2001). Snow-Shrub Interactions in Arctic Tundra: A Hypothesis with Climatic Implications. *Journal of Climate*, 14(3), 336–344. [https://doi.org/10.1175/1520-0442\(2001\)014%3C0336:SSIIAT%3E2.0.CO;2](https://doi.org/10.1175/1520-0442(2001)014%3C0336:SSIIAT%3E2.0.CO;2)
- Sturm, M., & Massom, R. (2016). Snow in the sea ice system: Friend or foe? In *Sea Ice: Third Edition* (pp. 65–109). <https://doi.org/10.1002/9781118778371.ch3>
- Sturm, M., & Wagner, A. M. (2010). Using repeated patterns in snow distribution modeling: An Arctic example. *Water Resources Research*, 46(12). <https://doi.org/10.1029/2010WR009434>
- Tang, X., Xie, J., Liu, R., Huang, G., Zhao, C., Zhen, Y., Tang, H., & Dou, X. (2020). Overview of the GF-7 Laser Altimeter System Mission. *Earth and Space Science*, 7(1), e2019EA000777. <https://doi.org/10.1029/2019EA000777>
- The physical geography of Fennoscandia*. (2005). [Computer software]. Oxford University Press.
- Tian, X., & Shan, J. (2021). Comprehensive Evaluation of the ICESat-2 ATL08 Terrain Product. *IEEE Transactions on Geoscience and Remote Sensing*, 59(10), 8195–8209. <https://doi.org/10.1109/TGRS.2021.3051086>
- Townsend, W. (1980). An initial assessment of the performance achieved by the Seasat-1 radar altimeter. *IEEE Journal of Oceanic Engineering*, 5(2), 80–92. <https://doi.org/10.1109/JOE.1980.1145459>
- Treichler, D., & Kääb, A. (2017). Snow depth from ICESat laser altimetry – A test study in southern Norway. *Remote Sensing of Environment*, 191, 389–401. <https://doi.org/10.1016/j.rse.2017.01.022>
- Trujillo, E., Ramírez, J. A., & Elder, K. J. (2007). Topographic, meteorologic, and canopy controls on the scaling characteristics of the spatial distribution of snow depth fields. *Water Resources Research*, 43(7). <https://doi.org/10.1029/2006WR005317>
- Tsang, L., Durand, M., Derksen, C., Barros, A. P., Kang, D.-H., Lievens, H., Marshall, H.-P., Zhu, J., Johnson, J., King, J., Lemmetyinen, J., Sandells, M., Rutter, N., Siqueira, P., Nolin, A., Osmanoglu, B., Vuyovich, C., Kim, E., Taylor, D., ... Xu, X. (2022). Review article: Global monitoring of snow water equivalent using high-frequency radar remote sensing. *The Cryosphere*, 16(9), 3531–3573. <https://doi.org/10.5194/tc-16-3531-2022>
- Vacaflor, P., Lenzano, M. G., Vich, A., & Lenzano, L. (2022). Co-Registration Methods and Error Analysis for Four Decades (1979–2018) of Glacier Elevation Changes in the Southern Patagonian Icefield. *Remote Sensing*, 14(4), 820. <https://doi.org/10.3390/rs14040820>
- Wang, X. (2022). *WRF-based dynamical downscaling over High Mountain Asia*. <https://depositonce.tu-berlin.de/handle/11303/16159>
- Wang, X., Cheng, X., Gong, P., Huang, H., Li, Z., & Li, X. (2011). Earth science applications of ICESat-/GLAS: A review. *International Journal of Remote Sensing*, 32(23), 8837–8864. <https://doi.org/10.1080/01431161.2010.547533>
- Weiss, A. (2001). *Topographic position and landforms analysis*. [Poster presentation]. ESRI user con-

A.4. Code Repository

- ference, San Diego, CA. http://www.jennessent.com/downloads/TPI-poster-TNC_18x22.pdf
- Westoby, M. J., Brasington, J., Glasser, N. F., Hambrey, M. J., & Reynolds, J. M. (2012). "Structure-from-Motion" photogrammetry: A low-cost, effective tool for geoscience applications. *Geomorphology*, 179, 300–314. <https://doi.org/10.1016/j.geomorph.2012.08.021>
- Wilby, R. L., & Wigley, T. M. L. (1997). Downscaling general circulation model output: A review of methods and limitations. *Progress in Physical Geography: Earth and Environment*, 21(4), 530–548. <https://doi.org/10.1177/030913339702100403>
- Wipf, S., Stoeckli, V., & Bebi, P. (2009). Winter climate change in alpine tundra: Plant responses to changes in snow depth and snowmelt timing. *Climatic Change*, 94(1-2), 105–121. <https://doi.org/10.1007/S10584-009-9546-X>
- Xdem contributors. (2021). *Xdem*. Zenodo. <https://doi.org/10.5281/zenodo.4809698>
- Xiong, L., Li, S., Tang, G., & Strobl, J. (2022). Geomorphometry and terrain analysis: Data, methods, platforms and applications. *Earth-Science Reviews*, 233, 104191. <https://doi.org/10.1016/j.earsci.rev.2022.104191>
- Xu, W., Ma, L., Ma, M., Zhang, H., & Yuan, W. (2017). Spatial-Temporal Variability of Snow Cover and Depth in the Qinghai-Tibetan Plateau. *Journal of Climate*, 30(4), 1521–1533. <https://doi.org/10.1175/JCLI-D-15-0732.1>
- Yamazaki, D., Ikeshima, D., Tawatari, R., Yamaguchi, T., O'Loughlin, F., Neal, J. C., Sampson, C. C., Kanae, S., & Bates, P. D. (2017). A high-accuracy map of global terrain elevations. *Geophysical Research Letters*, 44(11), 5844–5853. <https://doi.org/10.1002/2017GL072874>
- Yueh, S. H., Dinardo, S. J., Akgiray, A., West, R., Cline, D. W., & Elder, K. (2009). Airborne Ku-Band Polarimetric Radar Remote Sensing of Terrestrial Snow Cover. *IEEE Transactions on Geoscience and Remote Sensing*, 47(10), 3347–3364. <https://doi.org/10.1109/TGRS.2009.2022945>
- Zevenbergen, L. W., & Thorne, C. R. (1987). Quantitative analysis of land surface topography. *Earth Surface Processes and Landforms*, 12(1), 47–56. <https://doi.org/10.1002/esp.3290120107>
- Zhu, P., Kim, T., Jin, Z., Lin, C., Wang, X., Ciais, P., Mueller, N. D., Aghakouchak, A., Huang, J., Mulla, D., & Makowski, D. (2022). The critical benefits of snowpack insulation and snowmelt for winter wheat productivity. *Nature Climate Change*, 12(5, 5), 485–490. <https://doi.org/10.1038/s41558-022-01327-3>

